



## **COMPARATIVE STATISTICAL ANALYSIS OF AURORAL MODELS**

**THESIS**

Cory T. Lane, Major, USAF

AFIT/APPLPHY/ENP/12-M07

**DEPARTMENT OF THE AIR FORCE  
AIR UNIVERSITY**

**AIR FORCE INSTITUTE OF TECHNOLOGY**

**Wright-Patterson Air Force Base, Ohio**

**DISTRIBUTION STATEMENT A  
APPROVED FOR PUBLIC RELEASE; DISTRIBUTION UNLIMITED**

The views expressed in this thesis are those of the author and do not reflect the official policy or position of the United States Air Force, Department of Defense, or the United States Government. This work is declared a work of the U.S. Government and is not subject to copyright protection in the United States.

AFIT/APPLPHY/ENP/12-M07

COMPARATIVE STATISTICAL ANALYSIS OF AURORAL MODELS

THESIS

Presented to the Faculty

Department of Engineering Physics

Graduate School of Engineering and Management

Air Force Institute of Technology

Air University

Air Education and Training Command

In Partial Fulfillment of the Requirements for the  
Degree of Master of Science in Applied Physics

Cory T. Lane, BS

Major, USAF

March 2012

DISTRIBUTION STATEMENT A  
APPROVED FOR PUBLIC RELEASE; DISTRIBUTION UNLIMITED

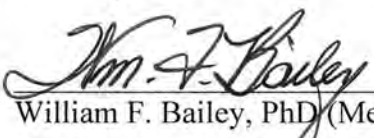
COMPARATIVE STATISTICAL ANALYSIS OF AURORAL MODELS

Cory T. Lane, BS  
Major, USAF

Approved:

  
\_\_\_\_\_  
Lt Col Ariel O. Acebal (Chairman)

8 MARCH 2012  
Date

  
\_\_\_\_\_  
William F. Bailey, PhD (Member)

21 Mar '12  
Date

  
\_\_\_\_\_  
Yihua Zheng, PhD (Member)

21 Mar / 2012  
Date

## Abstract

Accurate modeling of the auroral region is an important component to mitigate risk to space-based assets and communications systems. Many auroral models have been developed, but little effort has been made to validate their accuracy. The location of the equatorward boundary of the auroral oval provides an appropriate means to measure the accuracy of auroral models.

In this study, the equatorward boundary was represented by the location at which the energy flux measured by DMSP satellites exceeded a fixed threshold of  $0.4 \text{ erg/cm}^2/\text{s}$ . Magnetic latitude (MLAT) coordinates were obtained from more than 4,000 orbits through the polar region of the Northern Hemisphere and compared to the outputs of five auroral precipitation models. The models tested in this study included: the original Hardy auroral model of 1985 (OH), the OVATION Prime model (OP), the 2008 adaptation to the Hardy model (NH), the Space Weather Modeling Framework Ring-Current model (SWMF), and the Assimilated Mapping of Ionospheric Electrodynamics model (AMIE).

Each model's energy flux output was compared to DMSP data in a variety of categories including: high, moderate, and low K<sub>p</sub> index conditions; dawn, day, and dusk magnetic local time (MLT) sectors; and all four seasons. Differences between the model and satellite data were quantified and catalogued. A prediction efficiency (PE) score and was also calculated for each model and used to assess relative accuracy in the various categories. The statistical results using  $0.4 \text{ erg/cm}^2/\text{s}$  were validated by repeating the analysis using  $0.6 \text{ erg/cm}^2/\text{s}$  as the energy flux threshold.

In each of the 19 Kp-MLT-season categories combinations considered in this study, no singular model garnered a preponderance of the highest PE scores, when using the lower energy flux threshold. The SWMF model received the highest PE score in 4 categories, the NH model in 4 categories, the OH model in 5 categories, and the OP model in 6 categories. When the higher flux threshold was used, the OP model received the majority of the highest PE scores.

The model with the highest overall prediction efficiency score was the OP model (0.55). The OH model (0.51) had the second highest score, and it was followed by the NH model (0.45). The OP model's performance was well corroborated using the 0.6 erg/cm<sup>2</sup>/s threshold. Thus, the OP model is therefore deemed to be the most accurate of the models tested in this study and is most suitable for operational auroral forecasting.

## Acknowledgements

I am extremely grateful for the patience and persistence afforded to me by Lt Col Ariel Acebal. He possesses a truly incredible mastery of the subject material, and his guidance was integral to the completion of this initially overwhelming project. He excels as both a scientist and a mentor, and I am truly humbled by his diligence and work ethic.

Dr. William Bailey has that kind of genius that is as remarkable as it is rare. I feel extremely fortunate that he was the professor responsible for teaching plasma physics, whose importance to a study of this sort cannot be overstated, and I am proud that my thesis is one in a long line of graduate level work authored with his involvement and support.

I am also deeply indebted to Dr. Yihua Zheng at NASA's. The depth and breadth of her practical knowledge of this subject material is incredible, and her support and contributions to this project were substantial. She shoulders an incredible load at NASA, and I am very thankful she was willing to add this project to her extremely busy schedule.

Lastly, I must also express my sincere appreciation for the rest of the faculty and staff responsible for the Applied Physics program within ENP. There is something to be said about an organization of professionals who can nurture a pilot like me through a program like this. Thanks to all!

Cory T. Lane

# Table of Contents

|  | Page |
|--|------|
| Abstract.....  | iv   |
| Acknowledgements.....  | vi   |
| List of Figures.....   | ix   |
| List of Tables .....   | xi   |
| I. Introduction.....   | 1    |
| 1.1 Motivation.....  | 1    |
| 1.2 Research Topic.....  | 2    |
| 1.3 Research Objective .....                                   | 3    |
| 1.4 Document Structure .....                                   | 5    |
| II. Theory and Background .....                                | 6    |
| 2.1 Theoretical Background.....                                | 6    |
| 2.1.1 The Solar Wind.....                                      | 8    |
| 2.1.2 Magnetic Reconnection .....                              | 10   |
| 2.1.3 Magnetospheric Particle Flow .....                       | 11   |
| 2.1.4 Ionospheric Coupling .....                               | 14   |
| 2.1.5 Plasma Sheet Topology .....                              | 17   |
| 2.1.6 Auroral Current System and Emissions.....                | 19   |
| 2.2 Auroral Oval Boundaries .....                              | 21   |
| 2.3 Auroral Categorization and Measurements .....              | 24   |
| 2.3.1 The Planetary K Index .....                              | 24   |
| 2.3.2 DMSP Satellites and Sensors .....                        | 25   |
| 2.4 Auroral Modeling.....                                      | 26   |
| 2.4.1 The Hardy Model – 1985 Version .....                     | 27   |
| 2.4.2 The OVATION Prime Model.....                             | 29   |
| 2.4.3 The Hardy Model – 2008 Adaptation.....                   | 32   |
| 2.4.4 Space Weather Modeling Framework Model.....              | 34   |
| 2.4.5 Assimilative Mapping of Ionospheric Electrodynamics..... | 36   |
| III. Methodology.....  | 38   |
| 3.1 DMSP Data .....  | 38   |
| 3.1.1 DMSP Data Acquisition .....                              | 38   |
| 3.1.2 DMSP Data Compilation.....                               | 40   |
| 3.2 Auroral Precipitation Models.....                          | 46   |
| 3.2.1 The Original Hardy Model .....                           | 46   |
| 3.2.2 OVATION Prime Model .....                                | 47   |
| 3.2.3 The New Hardy Model .....                                | 49   |

|   | Page       |
|---|------------|
| 3.2.4 Space Weather Modeling Framework Model.....                         | 50         |
| 3.2.5 Assimilative Mapping of Ionospheric Electrodynamics Model .....     | 51         |
| 3.3 Data Compilation .....  | 52         |
| 3.4 Statistical Measures .....  | 54         |
| <b>IV. Results and Analysis.....</b>                                      | <b>57</b>  |
| 4.1 DMSP Data Characteristics .....                                       | 57         |
| 4.1.1 DMSP Systematics .....  | 58         |
| 4.1.2 Regression Analysis .....   | 61         |
| 4.1.3 Data Binning.....   | 64         |
| 4.1.4 Data Losses.....  | 65         |
| 4.2 Individual Model Characteristics as a Function of Kp Index .....      | 69         |
| 4.3 Model Accuracy Comparisons.....                                       | 72         |
| 4.3.1 Ratio Estimate.....   | 73         |
| 4.3.2 Mean Deviation between DMSP and Model .....                         | 74         |
| 4.3.3 Prediction Efficiency (PE) .....                                    | 79         |
| 4.3.4 Skill Score.....  | 82         |
| 4.4 Comparative Statistics Using Different Thresholds .....               | 84         |
| 4.5 Small-scale Experiment Using Predictable Precipitation Patterns ..... | 92         |
| <b>V. Conclusion .....</b>  | <b>100</b> |
| 5.1 Summary of Results .....  | 100        |
| 5.2 Future Research .....   | 102        |
| <b>Bibliography .....</b>   | <b>104</b> |

## List of Figures

| Figure   | Page |
|--|------|
| 1. Schematic of polar oval .....   | 7    |
| 2. Auroral Process Chain .....   | 8    |
| 3. Depiction of IMF's spiral orientation .....   | 9    |
| 4. Depiction of earth's magnetosphere .....  | 10   |
| 5. Geomagnetic field lines in the earth's magnetotail.....                             | 12   |
| 6. DMSP satellite particle counts.....   | 15   |
| 7. Pitch angle diffusion in plasma sheet.....  | 17   |
| 8. Geomagnetic field model accounting for asymmetry .....                              | 18   |
| 9. Characteristic polar region current flows.....                                      | 19   |
| 10. Sample DMSP spectrogram.....   | 23   |
| 11. OH model polar plots.....  | 29   |
| 12. OP model polar plots showing quiet solar drivingversus storming .....              | 32   |
| 13. NH model polar plots.....  | 34   |
| 14. SWMF boundary plot .....   | 36   |
| 15. AMIE polar plot.....   | 37   |
| 16. DMSP orbit plot example .....  | 42   |
| 17. Example of discarded orbit due to anomalous data. ....                             | 43   |
| 18. DMSP crossing points using a 0.4 erg/cm <sup>2</sup> /s energy flux threshold..... | 44   |
| 19. OH equatorward boundaries at various Kp indices .....                              | 46   |
| 20. OP boundary plot generated during Kp 4 conditions.....                             | 48   |
| 21. Example of spurious OP boundary point.....   | 49   |

| Figure  | Page |
|---|------|
| 22. NH equatorward boundaries at various Kp indices .....                           | 50   |
| 23. SWMF boundary plots generated at various Kp indices .....                       | 51   |
| 24. AMIE boundary plot during storming conditions.....                              | 52   |
| 25. DMSP threshold crossings grouped by Kp index .....                              | 59   |
| 26. Distribution of DMSP data .....   | 61   |
| 27. Scatterplots of DMSP threshold crossing coordinates.....                        | 64   |
| 28. DMSP threshold crossings grouped by MLT sectors .....                           | 66   |
| 29. Data losses .....   | 68   |
| 30. OP model output during quiet conditions .....                                   | 69   |
| 31. Plots of DMSP and model threshold crossings as functions of Kp .....            | 71   |
| 32. Deviations between DMSP and models at 0.4 erg/cm <sup>2</sup> /s threshold..... | 75   |
| 33. MLAT deviations between DMSP and models during storming .....                   | 77   |
| 34. Threshold crossing anomalies using high energy flux threshold.....              | 86   |
| 35. Deviations between DMSP and models at 0.6 erg/cm <sup>2</sup> /s threshold..... | 87   |
| 36. Model boundary plots at both thresholds during quiet conditions.....            | 90   |
| 37. Energy flux plots of DMSP and model data during various conditions .....        | 94   |
| 38. Deviation plots for NH, OH, and OP models. ....                                 | 96   |
| 39. Energy flux plots of DMSP and model data during storming .....                  | 98   |

## List of Tables

| Table   | Page |
|---|------|
| 1. Kp grouping used in OH model .....   | 28   |
| 2. OH model Kp distribution of analyzed spectra.....                              | 28   |
| 3. DMSP satellite data file example.....  | 39   |
| 4. List of dates investigated. ....   | 40   |
| 5. Energy flux thresholds .....   | 41   |
| 6. DMSP Threshold Crossing Data.....  | 45   |
| 7. Number of threshold crossings obtained for each model.....                     | 53   |
| 8. Definitions of data subcategories.....   | 54   |
| 9. DMSP threshold crossing statistics.....  | 58   |
| 10. DMSP threshold crossing regression analysis .....                             | 62   |
| 11. DMSP threshold crossing regression analysis with MLT groupings.....           | 65   |
| 12. Data loss percentages.....  | 67   |
| 13. Model ratio estimates.....  | 74   |
| 14. Lowest average model deviations .....   | 78   |
| 15. Prediction efficiency scores .....  | 80   |
| 16. Prediction efficiency scores for seasonal grouping. ....                      | 81   |
| 17. Skill scores .....  | 83   |
| 18. Skill scores for seasonal grouping. ....                                      | 84   |
| 19. Comparison of statistics using different thresholds.....                      | 88   |
| 20. Prediction efficiency scores using 0.6 erg/cm <sup>2</sup> /s threshold ..... | 88   |
| 21. Top prediction efficiency scores in each subcategory .....                    | 91   |

| Table  | Page |
|--|------|
| 22. Corroborated categories using both energy flux thresholds. | 92   |
| 23. Small-scale study parameters.....                          | 93   |
| 24. Statistical scores for small-scale study .....             | 97   |

# COMPARATIVE STATISTICAL ANALYSIS OF AURORAL MODELS

## I. Introduction

### 1.1 Motivation

Several governmental agencies, including the Department of Defense (DoD), increasingly rely on highly technological assets operating in the space environment to achieve national security objectives, and satellite operations have become an integral component of the execution of the national defense strategy of the United States. An increased dependence on these assets requires that efforts to mitigate risk remain a top priority.

Some of space asset's vulnerability is related to the highly variable conditions of the space environment, often termed space weather. Space weather, broadly defined, refers to fluctuations in solar activity and solar wind conditions that couple to earth's atmosphere via magnetospheric and ionospheric processes. This coupling can cause substantial increases in the density of highly energetic, charged particles in the satellite environment. In extreme cases, the conditions can become hazardous enough to damage to the fragile electronics on which the asset relies, jeopardizing its sustainability.

A complete theoretical understanding of the interplay among the complex physical processes that influence space weather conditions is not imminent. Thus, many research efforts have focused on developing and honing various models to better predict

and forecast the onset, duration, and severity of changes in the earth's space weather environment. The DoD has assumed a significant role in the development of better models because the ability to effectively and reliably model space weather phenomena provides the framework from which a strategy to protect space assets can be formulated. From a sustainability perspective, an accurate prediction of unfavorable conditions can afford satellite operators the time to execute contingency processes to shut down and/or shield the assets. But accurate modeling can also enhance operations by predicting periods where an asset's performance (or an adversary's asset) will be degraded.

## 1.2 Research Topic

Auroral precipitation models have been extensively used for estimating GPS and other communication satellite disturbances (Newell et al., 2010a). The auroral oval represents one candidate within the space weather framework well suited for modeling because its characteristics are a direct manifestation of the space weather conditions. In fact, auroral precipitation models have existed for several decades, and studies of the statistical systematics pertaining to high-latitude particle precipitation have proved very useful to the space weather community (Hardy et al., 2008). The oval in question refers to an annular region of significant thickness that encircles the magnetic north and south poles. Here, charged particles, originating in the earth's magnetosphere, constantly precipitate into the upper atmosphere along the planet's geomagnetic field lines.

This study specifically focuses on the systematic behavior of diffuse auroral precipitation, which is a pervasive and large-scale phenomenon. Even during quiet conditions, energy flux measurements can be used to discern the location of the precipitation boundaries. However, during geomagnetic storming, the equatorward

boundary of the oval predictably expands, resulting in a physical manifestation that is well suited for study and analysis.

The scope of this study supports taking a limited approach with regard to the complex characteristics of the particles precipitating into equatorward region of the oval. Integral energy fluxes will be used based upon the commonly accepted assumption of isotropic particle precipitation. Furthermore, no distinction will be made among the various types and characteristics of the particles forming the aurora. To that end, only total particle counts will be analyzed, and ion and electron energy fluxes will be summed together. Thus, the research conducted here will purposely not showcase the full capability of many of the models under review, some of which take great effort to model the behavior of specific particle types. Nevertheless, taking this limited view is justified because there have been few objective studies designed to measure, even in the most generic sense, how accurately models depict the extent of the oval.

### **1.3 Research Objective**

This study seeks to objectively quantify the accuracy of different auroral models. Researchers, over the years, have developed a multitude of different auroral precipitation models based on a variety of different methodologies. Generally speaking, each model possesses its own strengths and weaknesses by virtue of its design. However, only recently have efforts been made to compare how well different models predict changes in the auroral oval in response to various geomagnetic conditions.

In 2010, Newell et al. conducted a comparative study of four auroral precipitation models. This research dealt with how accurately each model predicted instantaneous auroral power by comparing each model's results to synoptic UV images from NASA's

Polar satellite. In this study, a similar methodology will be applied to a different dataset. Integral DMSP energy flux data will be used to identify the spatial extent of the equatorward boundary at a specific point along the oval's boundary. Although a single DMSP satellite's transit through the polar region is a poor synoptic representation of the oval, this specific crossing point can be easily compared to the corresponding output of a precipitation model's output, allowing a suitable comparison between the two. The DMSP data archives contain a large amount of easily accessible data, which will permit the creation of a sizeable and statistically significant dataset that includes a variety of conditions obtained at a variety of locations around the polar oval.

The equatorward extent of the auroral oval will be determined using the DMSP satellites' energy flux data. The DMSP results will be compared to the energy flux output of five auroral precipitation models given the same input parameters. The five models are: (1) the Hardy K<sub>p</sub> model from 1985; (2) a 2008 update to the Hardy K<sub>p</sub> model, provided by Dr. Chin at the Air Force Research Laboratory (AFRL); (3) the OVATION Prime model, developed by Newell and colleagues; (4) a physics-based model developed by coupling data from the Space Weather Modeling Framework (SWMF) to a Ring Current model maintained at the Community Coordinated Modeling Center (CCMC) at NASA-Goddard; and (5) results obtained from the Assimilative Mapping of Ionospheric Electrodynamics (AMIE) program provided by colleagues at the University of Michigan. Quantitative analysis of difference between the models' boundary locations compared to the determined boundary using the DMSP flux data will permit an objective, albeit partial, assessment of each model's accuracy.

## **1.4 Document Structure**

This document is arranged into five chapters. Chapter II includes the theoretical framework of the physical processes that create the auroral oval. It additionally discusses other important concepts associated with auroral modeling and provides background information on each of the models. Chapter III explains the methods used to obtain and analyze the data for this study. Chapter IV contains the results of the analysis and their relevance and includes a determination of the most accurate model. In Chapter V, a concise summary of the results and suggestions for subsequent experimentation and investigation will be provided.

## **II. Theory and Background**

This chapter provides theoretical material and background information relevant to this study. It is divided into four main sections. The first section contains a description of important auroral processes, including the solar wind, magnetic reconnection, magnetospheric particle flow, coupling to the ionosphere, and auroral currents and emissions. The second section of this chapter introduces specific concepts associated with the auroral oval's boundary and discusses a useful taxonomy. In the third section, background information relevant to auroral observation and measurement is provided. This includes describing the K<sub>p</sub> index and DMSP data characteristics. The final section provides background information on each of the five auroral models that will be utilized in this study.

### **2.1 Theoretical Background**

From a purely phenomenological point of view, the aurora is simply the emission of energy resulting from atomic and molecular excitation at altitudes between 100 and 300 km (Prölss, 2004). The neutral gas excitation occurs when energetic charged particles precipitating into the earth's atmosphere collide with the various atmospheric gases (Prölss, 2004). The aurora's most noticeable characteristics are the vibrant bands of light arcing throughout the polar night sky. But, this highly dynamic and often times finely structured aurora represents a specific type of aurora—discrete aurora.

In the late 1960s, the existence of a relatively structureless band of large-scale auroral precipitation was observed with both ground- and space-based sensors. The lack of structure led to its eventual classification as diffuse aurora. Shortly thereafter, a satellite launched as part of the International Satellites for Ionospheric Studies (ISIS)

program observed a global pattern of structureless, auroral luminosity encircling the entire geomagnetic pole. This confirmed the diffuse auroral phenomena was occurring in both the day and night hemispheres (Paschmann, 2003). Today, through comprehensive imaging studies, it is known the auroral oval describes of an elliptical ring of varying thickness whose center is displaced anti-sunward of the magnetic pole. The radii of the ring's inner and outer boundaries expand and contract in response to changing solar wind and magnetospheric parameters. The thickest part of the ring and its most equatorward extent are always found on the antisunward side of earth. The schematic in Figure 1 depicts the general shape of the polar oval, showing how it varies diurnally.

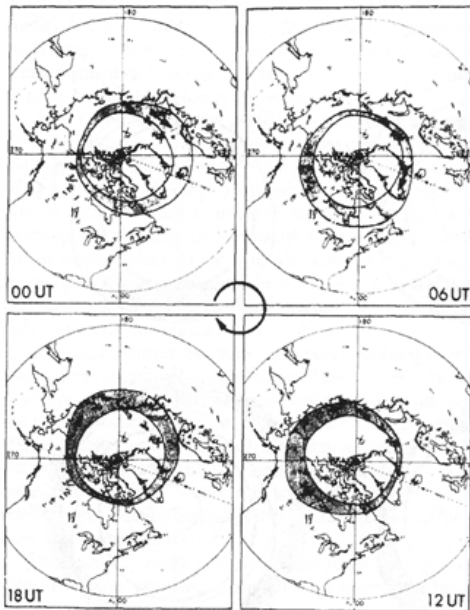


**Figure 1. Schematic of polar oval showing the characteristic diurnal migration (Whalen, 2001).**

The particles responsible for the diffuse aurora are prevalent in the equatorward regions of the oval and precipitate, to some extent, during all levels of geomagnetic conditions. Even though the diffuse emissions are typically too dim to observe with the

naked eye, measurements have since determined the diffuse aurora is responsible for 50-80% of the total energy input into the upper atmosphere (Whalen, 2001). Thus, the equatorward boundary of the oval is one of the most well-suited locations to measure the performance of various auroral models during a variety of conditions.

The molecular light emissions observed on the earth, whether part of the diffuse or discrete aurora, are actually the last link in a long chain of processes. The schematic shown in Figure 2 describes this linkage. An understanding of how the equatorward boundary of the oval changes requires knowledge of the solar wind and the Interplanetary Magnetic Field (IMF), the individual and coupled dynamics of the magnetosphere and ionosphere, and the complicated chemical processes occurring in the earth's atmosphere.

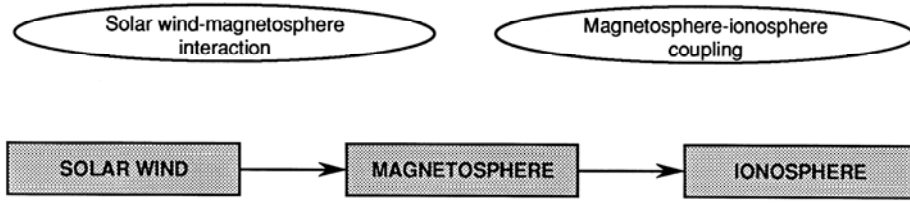


**Figure 2. Auroral Process Chain (Akasofu, 1981).**

### 2.1.1 The Solar Wind

The auroral process begins when the continual stream of charged particles in the solar wind interacts with the earth's magnetic field. The solar wind is highly conductive, collisionless, magnetized plasma emitted from the sun's corona. Because the plasma is highly conductive, the sun's magnetic field is carried along by it. The sun's rotation causes the magnetic field lines to bend into the spiral shape depicted in Figure 3. This accounts for the characteristic shape of the Interplanetary Magnetic Field (IMF), which permeates the entire solar system. The specific orientation of the IMF with reference to

the ecliptic plane (i.e., its  $B_z$ -component) is associated with geomagnetic conditions favorable to producing aurora. Additional information can be found in Tascione (1998).

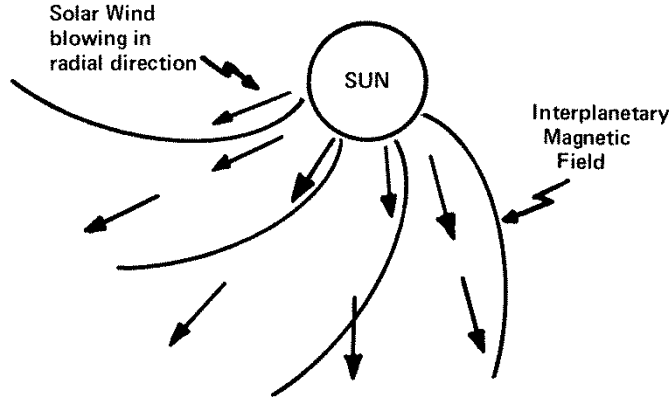


**Figure 3. Depiction of IMF's spiral orientation (Tascione, 1988).**

The vast majority of the solar wind is deflected around the earth. The impinging pressure of the solar wind particles exerts a force on the earth's dipolar field, forming a bow shock, analogous to the aerodynamic shock formed around a blunt obstacle (Tascione, 1988). Inside of this shock boundary, there exists a finite region where the largely dynamic pressure of the solar wind equals the oppositely directed magnetic field pressure of the earth. This results in the formation of the magnetopause, a distinct boundary that shields the magnetosphere from the vast majority of solar wind particles. The sunward side of the magnetosphere is compressed into an ellipsoid shape. On the anti-sunward side, the magnetosphere stretches well beyond  $60 R_E$ , forming a long magnetotail in which the geomagnetic field lines are extremely elongated (Prölss, 2004). The magnetospheric cusp describes the separation region between the field lines comprising the day- and night-sides of the magnetosphere. A schematic representing the

compression of field lines on the sunward side and extension of field lines on the anti-sunward side is provided in Figure 4.

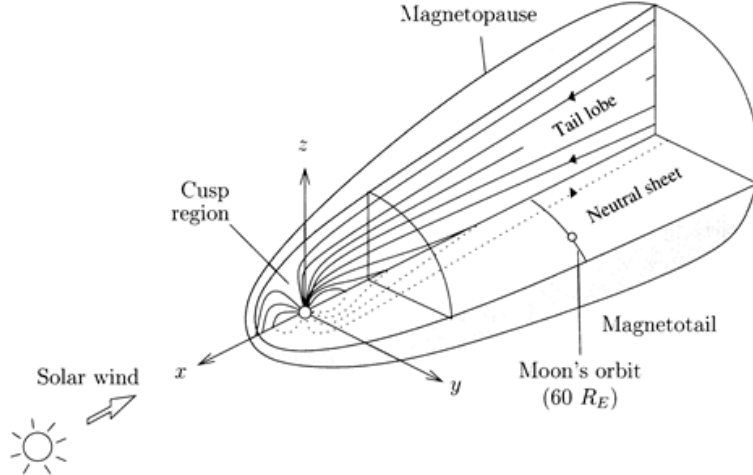


**Figure 4. Depiction of earth's magnetosphere (Prölss, 2004).**

### 2.1.2 Magnetic Reconnection

Due to the magnetopause, the solar wind plasma cannot precipitate directly into the auroral oval, but it is the only source of plasma that can replenish particle losses occurring in the continuous auroral process (Prölss, 2004). This condition necessitates the existence of a coupling mechanism that allows some particles to cross the magnetopause and to enter the earth's magnetosphere. Research has shown the rate of inelastic losses in the ionosphere (e.g., auroral emissions) requires approximately 0.1% of the incident solar wind particles to sustain the process (Tascione, 1988).

It is largely believed that an opening and reconnection process overcomes the otherwise solid boundary of the magnetopause and supplies the magnetosphere with approximately 90% of its energy (Prölss, 2004). The earth's magnetic field can be

thought of as a large magnetic dipole with an asymmetric, albeit closed, magnetic field. Both footpoints of a closed field line terminate on the earth's surface. However, the theoretical concept of magnetic opening provides a mechanism to defeat the otherwise closed system.

At places where the IMF and the earth's geomagnetic field have opposite polarity, a neutral point can form that breaks apart a closed field line. This allows the newly freed ends to be swept along with the solar wind stream toward the magnetotail. Solar wind plasma becomes associated with this open field line, and when the broken field line reconnects somewhere on the anti-sunward side of the earth, the plasma is introduced into the magnetosphere. This process, termed magnetic reconnection, replenishes the reservoir of particles and also releases energy (Prölss, 2004). Reconnection occurs within  $200 R_E$ , but near earth reconnection ( $\sim 20\text{-}30 R_E$ ) often correlates to faster convective flows within the plasma sheet and an expansion of the auroral oval (Ohtani et al., 2004).

Neutral points may form during both IMF-northward and IMF-southward conditions. However, it has been demonstrated empirically that when the earth enters a region of southward orientation, more particles enter the magnetosphere, and geomagnetic storming is intensified. Additional information regarding reconnection is contained in Prölss (2004) and Paschmann (2003).

### 2.1.3 Magnetospheric Particle Flow

Reference was made in Section 2.1.1 to the stretching of the magnetic field lines on the anti-sunward side of earth. The highly extended lines in the magnetotail are characterized by a sharp reversal in the tangential component of their polarity. The

graphic shown in Figure 5 demonstrates the extreme stretching of the field lines in the magnetotail.

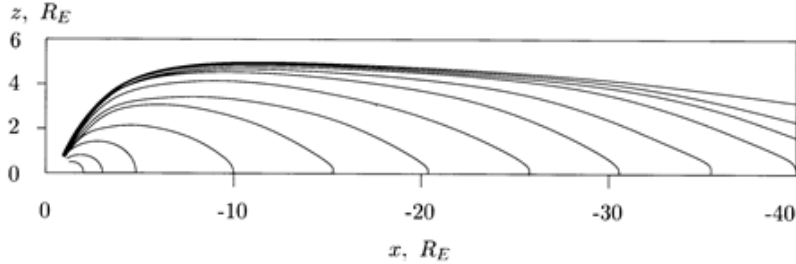


**Figure 5. Geomagnetic field lines in the x-z plane of the earth's magnetotail (Prölss, 2004).**

This feature creates a region along the ecliptic plane known as the magnetically neutral sheet, which permits the formation of a surface current that flows across the tail from dawn to dusk. The current creates a convection electric field oriented in the same direction. The perpendicular orientation of the electric (east-to-west) and magnetic (south-to-north) fields in and near the ecliptic plane of the magnetotail results in both ions and electrons in this region drifting toward the earth as a result of an  $\mathbf{E} \times \mathbf{B}$  drift. This drift is given by

$$\mathbf{u}_{ExB} = \frac{\mathbf{E} \times \mathbf{B}}{B^2} \quad (1)$$

in which there is no dependence upon particle charge or energy.

As the particles drift closer to earth, two things occur. First, they are heated and compressed but maintain a nearly Maxwellian energy distribution (Paschmann, 2003). Second, they encounter a region, as is shown in Figure 5, where the dipole field is far less elongated than it was in far regions of the magnetotail. In this region, there exists a stronger magnetic field gradient perpendicular to the field lines. The increase in energy

and the changing shape of the magnetic field cause the gradient and curvature drift to become dominant. This quantity is often expressed as total particle drift and is given by

$$\mathbf{u}_D = \left(\frac{m}{2q}\right) (v_\perp^2 + 2v_{||}^2) \frac{\mathbf{B} \times \nabla \mathbf{B}}{B^3} \quad (2)$$

which is dependent upon both particle charge and kinetic energy. For the purposes of the discussion salient to this study, it is sufficient to introduce a simplifying assumption, as is done by Prölss (2004). The total drift in the vicinity of the mirror points is significantly less than that found at the equatorial plane due to the parallel component of the velocity approaching zero and the reduction in the field gradient. To reasonable approximation, then, it is possible to ignore curvature drift component in the Equation (2), in which case, the total drift is equal to the gradient drift. Between approximately  $10-12 R_E$ , the dominance of the gradient drift begins to manifest itself on the highest energy particles. They are turned perpendicularly to the orientation of the convective flow, and because of the charge dependence, positively charged ions turn to the west and electrons turn toward the east (Paschmann, 2003).

The dominance of the gradient drift over the  $\mathbf{E} \times \mathbf{B}$  drift as a function of particle energy ultimately implies a point of closest approach for the lowest energy ions and electrons. This region in the nightside magnetosphere maps along the associated field lines and demarcates the equatorward boundary of diffuse precipitation in the oval (Prölss, 2004). The following equation establishes the distance from earth at which this point occurs:

$$L = \frac{3 W_{perp}}{|q| R_E E_{con}} \quad (3)$$

where  $W_{perp}$  is the kinetic energy perpendicular to the magnetic field and  $E_{con}$  is the convective electric field mapped from the solar wind. This relation clearly demonstrates two important characteristics. First, as the convective electric field increases, as it does during periods of increased geomagnetic activity, the distance of closest approach decreases. This gives particles of certain energy access to field lines whose footpoints map to lower latitudes, and the equatorward boundary of the auroral oval expands (Prölss, 2004).

Additionally, the effect of the energy term, as was discussed earlier, implies lower energy particles can be found closer to the earth. This has been validated through observation. The graphic in Figure 6 demonstrates electron flux counts in discrete energy channels. The arrows show the onset of precipitating electrons. The precipitation onset of more energetic electrons is observed at more poleward latitudes, which is consistent with their association with field lines farther from the earth. This has been found to be a energy onset pattern that is particularly characteristic of the equatorward boundary located in the evening and night sectors (Gussenhoven et al., 1981).

#### 2.1.4 Ionospheric Coupling

Charged particles spiraling along field lines will maintain their first adiabatic invariant under static conditions. This means that as the intensity of the magnetic field changes, the particle's perpendicular velocity increases. Conservation of energy requires the parallel component of the spiraling particle's velocity to eventually go to zero, and an oppositely directed gradient force reflects the particle. This condition, by itself, would result in a rapid emptying of the loss cone and an unsustainable auroral process. In effect, most particles would bounce between their mirror points well above the

atmospheric regions where the aurora forms. Since the auroral is pervasive, there must exist some mechanism to refill the loss cones. Scattering processes are thought to provide the means by which the loss cone population is replenished, sustaining the auroral process.

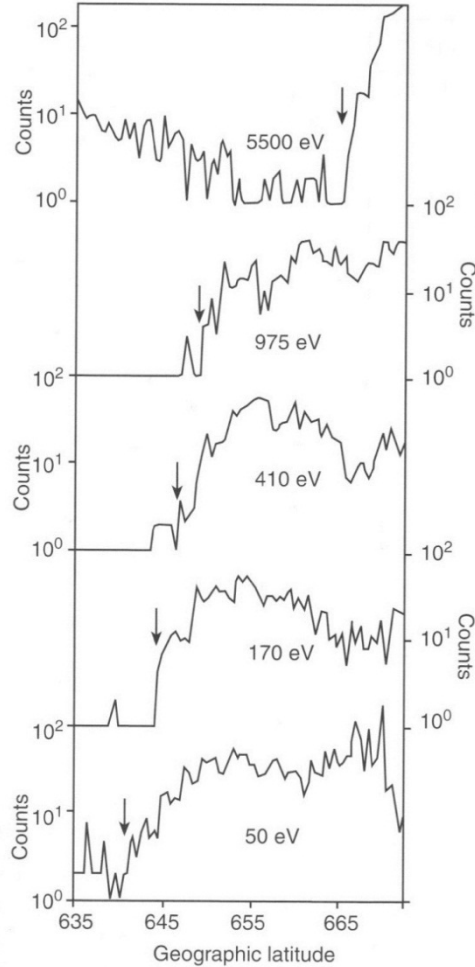


**Figure 6.** DMSP satellite particle counts in a few of the sensor's discrete energy bins for a satellite pass in the night sector. Arrows correspond to coordinates at which significant increase in number flux occurs. Boundary associated with higher energy particles is observed at higher latitudes consistent with curvature drift dominance (Gussenhoven et al., 1981).

For the more massive ions, scattering largely occurs because of the specific shape of the field lines in the magnetotail. Although they are closed, the field lines in question

exhibit a sharp reversal in the field lines of the nightside magnetosphere that can result in pitch angle scattering into the loss cone. This occurs because the typical ion gyroradius, which is much larger than that of an electron, becomes comparable to the radius of curvature of the magnetic field in the narrow region near the ecliptic plane (Paschmann, 2003).

As is given by Prölss (2004), particle motion can be described by a ratio of the field line curvature to the particle gyroradius:

$$\kappa^2 = \frac{q L B_n^2}{m v B_{lobe}} \quad (4)$$

where  $B_n$  represents the perpendicular magnetic field strength in the region spanning the current sheet and  $B_{lobe}$  is the larger tangential field strength immediately above and below the current sheet.  $L$  represents the scale length ( $\sim 1000\text{-}10,000$  km) for the reversal of polarity across the current sheet. When  $\kappa^2 \cong 1$ , strong pitch-angle scattering occurs. For protons in the mid-tail regions of the ionosphere, this relation is satisfied for a wide variety of energies spanning 30 eV to 190 keV, which agree closely with observed proton energies in the equatorward region of the auroral oval (Paschmann, 2003).

For electrons in the plasma sheet, the mechanism that fills the loss cone for the diffuse aurora is thought to be pitch angle diffusion brought about by wave-particle scattering. Scattered electrons may obtain velocities that are parallel to the magnetic field lines in the region. This change in velocity puts the electrons into the loss cone, and they are allowed to precipitate down into the upper atmosphere (Prölss, 2004). This process is shown schematically in Figure 7.

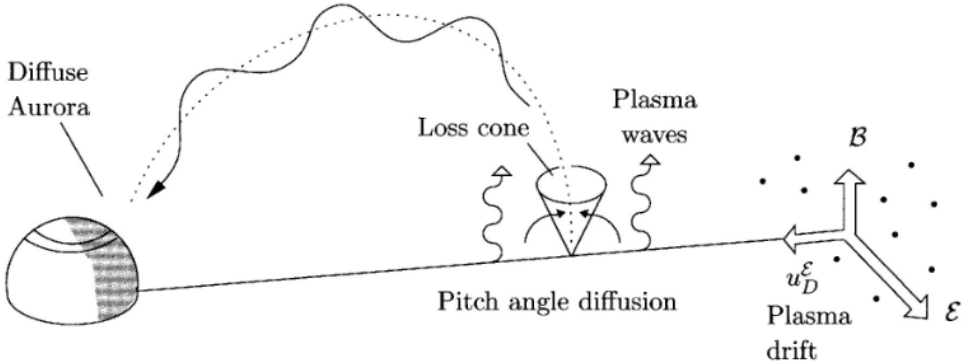


**Figure 7. Pitch angle diffusion in plasma sheet (Prölss, 2004).**

Pitch-angle scattering, therefore, forms the critical bridge between the plasma sheet along the equatorial plane and the upper atmosphere. Additionally, the following conclusions can be drawn. The distant regions of the magnetosphere contribute small electron energy fluxes to the ionosphere. Precipitation increases as a function of increased thermal energy as the particles are brought earthward, where perturbations in parallel velocities are sufficient to move the particles into their respective loss cones (Paschmann, 2003). The loss cone is a function of the ratio between the magnetic fields strength of a field line at the equator to the field strength of the same field line mapped into the polar ionosphere using a quasi-dipole approximation. Typical field strength ratios are on the order of  $10^{-4}$  resulting in loss cone angles  $\sim 1^\circ$  (Paschmann, 2003). For an isotropic temperature distribution of electrons, the fraction of particles in the loss cone is on the order of  $1 \times 10^{-4}$ .

### 2.1.5 Plasma Sheet Topology

As the primary source for diffuse auroral particles, the mapping of plasma sheet to the polar ionosphere is important. Crude approximations can be made using a pure

dipole field. The following equation expresses the magnetic latitude of a footprint to the corresponding L-shell (multiple of  $R_E$ ) at a height  $h$  above the earth's surface

$$\varphi = \arccos \sqrt{\frac{R_E + h}{R_E L}} \quad (5)$$

Using this approximation, the inner and middle portions of the plasma sheet, which exist between approximately 5 and 40  $R_E$ , are threaded by closed geomagnetic field lines which correspond to geomagnetic latitudes (MLATs) between approximately 63-80°. In order to account for the deviations from a pure dipole, various models have been developed. Figure 8 depicts field lines as a function of MLAT. As this model demonstrates, using a simple dipole approximation introduces errors at MLATs greater than 70°.

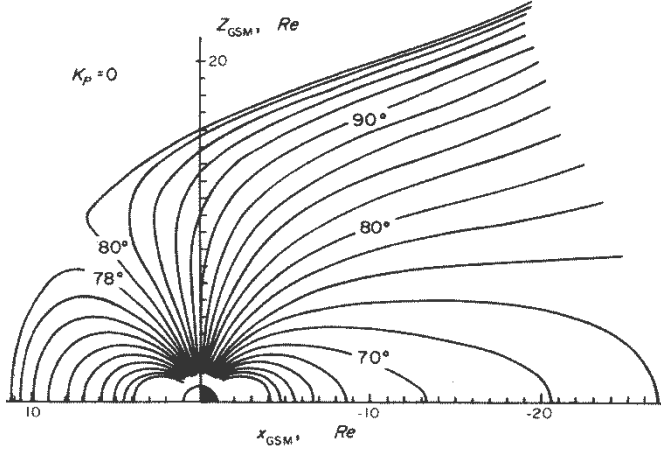


**Figure 8. Geomagnetic field model accounting for asymmetry during quiet conditions ( $K_p = 0$ ). Latitudes depicted are invariant (adapted from Hargreaves, 1995).**

Under all but the most extreme conditions, the auroral zone exists between 60-80° MLAT. As was discussed in the previous section, its equatorward boundary corresponds to the most earthward region of precipitating particles, which conventionally describes the boundary region of the plasma sheet. The connection between the

characteristics of the particles in the plasma sheet and the diffuse auroral oval was made in the mid-1970s (Newell et al., 1996). Since then, subsequent studies have confirmed the measured electron energies in the diffuse aurora are characteristic of the plasma sheet population.

### 2.1.6 Auroral Current System and Emissions

The regions of precipitating particles in the auroral zone form the current linkage between the ionosphere and magnetosphere. The energy transfer between the magnetosphere and the ionosphere is accomplished via field-aligned currents (FAC).

Figure 9 shows a generic schematic of the FAC flowing into and out of the ionosphere in the polar region.

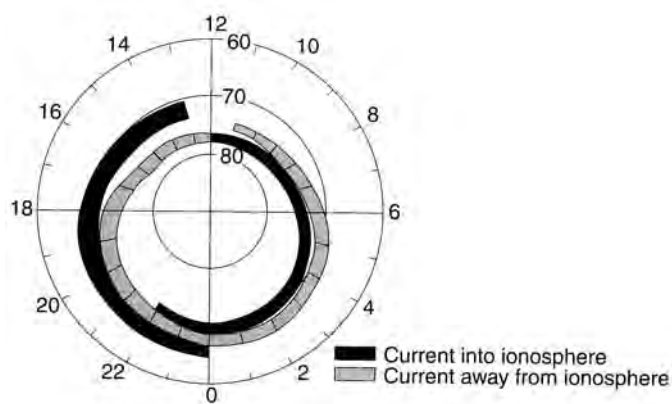


**Figure 9. Characteristic polar region current flows. Latitude is invariant. (adapted from Schunk, 2009).**

The FAC are an integral part of a complex current system that involves the entire polar cap. They are divided into two regions. Region 1 currents are everywhere poleward of Region 2 currents. As depicted in Figure 9, on the dawn side of the polar cap, current flows into the ionosphere in Region 1 and out of the ionosphere in Region 2. This system is reversed on the dusk side. The main distinction between the regions is

that Region 1 currents couple to the solar wind through open magnetic field lines, whereas Region 2 field lines are entirely part of the closed system of the inner magnetosphere (Paschmann, 2003).

The FAC are primarily carried by electrons. When current is flowing into the ionosphere, the upward flowing electrons, sourced in the ionosphere, are comparatively cold and responsible for little neutral gas excitation. More energetic electron populations from the magnetosphere precipitate in regions where current is flowing out of the polar cap. Studies have confirmed that there is very little field-aligned acceleration existing in the quasi-dipolar region of the inner magnetosphere (Paschmann, 2003). Thus, under quiescent conditions, thermalized electrons carry the current, and diffuse aurora is pervasive. However, during active periods, the convective flow from the plasma sheet is increased, and current continuity must be maintained through the formation of magnetic field-aligned electric fields. These are the electric fields that result in accelerated particles responsible for the visible, dynamic auroral displays (Paschmann, 2003).

In order to maintain charge continuity, inbound and outbound currents are connected with horizontal currents flowing across the geomagnetic field lines in the polar ionosphere (Paschmann, 2003). The Hall and Pedersen currents complete the auroral circuitry linking the magnetosphere and ionosphere. Additional discussion of these current systems can be found in Schunk (2009).

An in-depth review of the ionospheric chemistry that results in the auroral radiation exceeds the scope of this research and will not be included here. These processes are discussed at great length in Schunk (2009). One point will be clarified. Auroral emissions occur between ~90-200 km, approximately 700 km below the DMSP

satellite orbits. As can be confirmed by Equation (4), when considering altitudes much less than one earth radius, the field lines are virtually perpendicular to the earth's surface. Thus, the location of a satellite in low-earth orbit correlates closely to the region of the ionosphere where the auroral energy is radiated.

## 2.2 Auroral Oval Boundaries

By the mid-1980s, numerous studies had confirmed that the entire auroral oval, including the subvisual diffuse aurora found near the equatorward boundary, migrated north- and southward in response to magnetic substorming (Newell, et al. 1996). Replicating the full extent of the boundary's shifting nature has remained a primary focus of early and more recent modeling efforts.

Gussenhoven et al. (1981) were responsible for one of the first research efforts of this sort. Gussenhoven's study sought to categorize the oval's boundaries using data gained from DMSP/F2 satellite passes. The boundary coordinates were assigned to the location where the number flux exceeded  $10^7$  elec/cm<sup>2</sup>/s/sr, a value chosen to represent a significant rise above the background flux counts (Gussenhoven, 1981). The results of the research confirmed the existence of a strong correlation between the equatorward boundary's location and the Kp index. Incidentally, this study also discovered the boundary in the pre-noon MLT sectors was more difficult to determine than in the evening sectors, an issue which will be discussed in a later section.

In 1996, Newell and colleagues conducted an extensive study aimed at objectively categorizing the various boundaries that had been discovered within the nightside auroral oval. Physical manifestations throughout the inner magnetosphere associate to specific qualities observed in the energy signatures of the precipitating particles. Newell's study

associates various theoretical precepts with observed features found at locations within the auroral oval. Conveniently, Newell's boundaries were formulated based upon energy flux measurements, consistent with the data obtained in this study and, thus, provide a useful framework.

One example of the type of categorization conducted in Newell's study pertains to the point where the reduced curvature of the magnetic field lines no longer causes pitch angle scattering of the ions near the neutral sheet. This point maps to an observable ion boundary in the auroral oval, known as the ion isotropy boundary. Newell's study also defined two boundaries relating to the oval's equatorward regions. The most equatorward boundary corresponds to the convection boundary formed between the zero-energy population of the plasmasphere and the lowest energy particles of the plasma sheet.

As was described in an earlier section, low energy particles are less influenced by gradient and curvature drifts drift closer to the earth than those with higher energies. The boundary (termed b1e) demarcates the most equatorward location from which measured energies begin to increase, which corresponds to the field lines threading the most earthward regions of the plasma sheet. Its geophysical meaning is, therefore, associated with the zero-energy Alfvén layer and the plasmapause (Newell et al., 1996, 2002). The existence of this boundary can be conceptualized using a DMSP satellite data spectrogram, shown in Figure 10. The b1e boundary, delineated by the black line, corresponds to the onset of low-energy electron energy fluxes that occurs just after 00:27 UT. As was discussed in Figure 6, the energy fluxes initially increase as a function of latitude just inside of the equatorward boundary.

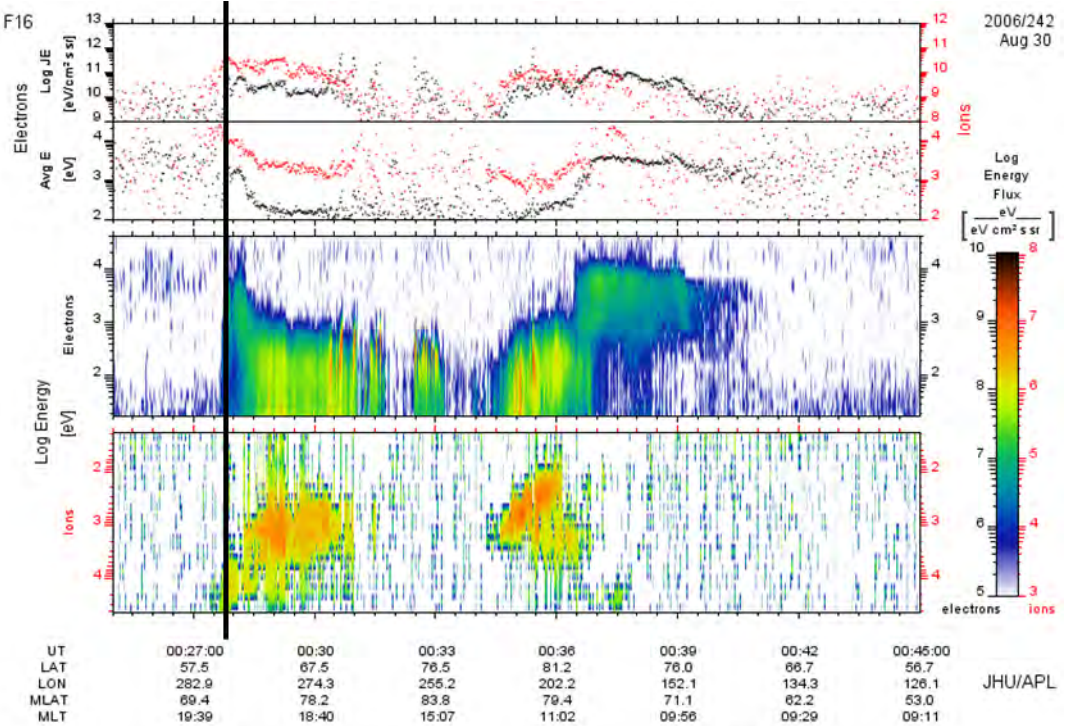


**Figure 10.** Sample DMSP spectrogram obtained on August 30, 2006. The b1e boundary (thick black line) occurs at approximately 00:27:30 UT corresponding to the onset of low-energy electrons. Spectrogram obtained from JHU/APL website: <http://sd-www.jhuapl.edu/Aurora/spectrogram/>

At some point after the onset of particle precipitation, however, the energy flux measurements plateau within the auroral oval. This occurs because the particle energies found within the main plasma sheet have a much more Maxwellian distribution than those that have migrated earthward. The point at which the change in the average energy no longer increases with latitude corresponds to Newell's b2e boundary. This boundary is topologically associated with the most earthward extent of the main body of the plasma sheet.

These two boundaries are useful in the development of this study. The region between the b1e and b2e boundaries clearly demarcates the equatorward extent of auroral precipitation, but various camps support utilizing one or the other (Newell et al., 2002). This study undertaken here has been designed to rank how accurately various models

depict the location of the equatorward boundary of the auroral oval using carefully chosen, fixed energy flux values to designate the effective boundary. The information gained from Newell's taxonomic research merits and justifies using a boundary criterion that is neither the b1e nor the b2e boundary but, instead, corresponds to an energy flux value statistically certain to fall between the two boundaries.

## **2.3 Auroral Categorization and Measurements**

Advancements in computing technology allow today's auroral models to ingest, process, and compile large amounts of space weather data from a multitude of sources. However, despite these advances, the Kp index remains one of the most valuable means of categorizing auroral activity. A brief summary of how this index is determined and utilized will facilitate later discussion.

In Section 2.3.2, the basic operation of the DMSP satellites will be discussed. DMSP has been providing polar region data for decades and has become one of the most prolific sources of data in the near-earth environment. Because DMSP data is integral to this research, some basic information will be provided to establish familiarity which will be relied upon in the remainder of this document.

### **2.3.1 The Planetary K Index**

The planetary K (Kp) index, fielded in 1949, remains a prevalent modeling parameter to this day. It measures geomagnetic activity on a scale from 0 to 9 based upon measurements taken from a network of 13 ground stations. Transient fluctuations in the magnetic field at the earth's surface are induced by changes in the ionospheric and magnetospheric currents (e.g., the ring current), which vary with changes in geomagnetic activity and solar wind conditions (Menvielle & Berthelier, 1991). The Kp index is

determined, in part, by measuring the magnitude of the surface field fluctuations. It is particularly suitable for auroral studies because variations in the earthward boundary of the plasma sheet have been shown to correlate well to the K<sub>p</sub> index value (Wing, 2005). Because of its ubiquity and uniformity, the K<sub>p</sub> index will be used extensively to categorize data sets within this study.

### 2.3.2 DMSP Satellites and Sensors

The Defense Meteorological Satellite Program (DMSP) launched its first satellite in 1963, and the program remains in service. Each DMSP satellite has a nearly polar, sun-synchronous, ~101 minute orbit at ~830-850 km. The polar orbits permit each satellite to transit through the auroral ring twice in each hemisphere (once going northward and once going southward). Optimally, as many as four satellites are in operation at the same time.

In the mid-1970s, specially designed particle detectors were installed on the DMSP satellites to measure the number and energy fluxes of precipitating electrons and ions. The latest in the series of sensors is the SSJ/4, an ion and electron spectrometer that is oriented on the satellites such that it always faces the local zenith. The sensors collect data at one-second intervals and use electrostatic analyzers to measure precipitating electron and ion energy fluxes (eV/cm<sup>2</sup>/s/sr) in one of 20 logarithmically spaced energy channels between 30 eV and 30 keV (Redmon et al., 2010). The DMSP satellites provide one of the best space-based platforms for measuring the precipitating ions and electrons while reducing exposure to back-scattered radiation (Gussenhoven & Hardy, 1983). The spectrogram in Figure 10 is one popular graphical representation of the data obtained from the satellites. In 2006, an upgraded SSJ/5 sensor was installed on DMSP satellite

F17. The SSJ/5 sensor's capabilities are enhanced, but for purposes of this study, its data is indistinguishable from the SSJ/4 data.

## 2.4 Auroral Modeling

The development of more space-based platforms has introduced many different ways to observe and measure auroral activity (Siscoe, 1991). Some platforms, like NASA's Polar satellite, take synoptic measurements and are useful in performing large-scale measurements like hemispheric auroral power. As was just discussed in a previous section, the low orbiting DMSP satellites continue to collect extensive amounts of particle and energy data with high spatial resolution. Other platforms, located well beyond earth's magnetosphere, directly measure ambient solar wind and IMF parameters. These measurements (e.g., solar wind speed, IMF orientation, etc.) have become an integral part of the computations done by more advanced precipitation models. The Advanced Composition Explorer (ACE) satellite, located approximately 1.5M km from earth, is an example of a platform that obtains this type of data. Each of these platforms has enhanced the ways auroral activity can be observed. However, the addition of more and more types of data still requires the modelers to carefully choose how to use this data in order to create the most accurate results. This, in general, has proved to be a formidable challenge.

The data limitations that beset the earliest models meant they were usually developed from statistical studies of empirical data. A better theoretical understanding has allowed more complex processes to be introduced, but most researchers agree that a completely physics-driven model is not imminent. The five models included in this study

span several decades of advancement and understanding. The following sections will provide some basic background information on each of them.

#### **2.4.1 The Hardy Model – 1985 Version**

Data obtained between 1977 and 1980 from more than 27,000 satellite passes of 3 DMSP satellites was utilized in 1985 to create what has become one of the most well-known, empirical auroral models—Hardy and Gussenhoven’s Statistical Model of Electron Precipitation (Hardy et al., 1985). Hereafter, for simplicity, this model will be referred to as the Original Hardy (OH). The OH model depicts the global pattern of electron precipitation in the polar region (in 1987, it was modified to include ion precipitation as well) as a function of MLT, MLAT, and Kp.

The model was developed by performing a comprehensive statistical study. The polar ionosphere was divided into a grid of 1440 sections comprised of 48 MLT bins (30-minute sections) and 30 MLAT bins between  $50^{\circ}$ - $90^{\circ}$  ( $1^{\circ}$  increments between  $60^{\circ}$ - $80^{\circ}$  and  $2^{\circ}$  increments elsewhere). Seven individual grids were then assembled based upon grouping Kp index values (Hardy et al., 1985). The seven groupings are listed in Table 1. Hardy’s study used approximately 14.1 million individual spectra, whose Kp distribution percentages are shown in Table 2. Group 7, despite comprising 9 discrete Kp levels, is the group with the smallest population of observed events. Extremely high Kp events are quite rare, and this poses a challenge for both the models and the studies designed to validate them.

**Table 1. Original Hardy model Kp grouping (Hardy et al., 1985).**

| Group | Kp Values                              |
|-------|--|
| 1     | 0, 0+                                  |
| 2     | 1-, 1, 1+                              |
| 3     | 2-, 2, 2+                              |
| 4     | 3-, 3, 3+                              |
| 5     | 4-, 4, 4+                              |
| 6     | 5-, 5, 5+                              |
| 7     | 6-, 6, 6+, 7-, 7, 7+, 8-, 8, 8+, 9-, 9 |

**Table 2. Original Hardy model Kp distribution of analyzed spectra (Hardy et al., 1985).**

| Group | Percent Observed |
|-------|------------------|
| 1     | 8.0              |
| 2     | 23.8             |
| 3     | 26.9             |
| 4     | 21.9             |
| 5     | 10.5             |
| 6     | 5.3              |
| 7     | 3.6              |

In each grid element, the average and standard deviation of the differential number flux in each of the discrete energy channels of the SSJ detector was used to calculate an average differential number flux spectrum for each group of Kp indices. To facilitate mapping the results, the integral number flux ( $\text{cm}^2/\text{s}/\text{sr}$ )<sup>-1</sup> and the energy flux (keV/cm<sup>2</sup>/s/sr) were then determined, based upon the differential number flux and the centerline energy of a respective energy bin. Noise was eliminated by using a smoothing function and averaging the values in contiguous grid elements three times (Hardy et al., 1985). Each computed value was mapped to a polar plot for a given Kp level. The result is seven polar maps, one for each Kp group, displaying number flux, energy flux, or average energy in each MLT-MLAT grid element.

Figure 11 displays the energy flux output for quiet (Kp 1) and stormy (Kp 6) conditions respectively. An interpolating function has been applied to reduce the MLAT grid size to  $0.1^\circ$  versus  $0.5^\circ$ . These plots clearly depict the significant changes in total energy and spatial extent of the auroral zone precipitation during different conditions. During high-Kp conditions, the expansion of the equatorward boundary of the oval is readily apparent.

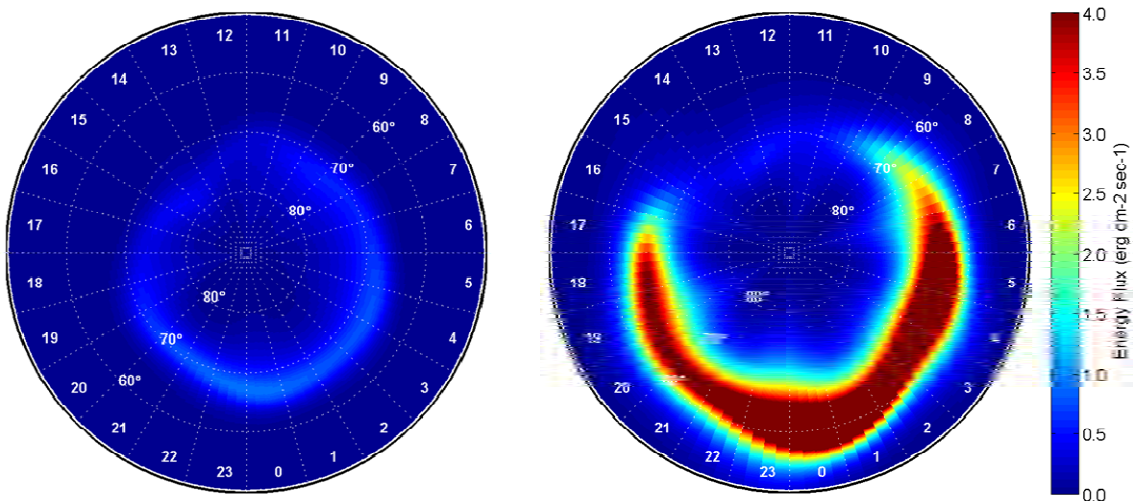


**Figure 11.** OH model polar plots showing Kp 1 (left) and Kp 6 (right).

#### 2.4.2 The OVATION Prime Model

One significant simplification of the Hardy model is that it does not distinguish between particles whose energy spectra are quite disparate. Different precipitation regions move about continually, therefore, averaging at fixed MLAT-MLT locations mixes the different types together (Sotirelis & Newell, 2000).

Distinguishing among different particles was one tenet of the OVATION Prime (OP) model, released by Newell and colleagues in 2009. This model parameterizes auroral electrons into three distinct types and separately accounts for ions. Two electron

classifications account for accelerated particles. Newell names these monoenergetic energy events, attributed to electric field acceleration, and broadband acceleration, produced by Alfvén wave dispersion. Any electrons not meeting either of the two previous definitions are classed as diffuse. This model does not make any distinction among ions, but it does consider them separately from electrons (Newell et al., 2009).

Electrons are categorized by assessing DMSP energy flux data which enables the model to distinguish between the two types of electron acceleration. The DMSP satellite's SSJ/4 sensor measures energy flux in each of 20 discrete bins. For a monoenergetic event, the energy flux must drop to 30% of the maximum of the peak channel measurement within two energy steps above or below the peak. Contrarily, broadband acceleration is categorized when three or more channels have energy flux measurements above  $2.0 \times 10^8 \text{ eV/cm}^2/\text{s/sr/eV}$  and at least one of the channels satisfying this criterion occurs in an energy channel exceeding 140 eV (Newell et al., 2009).

The OP model also maps to a polar MLT-MLAT grid. The model's resolution is  $0.25^\circ$  MLT and  $0.50^\circ$  MLAT between  $50^\circ$ - $90^\circ$ . In each grid element, energy flux is computed ( $\text{erg/cm}^2/\text{sec}$ ), but the output is not discretely parameterized by Kp index. Instead, the OP model is parameterized by solar wind driving, which its researchers believe is best represented by the following solar wind coupling function,  $d\phi_{MP}/dt$ , *magnetic flux at the magnetopause*. This equation is given by

$$\frac{d\phi_{MP}}{dt} = v^{4/3} \cdot B^{2/3} \cdot \sin^{8/3} \left( \frac{\theta}{2} \right) \quad (6)$$

where  $v$  is *bulk solar wind velocity* (km/s),  $B$  is  $(B_y^2 + B_z^2)^{1/2}$  (nT) and  $\theta$  is *IMF clock angle*. The solar wind data comes from the OMNI2 data set supplied by NASA Goddard.

The OMNI2 data set contains solar wind data obtained from a variety of satellites and is tabulated once per hour. Timing is reconciled by using data pre-propagated to  $\sim 10 R_E$ , the approximate location the bow shock (Newell et al., 2010b). The reconciliation is necessary because data concerning the solar wind incident on the earth's magnetosphere is often measured by a satellite far upstream from the magnetopause (e.g.,  $\sim 225 R_E$ ).

This solar wind coupling function serves as an organizing parameter for the model, and the statistical analysis is based upon least squares regression of the form

$$\text{Auroral Power} \left( \frac{d\phi_{MP}}{dt} \right) = a + b \cdot \frac{d\phi_{MP}}{dt} \quad (7)$$

where the auroral power is calculated in each grid element. There are 46,080 individual regression fits which constitute the model (4 categories x 120 MLAT bins x 96 MLT bins). The model then calculates the energy flux in a specific MLT-MLAT bin by taking the product of the fitted estimate of the auroral intensity and the probability of observing the specific type of aurora. Seasonal variations in each of the four types of auroral particles are also considered. A season is defined as a 90-day period centered on the respective equinox or solstice (Newell et al., 2010b). The seasonal dependence accounts for different energy input into the ionosphere. For a given solar wind condition, hemispheric energy flux in winter is increased by a factor of 1.18-1.30 over summer (Newell et al., 2010b).

One assumption the OP model makes is that all types of aurora are isotropic. Thus, all flux values are multiplied by  $\pi$  to eliminate any directional dependence. This assumption is both reasonable and justified, but it may slightly overestimate broadband and monoenergetic auroral fluxes, which tend to be field aligned (Newell et al., 2009). In

a given MLAT-MLT grid element, the total energy flux is simply the sum of each of the fluxes calculated for the four types of auroral particles described above.

For the purposes of this study, only total flux will be considered. The polar plots in Figure 12 provide two examples of the OP model’s output during different geomagnetic conditions. The general shape of the auroral oval is relatively easy to discern in both plots, particularly between dusk and dawn. For periods of heightened geomagnetic storming, the model produces a larger and more energetic auroral zone. Very large energy flux values are observed in the night hemisphere, and the equatorward boundary has expanded such that it is well below 60° MLAT.

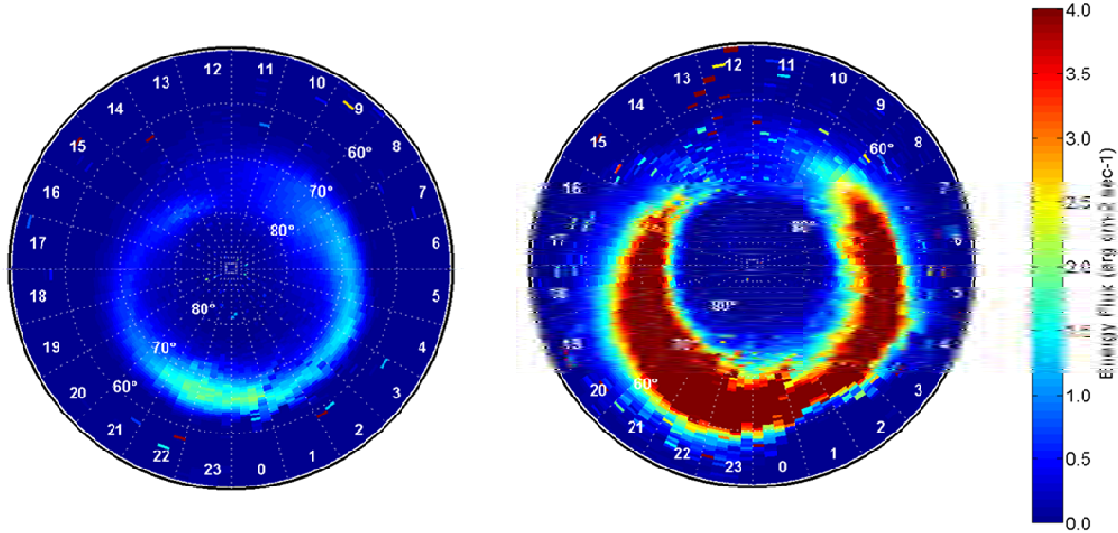


**Figure 12.** OP polar plots showing quiet solar driving (left) versus storming/Kp 6+ (right).

#### 2.4.3 The Hardy Model – 2008 Adaptation

In 2008, Hardy and colleagues reinvestigated their study of electron precipitation at high latitudes. Like the original research from 1985, this study conducted a statistical analysis of DMSP data, only now more than 600 million individual spectra were used

(Hardy et al., 2008). This model distinguishes itself by using probability distributions to characterize different particle populations in lieu of average energy flux values.

This adaptation to the OH model was motivated by the perception of an inherent problem in the way the OH model assumption that all particle populations represent unimodal, normal distributions. Statistically speaking, this assumption implies the average value corresponds to the most probable (Hardy et al., 2008). However, the various regions of the magnetosphere migrate within the magnetosphere as functions of geomagnetic activity, and as a result, the connection between the ionosphere and magnetosphere along the geomagnetic field lines also changes. Thus, particles indigenous to specific regions of the magnetosphere may under certain conditions precipitate into different regions of the ionosphere, and taking simple averages may lead to the mixing of precipitating particle characteristics. The researchers argue the final results may not represent characteristics associated with any of the original source particle populations.

In the new study, more highly refined analysis of the DMSP data confirmed that the probability distributions of electrons within a specific grid element were always lognormal distributions and often multimodal (Hardy et al., 2008). This consideration was factored into the development of new precipitation patterns, whose modeling enhancements will be referred to as the New Hardy (NH) model in this study. Comparisons between OH and NH output indicate a similar structure with large areas of agreement. However, Hardy et al. (2008) demonstrated there is a less than 10% probability that the particle precipitation in any particular MLAT-MLT-Kp grid element satisfies the unimodal assumption.

The NH model adjusts the OH model's output based upon this statistical conclusion that in a given MLT-MLAT-Kp grid element, there is a low probability of the average integral flux coinciding with the most probable. Figure 13 shows two examples of synoptic plots of the NH model's energy flux calculations during quiet and stormy conditions. Again, an interpolating function allows a  $0.1^\circ$  MLAT resolution. The model's equatorward boundary during stormy conditions does not exhibit the typical bulging near the midnight MLT sectors, and generally the plot is less energetic than was found with the OH model.

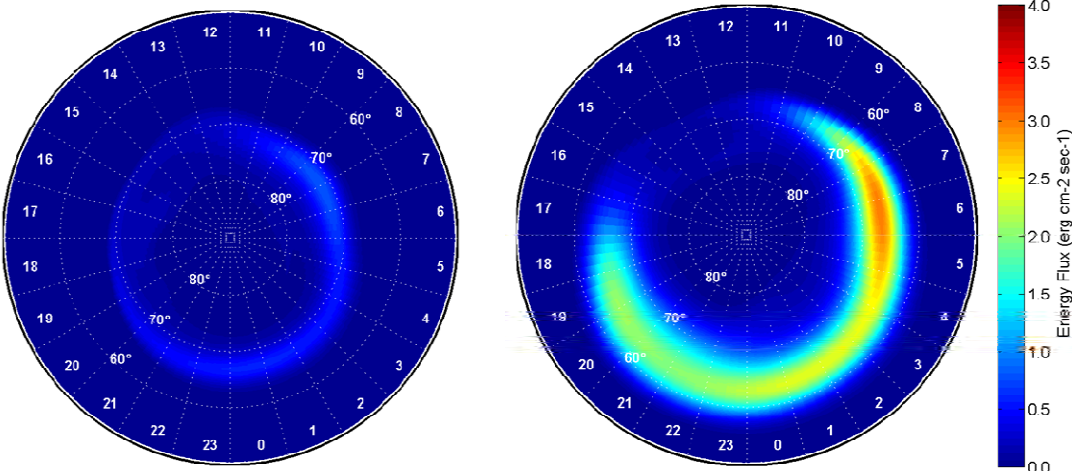


**Figure 13.** NH polar plot showing Kp 1 (left) and Kp 6 (right).

#### 2.4.4 Space Weather Modeling Framework Model

The entire Space Weather Modeling Framework (SWMF) consists of 10 major components representing the entire domain of solar-terrestrial space weather. The entire SWMF chain is maintained at NASA-Goddard. A method to calculate auroral precipitation patterns requires coupling the Global Magnetosphere (GM) component of the SWMF to the Fok Ring Current (RC) model.

In this process, the SWMF/GM model provides a physics-based magnetohydrodynamic (MHD) characterization of the earth's magnetosphere (Tóth et al., 2005). The Fok RC model generates a kinetic description of the global particle distribution in the inner magnetosphere in the energy range of 1-300 keV. By taking advantage of the dynamic electric and magnetic fields modeled by SWMF/GM, the Fok-RC model is capable of computing the equatorward boundary of auroral precipitation patterns (Zheng, 2012).

The dynamics of the ring current have been demonstrated to be closely tied to geomagnetic storming. The ring current flows in a westerly direction in the near-earth region, between 3 and 6 earth radii. Particles in the current region are lost as a result of pitch angle diffusion and subsequent collisions in the upper atmosphere in the mid and high latitudes (Prölss, 2004).

For simplicity, this model will be referred to as the SWMF model. The SWMF model assumes 30% of the particle fluxes crossing the equatorial plane are scattered into the loss cone, where they precipitate into the ionosphere. Utilizing characteristic energy distributions found in the ring current region, an energy flux is obtained. The output of the model is the most equatorward location at which a specified energy flux value is obtained. Its longitudinal resolution is coarse, limited to one hour MLT spacing. At this time, plotting an entire polar grid is not possible with the model's output. A representative sample of a boundary provided by the SWMF model is shown in Figure 14. Generally speaking, the SWMF's boundary is highly symmetric about the magnetic pole and largely invariant to changes in K<sub>p</sub>. This impact of this invariance on the model's comparative performance will be discussed in greater detail in Chapter IV.

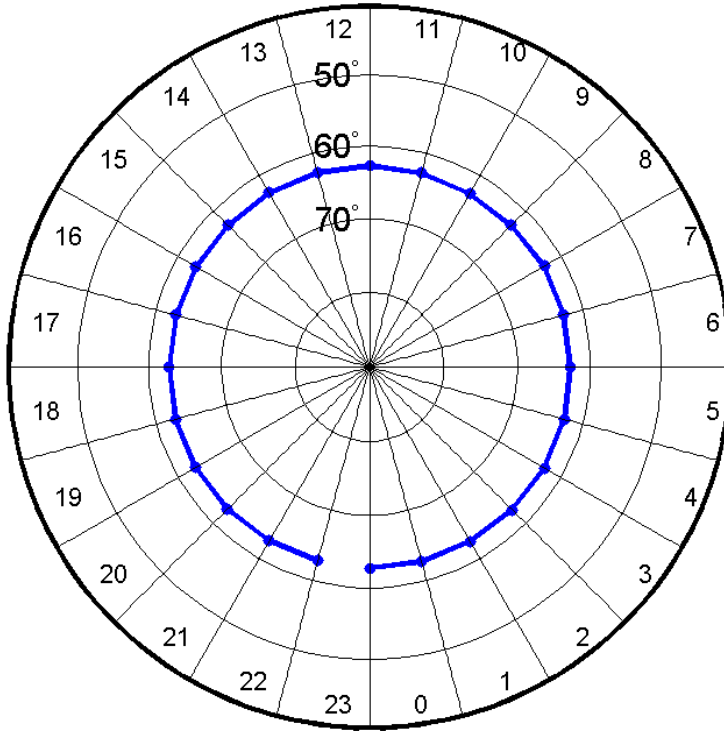


**Figure 14. SWMF characteristic boundary plot during Kp 3-. Boundary corresponds to an energy flux threshold of  $0.4 \text{ erg/cm}^2/\text{s}$ .**

#### 2.4.5 Assimilative Mapping of Ionospheric Electrodynamics

The Assimilative Mapping of Ionospheric Electrodynamics (AMIE) procedure is a specification model that was fielded in 1988. Its purpose is to synthesize collections of diverse data relating to the high-latitude ionospheric environment into patterns of conductivities, electric fields, and currents (Richmond et al., 1998). The AMIE model processes all data related to ionospheric conductances, including any observed data involving the energy fluxes of auroral particles, to obtain a conductance model. The conductance model can be used to estimate the energy flux of auroral particles throughout the polar regions. One of the capabilities for which AMIE was specifically designed pertains to auroral conductance and precipitation patterns.

As a specification model, AMIE procedure incorporates data from ground- and space-based instruments, including DMSP particle flux data. The model output is generated by performing an optimized, weighted least-squares fit of empirically measured parameters to existing statistical models. In effect, AMIE extrapolates as much information as possible from existing measurements and then utilizes fitting functions to fill in where data is absent (Richmond et al., 1998). The model's accuracy is inversely related to the amount of empirical data it is able to ingest, but the model can be used in a purely statistical sense, if there is no empirical data available.

This model will be referred to as the AMIE model. The data obtained for this study allowed for a model output with very good temporal resolution, but the data was limited to a spatial resolution of 1 hour MLT. Figure 15 depicts the result of an AMIE run for Kp 5 conditions. The reduction in spatial fidelity is readily apparent, and it becomes more problematic at more equatorward latitudes due to the expansion of the grid elements as a function of MLAT.

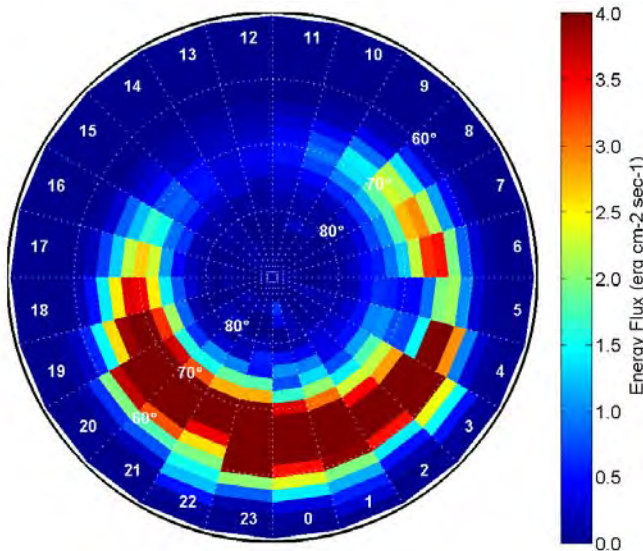


**Figure 15. AMIE polar plot for Kp 5 conditions. Its coarse resolution makes equatorward boundary identification difficult.**

### **III. Methodology**

This chapter describes the methods used to acquire and analyze the data utilized in this study. The first section pertains to the DMSP data and includes the means by which the data was obtained and processed. Then, the different methods used to calculate each model's equatorward boundary are detailed. Finally, the statistical measures that were used to establish meaningful comparisons between the models and the DMSP data are explained.

#### **3.1 DMSP Data**

DMSP data was obtained from an open-source website maintained by the Auroral Particles and Imagery Group at the Johns Hopkins University Applied Physics Laboratory (JHU/APL). A client-based JAVA application allowed the DMSP data to be retrieved and downloaded. Data was obtained from each satellite on a per day basis.

##### **3.1.1 DMSP Data Acquisition**

Table 3 is an extract from a data file containing one second of data of data recorded by DMSP Satellite F13 on May 15, 2005. The *UTC* column includes the date and time stamp of the data entry (seconds are not displayed). The *GLAT* (degrees) and *GLON* (degrees) columns convey the geographic latitude and longitude coordinates of the satellite in orbit. The *MLAT* (degrees) coordinate depicts the satellite's position using geomagnetic coordinates, and the *MLT* (hours) entry describes the longitudinal coordinate of the satellite's position. The MLT coordinate maintains a fixed reference to the sun, such that 12 MLT meridian is always sub-solar.

*JEE* and *JEI* entries represent the integral energy flux ( $\text{eV}/\text{cm}^2/\text{s}/\text{sr}$ ) for the electrons and ions respectively, and the *AvgEe* and *AvgEi* represent the average energy (eV) per electron and ion.

**Table 3. DMSP satellite data taken from Satellite F13 on May 15, 2005.**

| UTC            | GLAT  | GLON   | MLAT  | MLT   | JEE      | AvgEe    | JEI      | AvgEi    |
|----------------|-------|--------|-------|-------|----------|----------|----------|----------|
| 5/15/2005 0:01 | 81.37 | 225.90 | 82.22 | 11.28 | 3.54E+09 | 1.59E+02 | 1.86E+09 | 6.20E+03 |

Although the SSJ/4 sensor captures energy data in each of the 20 discrete channels, only the integral energy value was used in this study. Furthermore, this study made no distinction between electron and ion aurora with regard to the equatorward extent of the oval. The oval was determined based upon measurements of the total integral energy flux, calculated by adding the electron (*JEE*) and ion (*JEI*) energy fluxes together.

All of the events included in this study occurred between 2000-2008. The first dates selected for this study aligned with five prominent geomagnetic storms. This list included 13 total days, grouped into two-, three-, and four-day long events. The span of days for each event included the buildup and recovery phases of the storm. After data for these days was obtained, an additional 15 days were then added to include more low and moderate Kp index values and to represent a more diverse selection of months and years. A list of dates is included in Table 4.

Data was obtained from three satellites on each of the days in the study. The SSJ/5 sensor is installed on Satellite F17, but, as was mentioned previously, it provides the same integral energy flux data as the SSJ/4 sensor for the purposes of this study.

**Table 4. List of dates investigated.**

|                      | <b>Dates</b>        | <b>Days</b> | <b>DMSP Sat No.</b> |
|----------------------|---------------------|-------------|---------------------|
| Prominent<br>Storms  | 08/31/01 - 09/01/01 | 2           | 14, 15, 16          |
|                      | 05/15/05 - 05/16/05 | 2           | 13, 15, 16          |
|                      | 07/09/05 - 07/12/05 | 4           | 13, 15, 16          |
|                      | 08/31/05 - 09/01/05 | 2           | 13, 15, 16          |
|                      | 12/14/06 - 12/16/06 | 3           | 13, 15, 16          |
| Additional<br>Storms | 02/23/00 - 02/25/00 | 3           | 13, 14, 15          |
|                      | 10/23/02 - 10/25/02 | 3           | 13, 14, 15          |
|                      | 10/12/04 - 10/14/04 | 3           | 13, 15, 16          |
|                      | 06/19/07 - 06/21/07 | 3           | 13, 15, 17          |
|                      | 03/26/08 - 03/28/08 | 3           | 15, 16, 17          |

### 3.1.2 DMSP Data Compilation

The Matrix Laboratory (MATLAB) program was used to process all the DMSP data. Each of the DMSP data files was read into a specially developed MATLAB algorithm. This algorithm interrogated the energy flux data and automatically determined the MLAT-MLT coordinate of the equatorward boundary. Then, the location of the boundary was plotted on a geomagnetic polar grid.

Up to 14 orbits occurred during a 24 hour period; however, there were several conditions disqualified the orbit from the study. If the beginning of the data file corresponded to the satellite orbiting within the polar region, then that particular orbit was discarded. There were also multiple instances in the DMSP data files where no energy flux data recorded. These data points, identified by entries where the energy flux value was  $0.0 \text{ eV/cm}^2/\text{s/sr}$ , were deemed nonphysical and removed from the data file before processing it. If more than 10% of the entries in a data file recorded  $0.0 \text{ eV/cm}^2/\text{s/sr}$ , then the entire data file was deleted and another DMSP satellite was chosen.

Once the steps presented in the previous paragraph were used to condition the data file, a 15-second, moving average of the total energy flux was calculated. Using a moving average was an effective way to mitigate the impact of other spurious data points. Due to the satellites' trajectories, applying this average introduced approximately  $0.75^\circ$  of uncertainty in the MLAT coordinate but eliminated a large number of false crossing points.

In this study, the effective location of the equatorward boundary of the auroral oval was defined as the most equatorward MLAT where the average total integral energy flux exceeded  $0.4 \text{ erg/cm}^2/\text{s}$ . Another set of boundaries was determined using a  $0.6 \text{ erg/cm}^2/\text{s}$  threshold, and this data set was used to corroborate the results found at the lower flux threshold. As was discussed in Chapter II, no commonly accepted value can be said to perfectly represent the boundary. These quantities were selected because they were above the background readings of the detector but below the typical maximum readings observed inside the auroral oval. Because the DMSP satellites measure directional flux in units of  $\text{eV}/\text{cm}^2/\text{s}/\text{sr}$ , the energy fluxes were divided by  $\pi$  to obtain an equivalent value. Table 5 lists the unit conversions for each threshold.

**Table 5. Threshold Fluxes ( $\text{ener}/\text{cm}^2/\text{s}$ )**

| <b>erg</b> | <b>eV</b>            | <b>eV (per sr)</b>   |
|------------|----------------------|----------------------|
| 0.4        | $2.5 \times 10^{11}$ | $8.0 \times 10^{10}$ |
| 0.6        | $3.7 \times 10^{11}$ | $1.2 \times 10^{11}$ |
| 1          | $6.2 \times 10^{11}$ | $2.0 \times 10^{11}$ |

The plot in Figure 16 graphically depicts how the equatorward boundary of each orbit was determined. Each blue dot represents an energy flux measurement taken by the sensor. The heavy black line represents the 15-second moving average of the energy flux

measurements. The thin horizontal line is the energy flux threshold. The effective equatorward boundary occurs at the location where the heavy black line intersects the threshold. As was previously mentioned, each DMSP data file contained as many as 14 orbits. In a polar orbit, a northbound and a southbound crossing can be obtained, resulting in up to 28 total crossings per satellite per day.

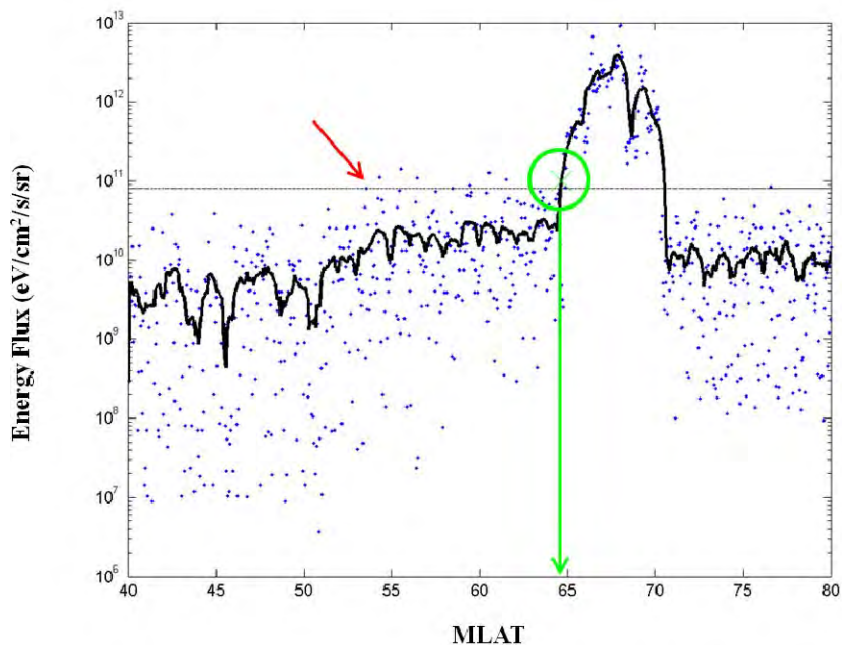


**Figure 16.** DMSP orbit plot taken from DMSP Satellite F15 on August 31, 2001 during low K<sub>p</sub> conditions. Energy flux threshold is  $8.0 \times 10^{10}$  eV/cm<sup>2</sup>/s/sr. Red arrow indicates false boundary if no smoothing function is used. The circled green X indicates the location of the effective boundary.

These plots were used to validate the location of the boundary coordinates. Despite using the smoothing function, occasionally a single, high-energy data point was able to foul the moving average. An example of this is shown in Figure 17. These occurrences were also deemed non-physical, and the boundary coordinate was excluded from the study. To ensure the highest standard of date integrity, a plot was created for

every boundary and was visually inspected for anomalies like the one shown in Figure 17.

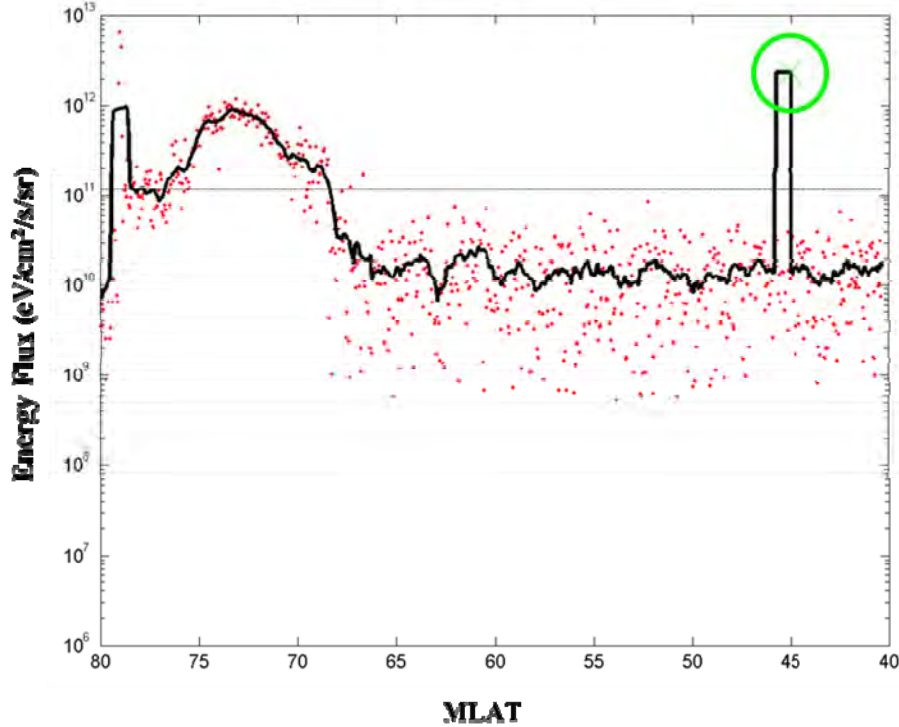


**Figure 17. Example of discarded orbit due to anomalous data.**

The UTC of each threshold crossing was recorded, and the crossings that occurred during the same hour were grouped together and plotted on a polar projection map like the one shown in Figure 18. The grid is divided into MLAT-MLT sectors. This allowed chronological crossing points to be plotted on the same map. As an example, Figure 18 shows the location of the six threshold crossings found between 0800-0900 UTC on May 15, 2005, during high K<sub>p</sub> conditions. These plots were originally generated to observe the qualitative systematic migration of the equatorward boundary, but they also identified the considerable variance in the boundary location defined by DMSP flux data.

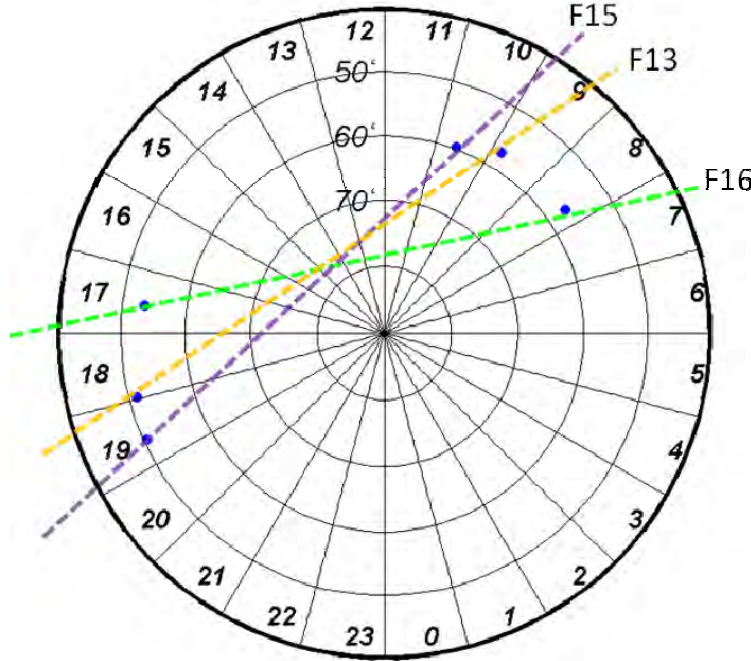


**Figure 18.** DMSP crossing points (blue dots) obtained between 08-09 UTC on May 15, 2005 during high K<sub>p</sub> period. Crossing points determined using a 0.4 erg/cm<sup>2</sup>/s energy flux threshold. Six data points were obtained during this 60 minute period from the F13, F15, and F16 satellites, whose trajectories are indicated by the dashed lines. Grid coordinates are MLAT-MLT.

When a threshold crossing occurred, the UTC, MLAT-MLT coordinates, and energy flux were captured from the DMSP data. Using the UTC, the corresponding K<sub>p</sub> index value was obtained from a separate database of three-hour K<sub>p</sub> index values.

After a day of satellite data was run, the results were compiled into a single data file for each day. Table 6 contains an example data file. This table lists each boundary obtained during a 24-hour period. There is a missing orbit (4N) near 6:00 UTC, whose data was excluded for one of the reasons previously discussed.

This data was used to initialize the model runs. The OP, SWMF, and AMIE models required the UTC, and the OH and NH models required the K<sub>p</sub> index value. Based on this input, each model determined a precipitation pattern, and this output was

interrogated to obtain the model's location of the effective equatorward boundary. The difference between the DMSP boundary location and model's boundary was the fundamental data obtained in this study. The process used to obtain each model's boundary will be explained in the next section.

**Table 6. DMSP Threshold Crossing Data obtained from DMSP Satellite F13 on December 14, 2006. Missing data indicates disqualified orbit.**

| Orbit | UTC   | MLAT  | MLT   | Kp  |
|-------|-------|-------|-------|-----|
| 1N    | 0:54  | 73.27 | 15.79 | 3.0 |
| 1S    | 1:05  | 67.79 | 8.32  | 3.0 |
| 2N    | 2:38  | 73.67 | 14.61 | 3.0 |
| 2S    | 2:47  | 67.34 | 8.69  | 3.0 |
| 3N    | 4:20  | 69.55 | 15.51 | 2.3 |
| 3S    | 4:30  | 66.44 | 8.91  | 2.3 |
| 4N    | --    | --    | --    | --  |
| 4S    | 6:11  | 68.62 | 9.60  | 2.0 |
| 5N    | 7:47  | 74.90 | 14.48 | 2.0 |
| 5S    | 7:53  | 70.20 | 10.02 | 2.0 |
| 6N    | 9:28  | 72.82 | 16.02 | 2.0 |
| 6S    | 9:37  | 68.23 | 9.47  | 2.0 |
| 7N    | 11:10 | 74.33 | 16.43 | 2.0 |
| 7S    | 11:20 | 68.83 | 8.99  | 2.0 |
| 8N    | 12:51 | 73.42 | 17.37 | 5.0 |
| 8S    | 13:03 | 67.09 | 7.93  | 5.0 |
| 9N    | 14:31 | 68.79 | 18.07 | 5.0 |
| 9S    | 14:45 | 63.82 | 7.05  | 5.0 |
| 10N   | 16:11 | 63.65 | 18.26 | 5.3 |
| 10S   | 16:26 | 64.27 | 6.58  | 5.3 |
| 11N   | 17:51 | 61.89 | 18.37 | 5.3 |
| 11S   | 18:07 | 62.37 | 6.52  | 5.3 |
| 12N   | 19:33 | 63.91 | 18.52 | 5.3 |
| 12S   | 19:47 | 63.39 | 6.81  | 5.3 |
| 13N   | 21:14 | 65.56 | 18.40 | 7.7 |
| 13S   | 21:28 | 64.54 | 7.25  | 7.7 |
| 14N   | 22:53 | 61.38 | 17.99 | 7.7 |
| 14S   | 23:10 | 62.86 | 7.57  | 7.7 |

## 3.2 Auroral Precipitation Models

### 3.2.1 The Original Hardy Model

As mentioned in Chapter II, the original, 1985 version of the Hardy model has been designated the Original Hardy (OH) model in this study. This model was obtained from Utah State University. The model's algorithm generated a data file of the energy flux values at each MLAT-MLT grid element (the model's resolution is  $0.10^\circ$  MLAT by 0.25 hour MLT). Because the OH model is parameterized by integral K<sub>p</sub> index value from 0 to 6, only seven data files were created.

The equatorward boundary of the OH model was determined by interrogating each MLT sector (4 sectors per hour) from low to high MLAT for the point where the flux threshold was first exceeded. Figure 19 shows the results for K<sub>p</sub> values of 1, 3, and 5 with the threshold set at  $0.4 \text{ erg/cm}^2/\text{s}$ . In some cases, particular near 12 MLT, no effective boundary was found using this threshold.

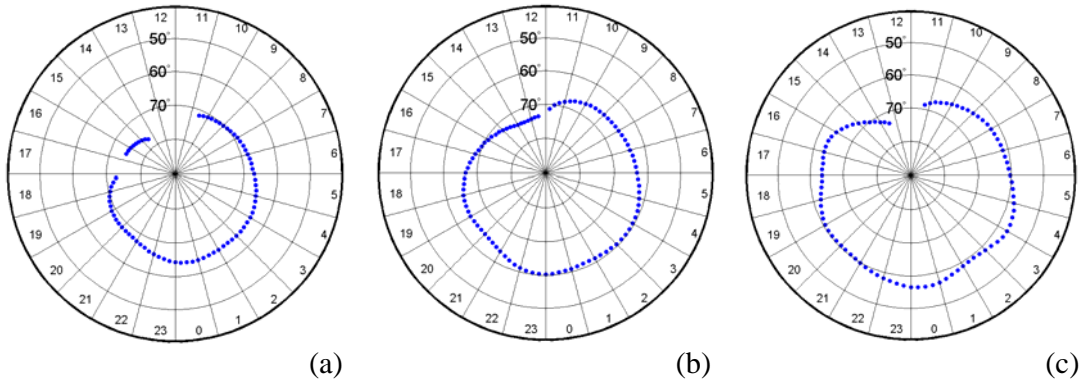


**Figure 19. OH equatorward boundaries for (a) Kp 1, (b) Kp 3, (c) Kp 5. Boundary corresponds to energy flux of  $0.4 \text{ erg/cm}^2/\text{s}$ . Absent data corresponds to MLT sector with no threshold crossing.**

Then, a data file was generated that compared the model boundary to each DMSP crossing point. To do this, each DMSP MLT coordinate was rounded to the nearest 0.25

hour MLT (e.g., 10.13 was rounded to 10.25 MLT). In the corresponding MLT wedge, the model's equatorward boundary recorded. The signed difference between the DMSP MLAT and the OH MLAT was also calculated. A positive difference indicated the DMSP boundary was found more toward the pole (at a higher MLAT) than the model boundary.

### 3.2.2 OVATION Prime Model

Like the DMSP data, the OP model was also accessed at the Auroral Particles and Imagery group maintained by JHU/APL. The model's output is a polar map very similar to OH, except it is not parameterized based upon a single input condition. To generate a plot, the OP model required the date and time of each DMSP crossing event.

The source data, provided by Dr. Patrick Newell, was used to construct an automatic program capable of running the model without using the web interface. The automated program took an input file consisting of dates at times and generated an output file for each crossing.

The output file consisted of the same information as the OH model contained; however, the OP's MLAT resolution was  $0.50^\circ$  versus  $0.10^\circ$ . Initially, the location of the boundary was determined in the same way as was for OH, but OP's unusual energy flux calculations at low latitude led to many false boundaries. Some of the pixels in the annulus between  $50\text{--}60^\circ$  MLAT were found to have very high energy flux values, which generated a false boundary location. To mitigate this problem, the boundary was defined only if three consecutive energy flux values in an MLT wedge were above the threshold. If this criterion was met, the boundary was logged at the first of the three MLAT coordinates. Imposing this requirement eliminated most of the false boundary triggers.

The data files were generated the same way they were with the OH model: each DMSP crossing MLT was rounded to the nearest 0.25 hour, and the MLAT of the model's equatorward boundary was recorded in the corresponding MLT wedge.

Additionally, to demonstrate the systematic characteristics of the oval, another MATLAB program was developed to create a boundary plot of the full oval. An example is shown in Figure 20. During the creation of these plots, more anomalies with the model's boundary were observed, in spite of the stricter criteria imposed. An example of this condition is shown in Figure 21.

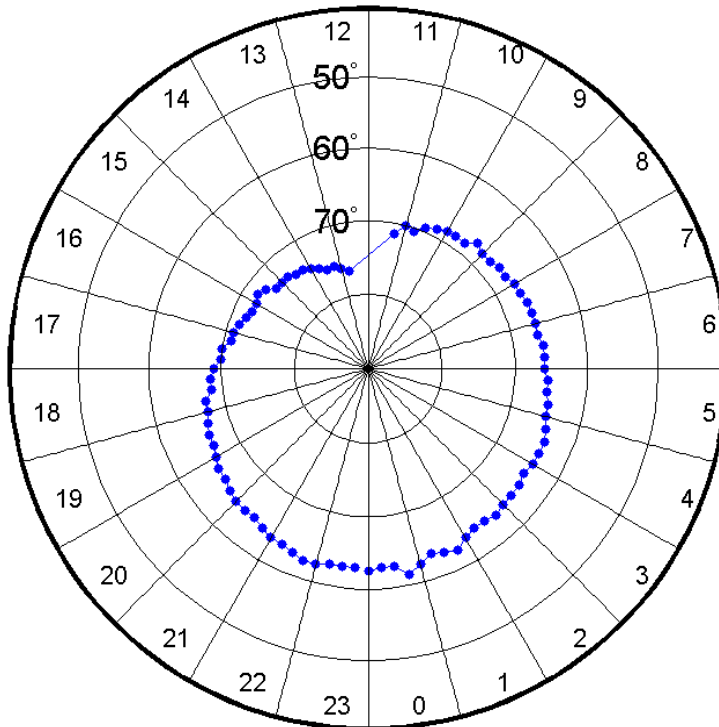


**Figure 20.** OP boundary plot generated for August 31, 2001 at 17:38 UTC during Kp 4 conditions. Boundary corresponds to energy flux of  $0.4 \text{ erg/cm}^2/\text{s}$ . Absent data between 1130-1230 MLT indicate sector in which no threshold crossing occurs.

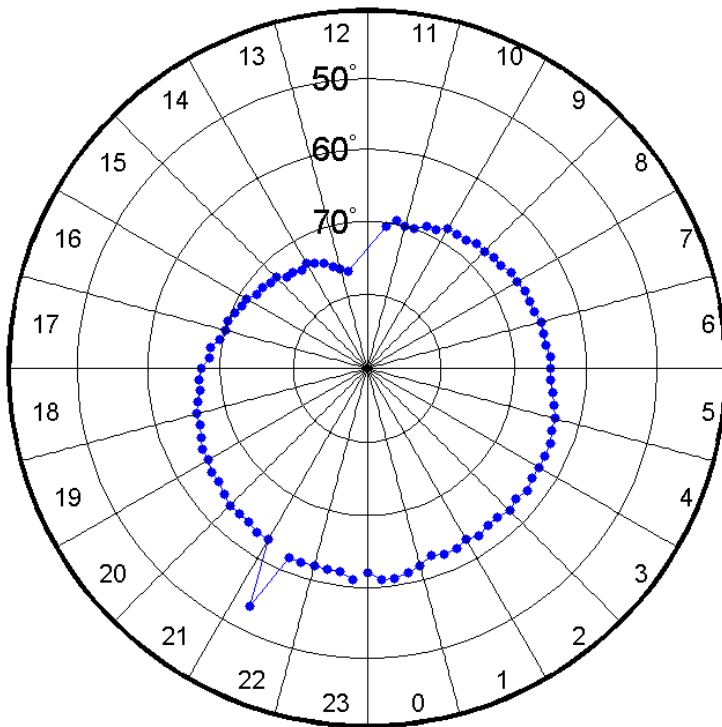


**Figure 21.** Example of spurious OP boundary point despite imposing stricter selection criteria. Plot generated for August 31, 2001 at 00:25 UTC during quiet conditions ( $K_p$  3-). Boundary in 2215 MLT sector is  $\sim 10^\circ$  displaced.

### 3.2.3 The New Hardy Model

The data files for the enhancements to the original Hardy model were provided by Dr. Chin Lin and colleagues at the AFRL. The processing of this data followed the same approach as the OH model did, and the format of the output and the model's resolution were identical. Figure 22 is the NH analog of Figure 19 and presents the model's boundary location at each  $K_p$  index values of 1, 3 and 5. If no data point exists, it means the model did not compute an energy flux value above the threshold in that MLT sector. With the NH model, this occurred routinely between approximately 12-16 MLT.

For each DMSP crossing point, the MLT was rounded to the nearest 0.25 hour, and the MLAT corresponding to the most equatorward occurrence of an energy flux at or

above the threshold was recorded into a data file. The difference between the two coordinates was also determined and recorded.

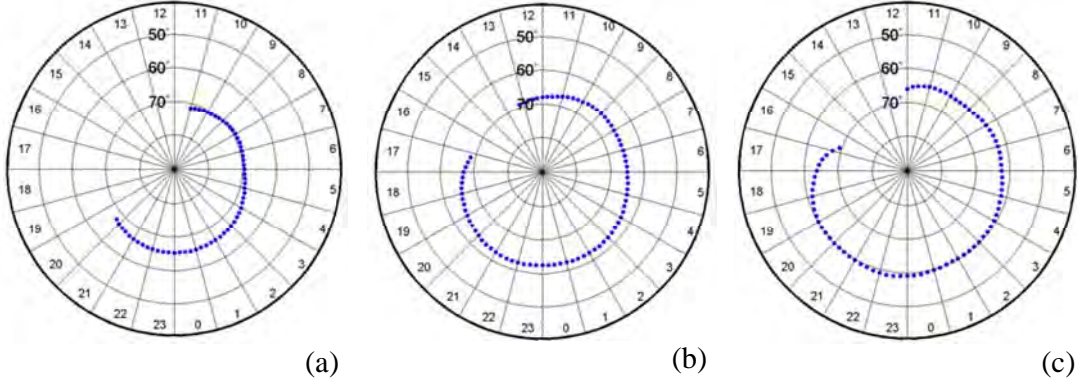


**Figure 22. NH equatorward boundaries for (a) Kp 1, (b) Kp 3, (c) Kp 5. Boundary corresponds to energy flux of  $0.4 \text{ erg/cm}^2/\text{s}$ . Absent data corresponds to MLT sector with no threshold crossing.**

### 3.2.4 Space Weather Modeling Framework Model

For this model, researchers at NASA CCMC provided a file with boundary coordinates only, precluding the depiction of a synoptic, polar plot. Three independent boundary files, however, were provided for each of the three energy flux thresholds used in this study.

One file was available for each day, and each hour was divided into 15 individual entries spaced between 3 and 4 minutes apart. Each entry contained 1 MLAT coordinate in each of the 24 MLT sectors. To interrogate this data, a slightly different MATLAB algorithm was developed. First, for each DMSP crossing time (UTC), the closest SWMF data entry was found. Then, the DMSP MLT coordinate was rounded to the nearest whole hour, and the model's corresponding boundary MLAT was recorded into a file. The difference between the DMSP and model's coordinates was calculated as it was for the previous models. To demonstrate the difference in resolution, two examples of the

SWMF boundary plot are shown in Figure 23. These plots were generated with data obtained on August 31, 2005 during low and high K<sub>p</sub> conditions. Only one point describes the boundary in each MLT wedge. This model exhibits minimal expansion in response to geomagnetic storming and a high degree of symmetry around the geomagnetic pole.

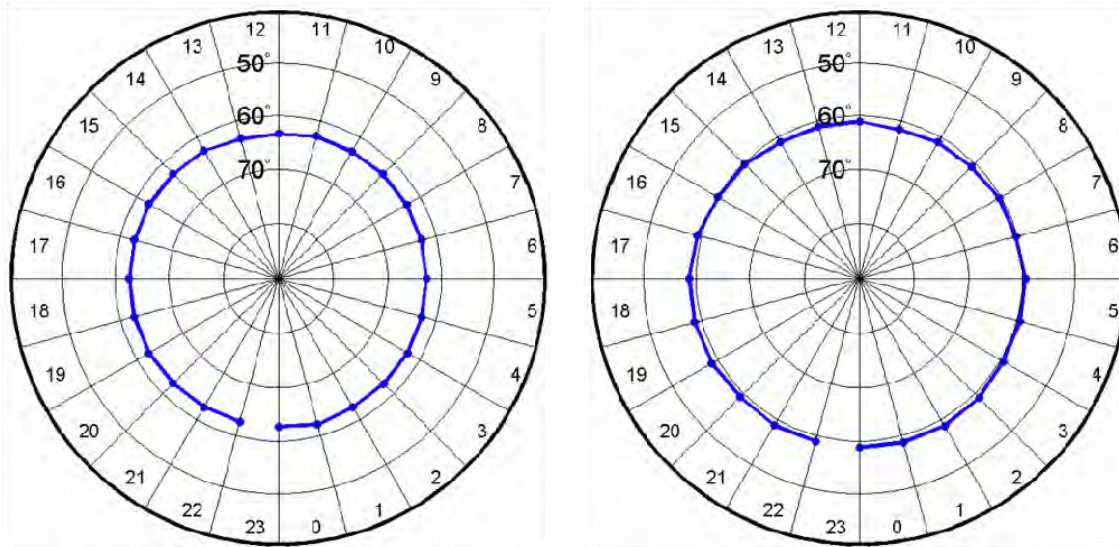


**Figure 23.** SWMF boundary plots generated on August 31, 2005 for K<sub>p</sub> 3- (left) and K<sub>p</sub> 7- (right) conditions. Boundary locations correspond to an energy flux of 0.4 erg/cm<sup>2</sup>/s. Minimal expansion is observed and a high degree of symmetry around the geomagnetic pole is observed with this model.

### 3.2.5 Assimilative Mapping of Ionospheric Electrodynamics Model

Like the NH and SWMF data, AMIE data was obtained from an external agency. Indebtedness is due to Dr. Aaron Ridley at the University of Michigan for providing the data files containing energy flux information.

As was the case with the SWMF model, AMIE's resolution is also 1 hour MLT by 0.50° MLAT. As before, a MATLAB program rounded the DMSP crossing coordinates to the nearest MLT and then found and recorded the MLAT corresponding to the model's equatorward boundary. The difference between the two were again

calculated and recorded. In order to enable a graphical comparison to the other models, another program was developed to plot the AMIE equatorward boundary on a polar projection. An example of the resulting plot, using a  $0.4 \text{ erg/cm}^2/\text{s}$  threshold, is shown in Figure 24.

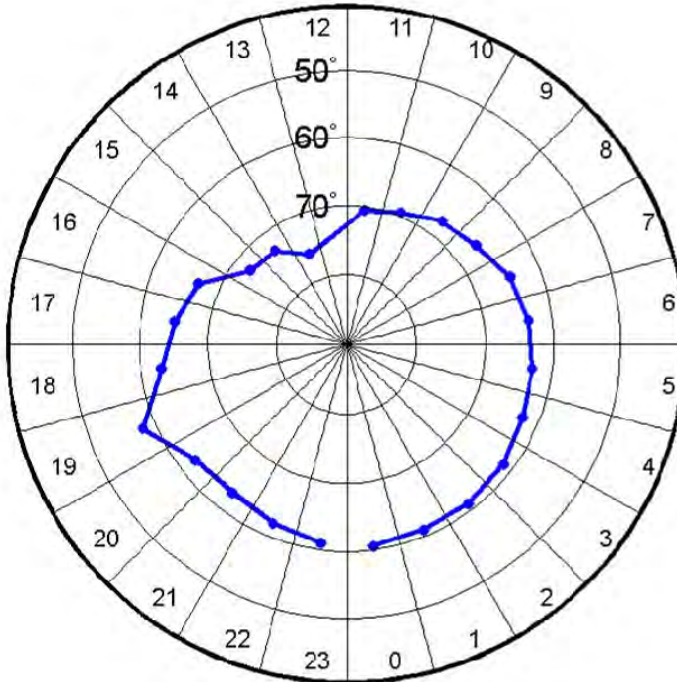


**Figure 24.** AMIE boundary plot generated for May 15, 2005 during  $\text{Kp } 6-$  conditions. Boundary locations correspond to an energy flux of  $0.4 \text{ erg/cm}^2/\text{s}$ .

### 3.3 Data Compilation

Unfortunately, some data availability limitations precluded comparing all of the DMSP data to all of the models. None of the additional days selected for the study (Table 4) could be processed with the SWMF or AMIE models. Availability of SWMF data, even for the high  $\text{Kp}$  events, was further limited. Thus, the number of events processed in this statistical comparisons of SWMF and AMIE was significantly less than the total number of DMSP data points.

Regarding the OH and OP models, many low-K<sub>p</sub> events were also unable to be processed. As was discussed previously, this occurred because in some MLT sectors (particularly near 1200 MLT), these models did not compute an energy flux above the threshold. This problem was exacerbated at higher energy flux thresholds. Originally, an additional flux threshold of 1.0 erg/cm<sup>2</sup>/s was also intended to be used in this study. However, the losses associated with this threshold were deemed too substantial, and all of this data was discarded. Table 7 presents the total number of data points used in the analysis of each model.

**Table 7. Number of crossings for each model for each energy flux threshold.**

|             | Thresholds |            |            | <b>Total</b> |
|-------------|------------|------------|------------|--------------|
|             | <b>0.4</b> | <b>0.6</b> | <b>1.0</b> |              |
| <b>DMSP</b> | 2198       | 2154       | 1945       | 6297         |
| <b>NH</b>   | 1798       | 1518       | 1007       | 4323         |
| <b>OH</b>   | 2059       | 1724       | 1227       | 5010         |
| <b>OP</b>   | 2122       | 1722       | 1130       | 4974         |
| <b>SWMF</b> | 426        | 320        | 317        | 1063         |
| <b>AMIE</b> | 849        | 764        | 610        | 2223         |

The data points obtained using each specific threshold were not combined, yielding, in effect, three sub-studies. At a specific threshold, all of the data was compiled into one file. This file included the UTC, the K<sub>p</sub>, the MLT, and the DMSP and respective model's MLATs. The signed difference between the DMSP and each model was also included in this file.

This file was used to then create histogram plots to convey the MLT distribution and K<sub>p</sub> distribution of the data points. The number of data points lost due to the model failing to produce a threshold crossing was also plotted as a function of MLT and K<sub>p</sub>.

In order to afford the most flexibility to the study, a scheme was devised to parse the data into the seasons, time-of-day (TOD), and Kp groupings. Table 8 lists the definitions of the subdivisions in each category.

**Table 8. Definitions of data subcategories.**

| Season        |           | TOD (MLT)    |         | KP          |           |
|---------------|-----------|--------------|---------|-------------|-----------|
| <b>Winter</b> | Jan - Mar | <b>Dawn</b>  | 04 - 09 | <b>Low</b>  | 0.0 - 2.7 |
| <b>Spring</b> | Apr - Jun | <b>Day</b>   | 10 - 15 | <b>Mid</b>  | 3.0 - 6.0 |
| <b>Summer</b> | Jul - Sep | <b>Dusk</b>  | 16 - 21 | <b>High</b> | 6.3 - 9.0 |
| <b>Fall</b>   | Oct - Dec | <b>Night</b> | 22 - 03 |             |           |

### 3.4 Statistical Measures

Several statistical measures were deemed suitable for this study. The first calculation simply involved determining the mean ( $\mu$ ) and standard deviation ( $\sigma$ ) of the DMSP data points as a function of Kp. This was used to validate the statistical qualities of the DMSP data.

Several statistics were used to analyze the accuracy of the models. For each of the models, the statistical measures were calculated for all of the available data and for various combinations of the subcategories listed in Table 8.

The differences between the DMSP and each model's boundary location were used to find the mean value of the differences. The standard deviation ( $\sigma$ ) of the mean of these differences was also computed. Then, the following formula was used to calculate the standard deviation of the differences:

$$\sigma = \left\{ \frac{1}{N} \sum_{i=1}^N (y_i - \bar{x}_i)^2 \right\}^{1/2} \quad (5)$$

where  $y$  is the DMSP MLAT and  $x$  is the model's MLAT. The standard deviation categorizes the spread of the distribution of differences and is a convenient measure because it has units of MLAT and is always positive, regardless of whether the model's threshold is more equatorward or more poleward.

The next statistical measure that was calculated was the ratio estimate ( $RE$ ). It is given by

$$RE = \bar{y}/\bar{x} \quad (6)$$

where the bar operator designates the mean values. The  $RE$  is a measure of how closely the model varies at 1:1 ratio with measured observations. In this study, model accuracy is partially related to how much the model's equatorward boundary moves in relation to changes in the DMSP observation. If the model and physical observations are in perfect agreement, then  $RE = 1$ . Any deviations from this value indicate the model's calculated boundary is varying, in an average sense, more or less than the DMSP observed boundary.

One of the most prolifically used statistical measures in a comparative study of this sort is prediction efficiency ( $PE$ ). Prediction efficiency is a numerical score with a maximum value of 1 and no theoretical minimum value. It describes the percentage of the observed variance (e.g., DMSP data) explained by the model. When the  $PE = 0$ , this indicates that the model's calculations are statistically less accurate than using the observed mean. Thus, negative values of  $PE$  are not associated with any discernible characteristic other than that just described. The prediction efficiency was calculated for all of the data obtained in this study using this formula:

$$PE = 1 - \frac{\sum_{i=1}^N (y_i - x_i)^2}{\sum_{i=1}^N (y_i - \bar{y}_i)^2} \quad (7)$$

Another statistic of was used in this study is known as the skill score (*SS*). The skill score compares a model's performance against the performance of a reference model. It determines if the test model provides a more accurate representation of the observed conditions than does the reference. Statistically, the *SS* simply represents the ratio of the square error of two models. A perfect skill score is 1, and it also has no negative bounds. It is found by calculating the following:

$$SS = 1 - \frac{\sum_{i=1}^N (y_i - x_{test_i})^2}{\sum_{i=1}^N (y_i - x_{ref_i})^2} \quad (8)$$

A skill score greater than 0 means the tested model outperformed the reference model (in effect, having less aggregate error). In this study, the OH model was selected to be the reference model because of its long-standing reputation and successful implementation in various capacities. A *SS* was then calculated for the NH and OP models.

## **IV. Results and Analysis**

In this chapter, the results and analysis of the study will be presented. The statistical characteristics of the DMSP satellite data will be discussed first. The subsequent section will reveal the statistical measures of the models' independent performances. Then, the prediction efficiency and skill score comparisons will be developed. These scores will be determined based upon the data obtained using the 0.4 erg/cm<sup>2</sup>/s energy flux threshold and will be corroborated with the 0.6 erg/cm<sup>2</sup>/s dataset. After the prediction efficiency rank order has been established, the next section will present an alternative means to compare the models' performances. Finally, the results of a small-scale, special investigation of particular auroral precipitation patterns will be presented.

As was mentioned in the previous chapter, the significant data losses associated with the 1.0 erg/cm<sup>2</sup>/s threshold precluded using this data in any statistical analysis. However, for completeness the DMSP statistics associated with the data obtained at this threshold will be included in the discussion. There will also be a small discussion on why using threshold resulted in such significant data losses.

### **4.1 DMSP Data Characteristics**

Data from 6,297 DMSP satellite passes were obtained in this study. This represents a sizeable sample set but is a small fraction of the total available DMSP data. The results discussed in this section will attend to the statistical characteristics of the sample of DMSP data. The majority of the discussion in this chapter will focus on data obtained using a threshold flux of 0.4 erg/cm<sup>2</sup>/s. Unless annotated specifically, there are

no distinct or consequential differences to any conclusions in this chapter with regard to the independent study conducted with the 0.6 erg/cm<sup>2</sup>/s threshold.

#### 4.1.1 DMSP Systematics

Figure 25 contains the polar plots of the DMSP threshold crossings obtained as a function of Kp index. Equatorward expansion of the oval with increasing Kp value can be easily inferred from the plots. However, as was indicated in Figure 18, the substantial variance originally seen in the data has persisted.

The statistics of the data are summarized in Table 9, which shows the mean value (MLAT) of the threshold crossing points ( $\mu$ ) and the standard deviation ( $\sigma$ ) for each Kp index value. Simple inspection of this data shows a decrease in the average MLAT of the effective boundary location as Kp index increases. This trend is consistent with the theoretical expectation discussed in Chapter II.

**Table 9. Statistics of DMSP satellite coordinates corresponding to threshold crossings. Average crossing MLAT is displayed for each Kp index value.**

| Threshold = 0.4 erg/cm <sup>2</sup> /sec (Total Events: 2198) |       |       |       |       |       |       |       |       |       |   |
|---|-------|-------|-------|-------|-------|-------|-------|-------|-------|---|
| Kp  | 0     | 1     | 2     | 3     | 4     | 5     | 6     | 7     | 8     | 9 |
| N   | 21    | 235   | 381   | 404   | 562   | 307   | 184   | 41    | 63    | 0 |
| $\mu$   | 74.25 | 71.94 | 68.53 | 66.94 | 65.62 | 63.74 | 62.50 | 58.94 | 58.60 | 0 |
| $\sigma$  | 2.37  | 3.49  | 3.86  | 3.55  | 3.47  | 3.52  | 4.04  | 1.96  | 3.35  | 0 |

| Threshold = 0.6 erg/cm <sup>2</sup> /sec (Total Events: 2154) |       |       |       |       |       |       |       |       |       |   |
|---|-------|-------|-------|-------|-------|-------|-------|-------|-------|---|
| Kp  | 0     | 1     | 2     | 3     | 4     | 5     | 6     | 7     | 8     | 9 |
| N   | 16    | 206   | 366   | 401   | 572   | 306   | 186   | 38    | 63    | 0 |
| $\mu$   | 75.37 | 72.65 | 69.26 | 67.75 | 66.39 | 64.36 | 63.00 | 59.33 | 59.22 | 0 |
| $\sigma$  | 2.55  | 3.62  | 4.11  | 3.78  | 3.93  | 3.60  | 4.04  | 2.11  | 3.68  | 0 |

| Threshold = 1.0 erg/cm <sup>2</sup> /sec (Total Events: 1945) |       |       |       |       |       |       |       |       |       |   |
|---|-------|-------|-------|-------|-------|-------|-------|-------|-------|---|
| Kp  | 0     | 1     | 2     | 3     | 4     | 5     | 6     | 7     | 8     | 9 |
| N   | 12    | 164   | 322   | 382   | 531   | 252   | 181   | 77    | 24    | 0 |
| $\mu$   | 77.65 | 73.63 | 69.77 | 68.50 | 67.57 | 65.37 | 63.81 | 61.17 | 56.96 | 0 |
| $\sigma$  | 2.38  | 3.70  | 4.29  | 3.89  | 4.06  | 4.04  | 4.37  | 3.35  | 2.69  | 0 |

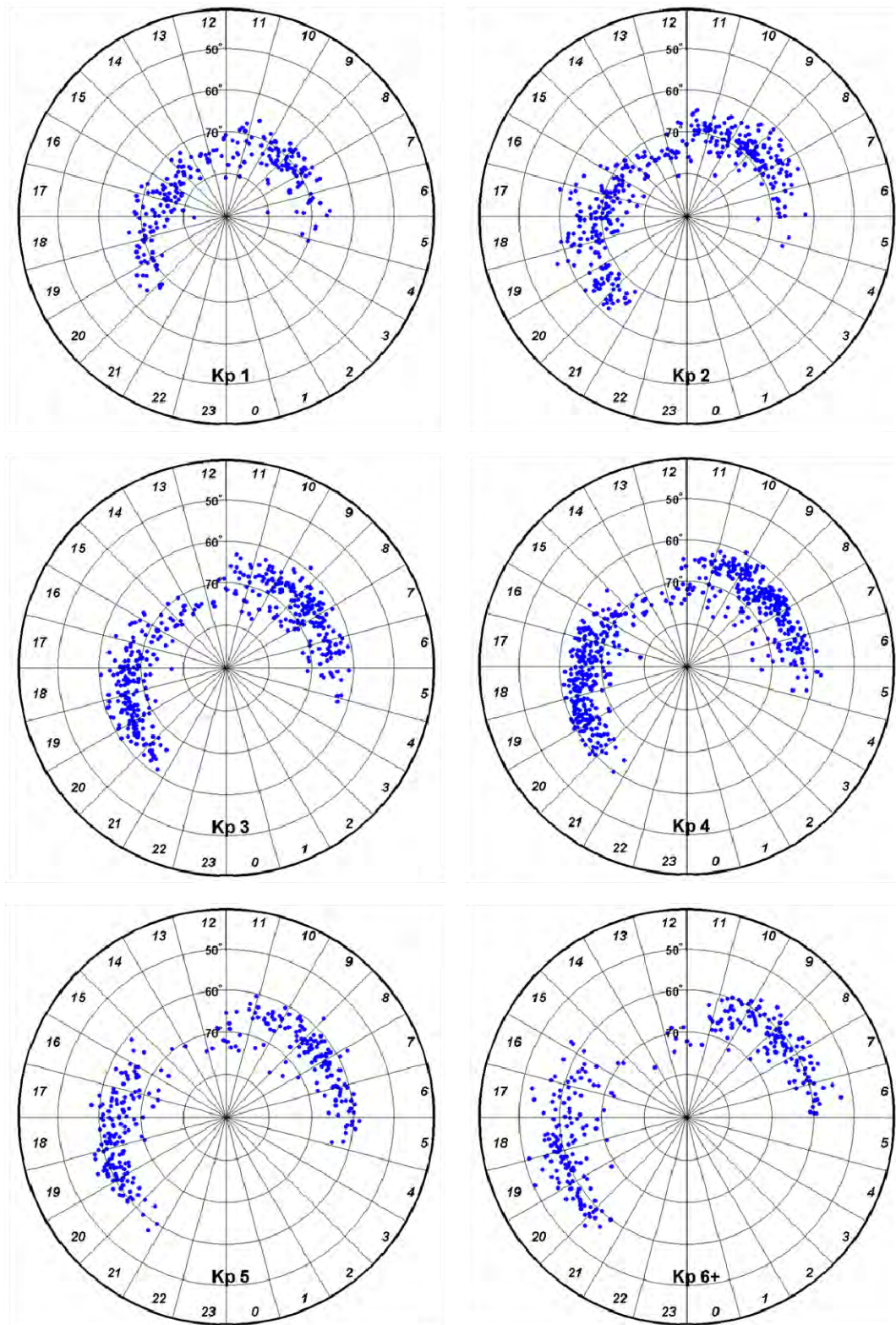


**Figure 25.** DMSP boundary locations using a  $0.4 \text{ erg/cm}^2/\text{s}$  energy flux threshold grouped by Kp index. Systematic expansion equatorward is observed with increasing Kp index, however, significant variance exists in the boundary's locations.

At the lowest energy flux threshold, the standard deviations range between 1.96 and 4.04 degrees. The standard deviation does not decrease in Kp bins where the most data was obtained. Furthermore, it does not uniformly increase or decrease as a function of Kp index value. In effect, there is systemic, pervasive scatter in the DMSP data. These are qualities of the DMSP data that cannot be improved upon.

Further reference to Table 9 shows the data obtained using the 0.6 and 1.0 erg/cm<sup>2</sup>/s thresholds exhibit an increase in standard deviation at almost all Kp levels. This indicates a worsening quality of the data; however, the mean crossing values are more poleward than those at the lower threshold. This is also theoretically consistent. Thus, although the data obtained using the lowest energy threshold has a sizeable variance, it remains the most suitable for comparison to the models, and the data obtained using the larger threshold is suitable to support and corroborate any conclusions drawn.

Other characteristics of the DMSP data limit this study. Most notably, there is a non-uniform distribution of data points with regard to MLT. This is the result of the sun-synchronous orbits of the DMSP satellites. The naturally infrequent occurrence of events with high Kp index values also limits the available data. The charts presented in Figure 26 show that there are significantly fewer crossing points obtained with a Kp index was greater than 6, and, regarding MLT, there exists a dearth of data between 11-15 MLT and no data between 22-03 MLT. The only way to mitigate either of these limitations is to increase the original number of data points by introducing data from earlier decades. However, for the purposes of this study, the amount of data collected remains sufficient to draw valid and substantiated conclusions.

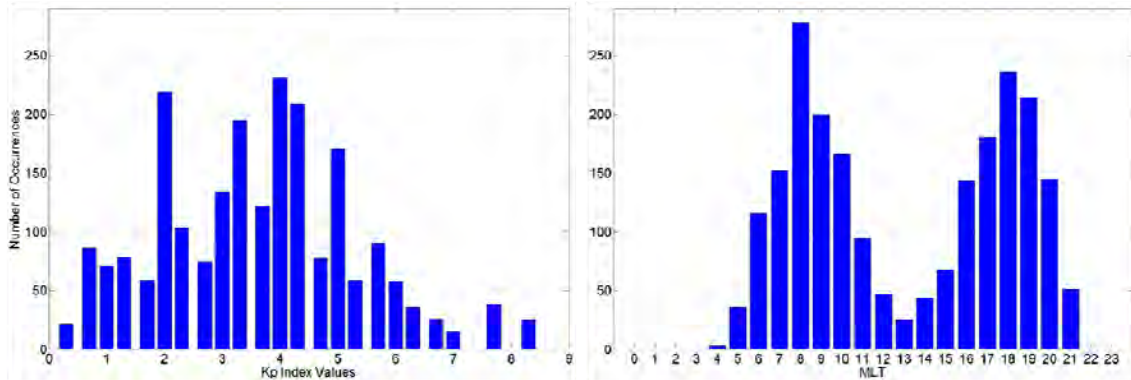


**Figure 26. DMSP data distributions for 0.4 erg/cm<sup>2</sup>/s dataset. Data is limited at Kp index values greater than 7 and between 11-15 MLT. No data obtained between 22-03 MLT.**

It was not apparent that other studies performed equivalently calculated standard deviations, like the values shown in Table 9. Thus, it was not possible to compare the DMSP data obtained in this study directly to that obtained in other research efforts. However, because the DMSP data is of central to the validity of the study, additional investigation was performed in the form of a basic regression analysis. This type of analysis was performed in previous research by Hardy and Gussenhoven and will assist in validating the characteristics of the DMSP data in this study.

#### 4.1.2 Regression Analysis

Past research studies (Gussenhoven et al., 1983, Hardy et al., 2008) have characterized the equatorward boundaries ( $\Lambda$ ) obtained from DMSP data by conducting a regression analysis of the form  $\Lambda = \Lambda_o + \alpha \cdot Kp$ . The slopes of the lines ( $\alpha$ ) can be compared against each other to show sensitivity to Kp, and the correlation coefficients ( $r^2$ ) are helpful in determining the linearity of the data. Data with less scatter will have a higher correlation coefficient. The results of regression analysis for the DMSP data in this study are contained in Table 10.

**Table 10. Regression analysis of the form  $\Lambda = \Lambda_o + \alpha \cdot Kp$ . Greyed areas represent MLT sector where no data was obtained. Lowest (worst) correlation occurs in the day sector.**

|      | MLT | N   | Intercept ( $\Lambda_o$ ) | Slope ( $\alpha$ ) | $ r^2 $ |
|------|-----|-----|---------------------------|--------------------|---------|
| 1    | --  | --  | --                        | --                 | --      |
|      | --  | --  | --                        | --                 | --      |
|      | --  | --  | --                        | --                 | --      |
| Dawn | 4   | 3   | 71.75                     | -2.81              | 1.00    |
|      | 5   | 36  | 72.13                     | -2.27              | 0.74    |
|      | 6   | 116 | 71.69                     | -1.88              | 0.76    |
|      | 7   | 152 | 70.91                     | -1.56              | 0.72    |
|      | 8   | 278 | 71.33                     | -1.51              | 0.70    |
|      | 9   | 200 | 72.06                     | -1.65              | 0.69    |
|      | 10  | 166 | 72.96                     | -1.59              | 0.63    |
|      | 11  | 94  | 71.09                     | -0.67              | 0.25    |
|      | 12  | 47  | 75.27                     | -0.98              | 0.46    |
| Day  | 13  | 25  | 76.78                     | -0.91              | 0.70    |
|      | 14  | 44  | 75.66                     | -0.85              | 0.50    |
|      | 15  | 68  | 77.06                     | -2.00              | 0.72    |
|      | 16  | 143 | 76.27                     | -2.04              | 0.76    |
|      | 17  | 180 | 74.67                     | -2.09              | 0.72    |
|      | 18  | 236 | 72.60                     | -1.88              | 0.71    |
| Dusk | 19  | 214 | 70.51                     | -1.71              | 0.75    |
|      | 20  | 145 | 69.45                     | -1.69              | 0.76    |
|      | 21  | 51  | 68.84                     | -1.75              | 0.82    |
|      | 22  | --  | --                        | --                 | --      |
|      | 23  | --  | --                        | --                 | --      |
|      | 24  | --  | --                        | --                 | --      |

A couple of salient features emerge as part of the regression analysis. The intercepts between 12-17 MLT occur at higher latitudes, which is consistent with compression of the magnetopause on the dayside and its associated magnetic field lines. Despite the smaller sample sizes, the lower correlation coefficients found between 11-14 MLT (excluding 13 MLT) is also consistent with the fact the identification of the dayside boundary is beset with ambiguities, often attributed to contamination of ring current particles and influences from the cusp (Gussenhoven et al., 1981). There is no

theoretical explanation for the increase in correlation at 13 MLT, and this score is likely a statistical anomaly. In general, the increased unpredictability of the in situ measurements inferred by the data in this table was also observed in Hardy's and Gussenoven's previous research and is supported theoretically.

The reduced slopes ( $\alpha$ ) between 11-14 MLT indicate a decreased sensitivity to magnetic activity that has also been corroborated by other studies of this sort. Hardy et al. (2008) observed a similar clustering of the boundaries in the noon and mid-afternoon MLT sector at Kp index values of 1, 3, and 5. Past studies have also confirmed the existence of a steeper gradient in the evening and dawn sectors than in the pre- and post-noon sectors (Gussenoven et al., 1981). As a result, the evening boundary is typically less ambiguous to determine. Statistically, this is reflected in the higher correlation coefficients found outside the 11-14 MLT sector.

With regard to these morphological qualities, the data obtained in this study closely aligns with these patterns, which is clearly demonstrated by looking at two narrow MLT sectors from opposite regions. Figure 27 depicts two plots of DMSP crossing data that were generated with data occurring at 11 and 20 MLT. In the morning sector, the equatorward crossings are found at more poleward locations than they are at 20 MLT. This is consistent with diurnal characteristics of the auroral oval discussed in Chapter II. Furthermore, the correlation coefficient is smaller here, indicative of increased uncertainty in the equatorward boundary's position in the pre- and post-noon sectors, as Gussenoven et al. (1981) alluded to. Finally, the slope of the regression line shows an increased sensitivity to Kp in the 20 MLT sector than in the 11 MLT sector, also consistent with the greater expansion observed on the evening side of the oval.

These plots also clearly show the lack of data for high-K<sub>p</sub> index conditions. This data shortage occurs throughout the entire dataset, regardless of sector, and precludes parsing the DMSP data into individual MLT sectors.

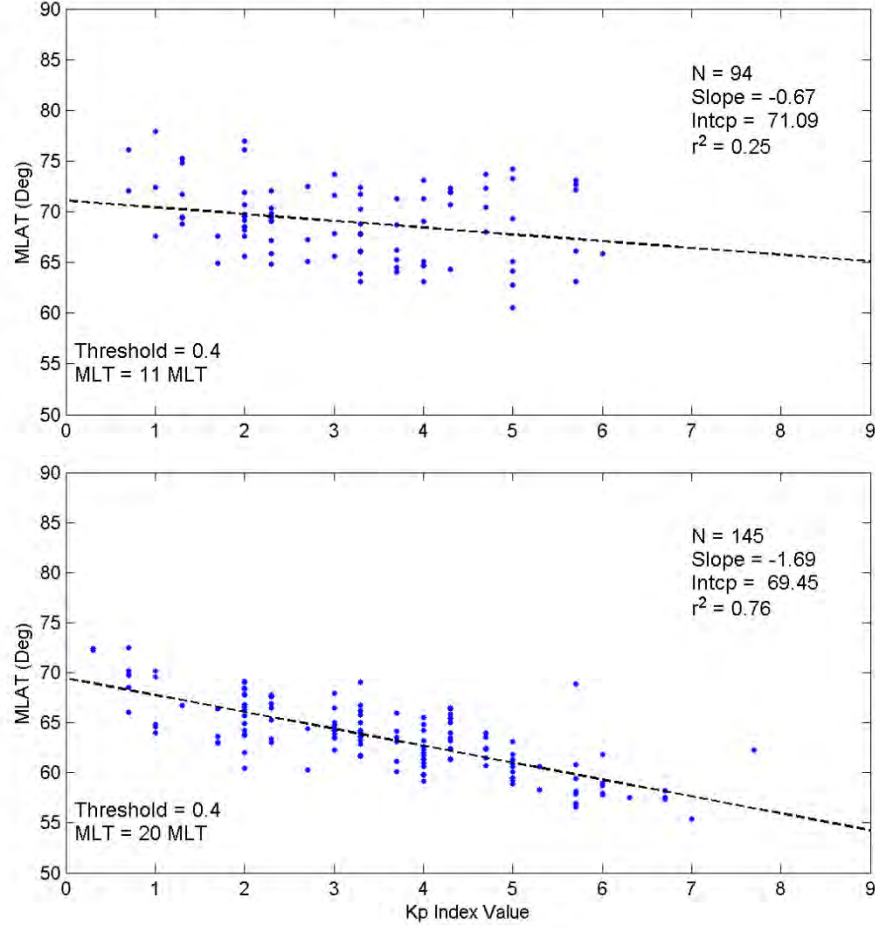


**Figure 27.** Scatterplots of DMSP threshold crossing coordinates at (a) 11 and (b) 20 MLT. In the morning sector, boundary is displaced poleward, is less dependent upon K<sub>p</sub>, and is more scattered.

#### 4.1.3 Data Binning

Table 11 depicts the results of a regression analysis when this study's data is grouped into three 6-hour MLT sectors and one 18-hour sector that encompasses all the data. The corresponding data plots are shown in Figure 28. When compiled in this manner, the data best reflects the results found in Hardy et al. (2008) and Gussenoven et

al. (1983), while maintaining the characteristics discussed in the previous paragraphs. Importantly, utilizing larger MLT sectors also allows high-K<sub>p</sub> data points to be grouped together in order to promote a better statistical investigation.

**Table 11. Same as Table 10 but with MLT groupings.**

| MLT   | N    | Intercept ( $\Lambda_0$ ) | Slope ( $\alpha$ ) | $ r^2 $ |
|-------|------|---------------------------|--------------------|---------|
| 04-09 | 785  | 71.50                     | -1.64              | 0.70    |
| 10-15 | 444  | 75.13                     | -1.69              | 0.59    |
| 16-21 | 969  | 72.60                     | -1.94              | 0.69    |
| 04-21 | 2198 | 72.96                     | -1.85              | 0.66    |

Cursory inspection of each panel of Figure 28 reveals that, even when grouped, the data still spans a broad range of MLATs at each integral K<sub>p</sub> value. In some cases, individual threshold crossings at the same K<sub>p</sub> index span more than 15° MLAT. These plots represent the inherent span present in the DMSP data that was accepted for the calculations performed in this study. Additionally, although the data is still scant at the high-K<sub>p</sub> indexes, these groupings have populated this region to the best extent possible.

#### 4.1.4 Data Losses

Because of the sun-synchronous orbits of the DMSP satellites, the number of crossings obtained between 11-13 MLT was significantly less than in other time frames. However, an additional problem attends auroral precipitation measurement in and near the 12 MLT sector. Paschmann (2003) observed there is a far greater likelihood of measuring a flux above 0.25 erg/cm<sup>2</sup>/s between 13.5 and 23 MLT. Hardy (2008) further purported that lower rates of pitch angle scattering in the dayside plasma sheet severely restrict electron precipitation in the region centered on 12 MLT.

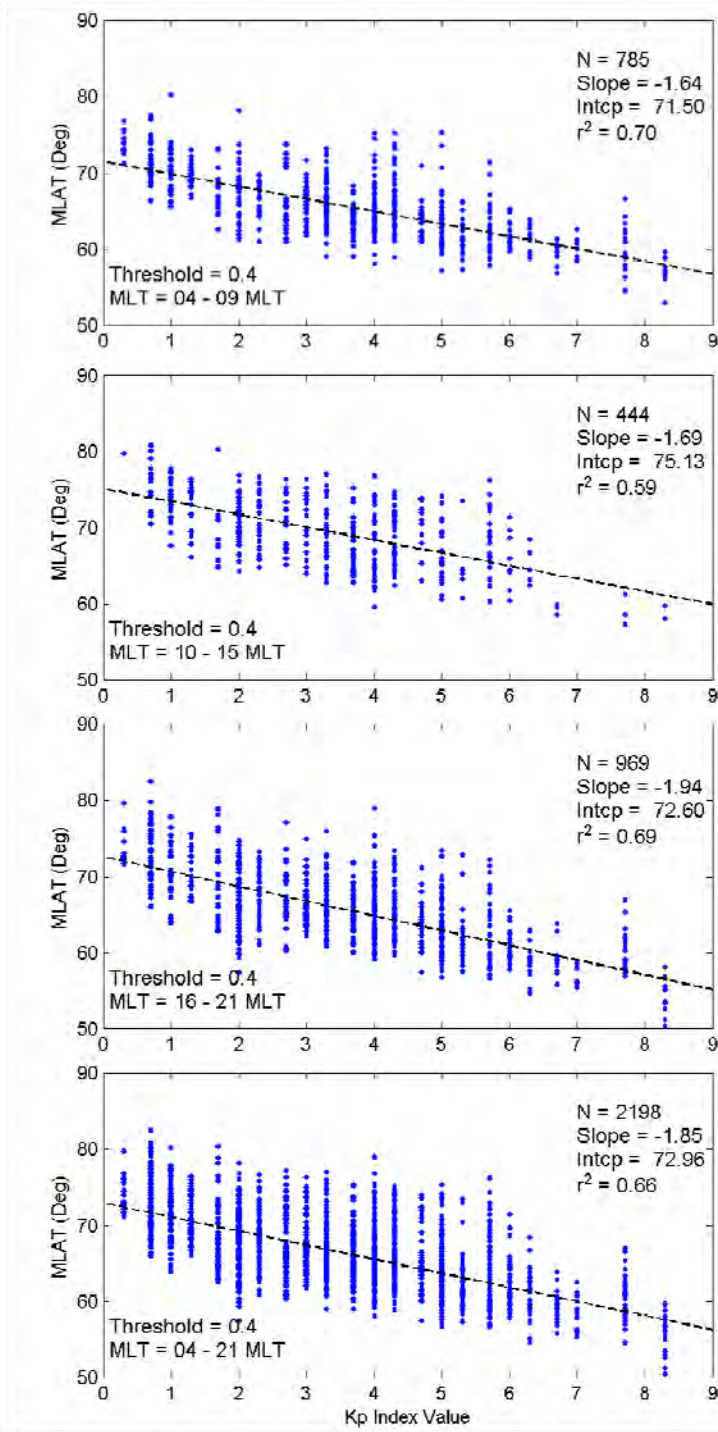


**Figure 28. DMSP boundary coordinates as a function of integral Kp grouped (top to bottom) by MLT sectors: dawn, day, dusk, and all.**

In this study, however, 166 DMSP data points were obtained between 11-13 MLT with an energy threshold of 0.4 erg/cm<sup>2</sup>/s. The OH, OP, and NH models, when run for

the same conditions, often did not determine a boundary in the corresponding MLT sector. In other words, the model's output never met or exceeded the energy flux threshold.

The charts in Figure 29 show the data loss statistics for each of the models using a threshold of 0.4 erg/cm<sup>2</sup>/s. The OP model had 3.5% loss, found almost entirely between 1130-1230 MLT. The OH model's loss percentage was 6.3%, and it had the most losses between 1100-1300 MLT. The NH model, however, did not compute a boundary for 18.2% of the DMSP data, and it also exhibited significant losses between 14-16 MLT unlike the other models.

The loss patterns underscore the difficulties associated with modeling the dayside precipitation patterns. The problem is only exacerbated when utilizing higher flux thresholds. Using 1.0 erg/cm<sup>2</sup>/s as a threshold, more than 35% of the DMSP data was unusable because the models did not calculate a boundary to compare against. Because of this, the 0.4 erg/cm<sup>2</sup>/s threshold is primarily considered in the determination of the models' performance. All of the loss percentages are listed in Table 12.

**Table 12. Percentages of data lost for the NH, OH, and OP models at each energy flux threshold.**

|    | Thresholds |      |      |
|----|------------|------|------|
|    | 0.4        | 0.6  | 1.0  |
| NH | 18.2       | 29.5 | 48.2 |
| OH | 6.3        | 19.9 | 36.9 |
| OP | 3.5        | 17.7 | 41.9 |

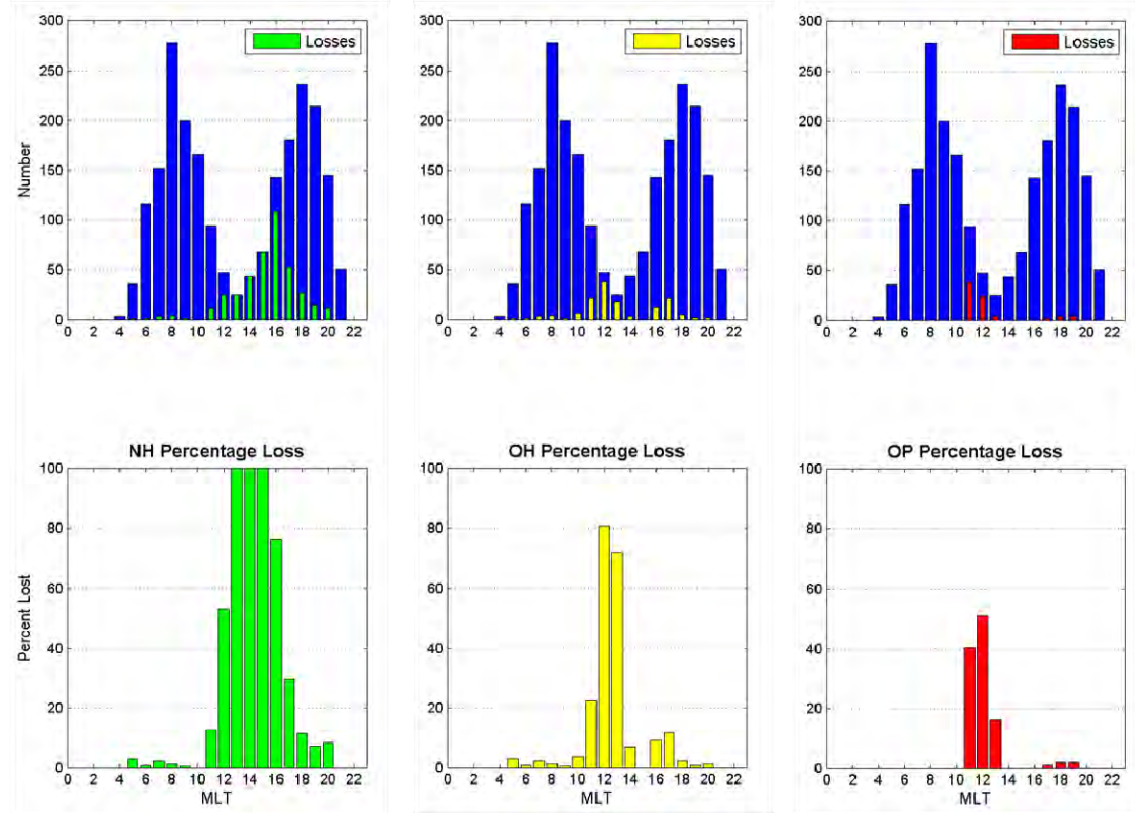


**Figure 29.** Top row: Data losses using  $0.4 \text{ erg/cm}^2/\text{s}$  threshold for NH model (left), OH model (center), and OP model (right). Bottom row: Percentage of available DMSP passes lost in each MLT sector.

There was one additional factor to consider regarding the boundary produced by the OP model. Even though the OP model had the lowest loss percentage using the  $0.4 \text{ erg/cm}^2/\text{s}$  threshold, it did not necessarily calculate a physically reasonable boundary position. An example of this characteristic of the OP model is shown in Figure 30. In the 14, 15, and 22 MLT sectors, there are non-physical jumps in the equatorward boundary location. These boundary locations are particularly troublesome because they satisfied the more rigorous criteria set forth in Chapter III designed to reduce the OH model's anomalies. The corresponding synoptic plot is also shown in Figure 30, which clearly demonstrates the scope of the problem. It is apparent that requiring three consecutive energy flux values to meet or exceed the threshold does eliminate the majority of

anomalous energy fluxes. However, in order not to introduce additional biases in this comparative study, any boundary locations satisfying the more stringent criterion were included as part of OP model's accepted output.

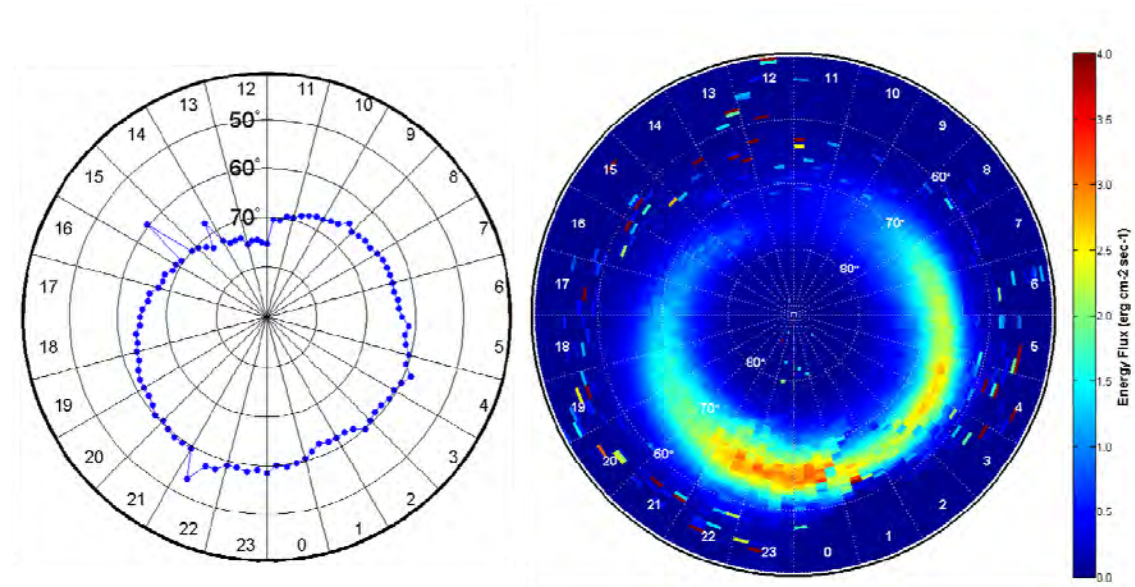


**Figure 30.** OP model output for data obtained on August 31, 2001 during Kp 3 conditions. Data points in the 14, 15, and 22 MLT sectors demonstrate peculiar boundary locations that were nevertheless included in the study because they satisfied the already more stringent selection requirements.

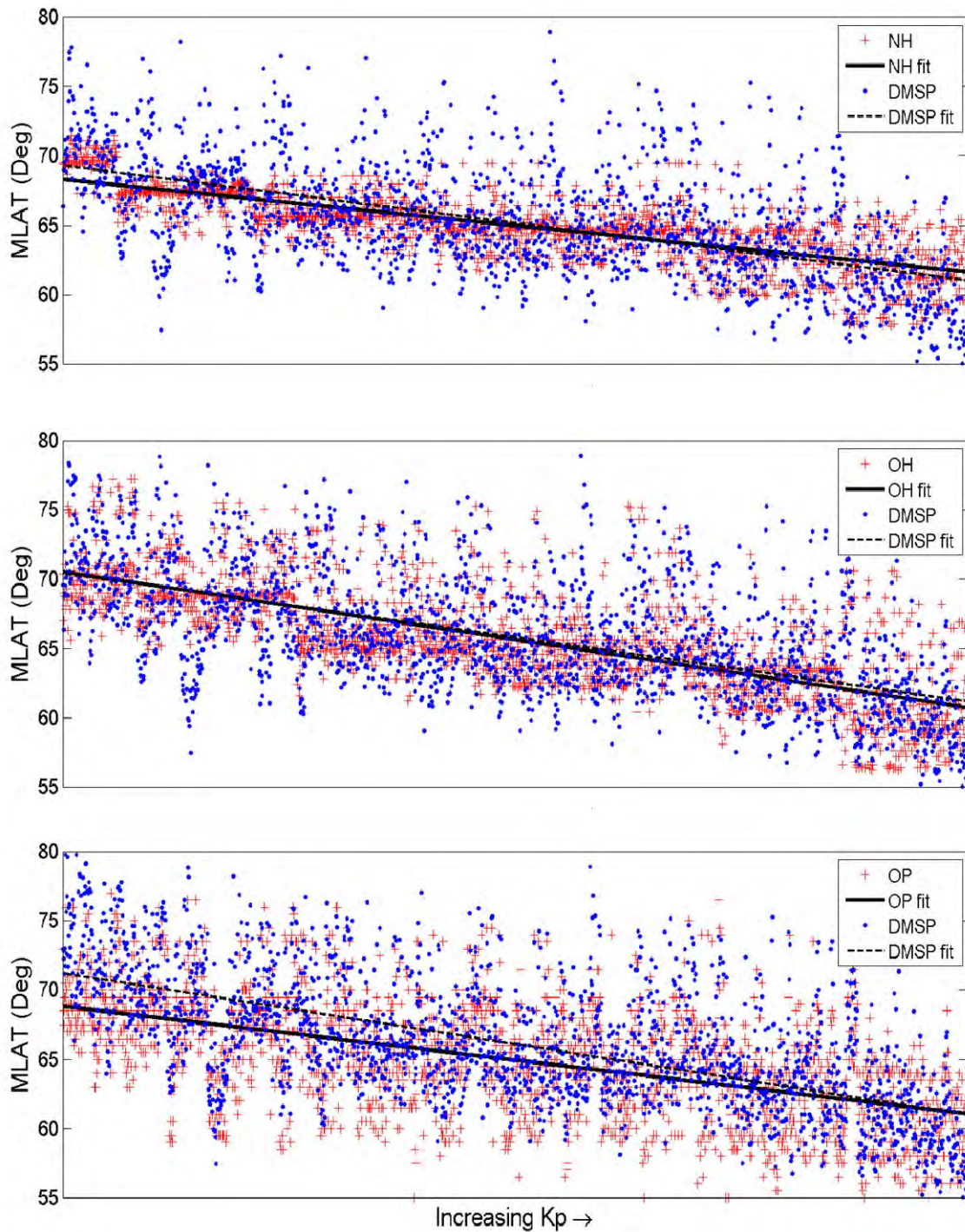
## 4.2 Individual Model Characteristics as a Function of Kp Index

Qualitative information about the models' performance can be gained by looking at general patterns of their output. The series of plots shown in Figure 31 depict the DMSP data set overlaid on the same data set for a particular model. There is the same number of red and blue points in each plot, but due to differing data losses among the models, the total number of data points in each plot is different. The data is ordered such that moving from left to right every subsequent red or blue point represents a measurement taken during either an equivalent or a higher Kp than the one preceding it. The model's linear

trend line is shown in solid black, and the DMSP trend line is dashed. These lines depict the best fit, but the degree of correlation is not important to the ensuing qualitative discussion.

Although the DMSP and model data exhibit significant scatter, the results obtained are consistent with theoretical prediction. The trend lines clearly show that each model exhibits an equatorward migration of its boundary crossing MLAT coordinates with increasing K<sub>p</sub>. By comparing the trend lines, the OH model appears to qualitatively match the DMSP data the best, but some of the other models also show good performance. The OP model's trend line more closely matches the DMSP data as K<sub>p</sub> increases, whereas, the NH and SWMF models go from overestimating the boundary at low Kps to slightly underestimating it at high Kps. Finally, the AMIE model depicts a nearly uniform equatorward bias at all Kps, but the slopes of the trend lines appear nearly equal.

Thus, the series of plots in Figure 31 provide the first qualitative indication that a model's accuracy may be dependent upon K<sub>p</sub> index. The SWMF model is a particularly good example of this. This model's performance appears to be very poor at low Kps, but as the K<sub>p</sub> index increases, the deviation becomes much smaller.



(continued on next page)

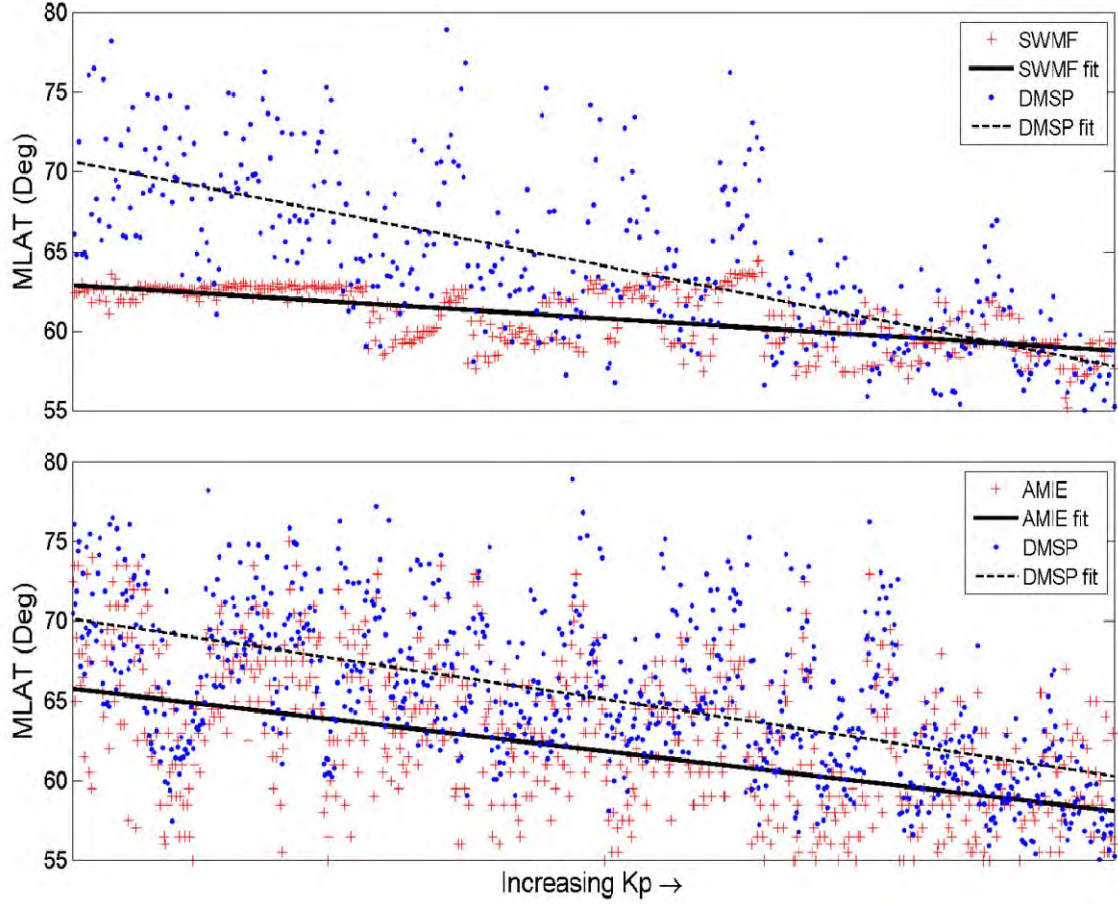


**Figure 31.** Plots of DMSP and NH, OH, OP, SWMF, and AMIE (top to bottom) as functions of increasing  $K_p$  between  $K_p 1$  and  $K_p 8+$ . Black lines indicate data trend.

### 4.3 Model Accuracy Comparisons

To begin assessing and comparing the performance of the models, the broadly applicable ratio estimate will be used to expand upon some of the observed qualitative trends. Then, the remainder of this section will present the results of the comprehensive statistical study designed to measure each model's accuracy. This will include a discussion of average deviations and prediction estimate scores. Finally, the most successful models will be compared to each other, and through the use of the skill scores, a most accurate model will be designated.

#### **4.3.1 Ratio Estimate**

The ratio estimate (RE) was defined in Chapter III and pertains to the data and applies to the average characteristics of the dataset in question. The optimum RE value is 1, indicating the means of the two data sets are equal. If the RE is greater than 1, then the model's average output is more equatorward than the DMSP satellite data. An RE value less than 1 indicates the opposite.

The RE can be misleading because small deviations may be indicative of much larger errors. For example, an RE of 1.05 at 70° MLAT corresponds to a 3.5° deviation, which is equivalent to a transverse distance of approximately 430 km at a DMSP satellite's orbit. Each model's ratio estimates are displayed in Table 13.

A few trends are observed with regard to RE. First, SWMF and AMIE have high RE values in the low and moderate Kp index ranges but perform better during stormy conditions. All of the models perform well during high-Kp events, except for the NH model, which underestimates the equatorward expansion of the oval. Otherwise, both the NH and OH models have RE values very close to 1.00 during all conditions. The OP model also performs suitably well, though at low and moderate Kps, it tends to locate the boundary more equatorward than is seen in the DMSP data. However, because the ratio estimate is solely based upon mean values, it only describes the general correlation between the model and DMSP data without regard for any variance in the data. With this in mind, the study now looks to complement the RE statistics by considering the standard deviation of each model's data set as well.

**Table 13. Ratio estimates for each model binned by Kp conditions.**

|                | <b>NH</b> | <b>OH</b> | <b>OP</b> | <b>SWMF</b> | <b>AIME</b> |
|----------------|-----------|-----------|-----------|-------------|-------------|
| <b>All Kp</b>  | 1.00      | 1.00      | 1.02      | 1.06        | 1.05        |
| <b>Low Kp</b>  | 1.01      | 1.00      | 1.03      | 1.11        | 1.06        |
| <b>Mod Kp</b>  | 1.01      | 1.01      | 1.02      | 1.06        | 1.06        |
| <b>High Kp</b> | 0.96      | 0.98      | 0.99      | 0.99        | 1.01        |

#### 4.3.2 Mean Deviation between DMSP and Model

Figure 32 presents five charts that summarize the basic statistics of each model's deviation from the DMSP data. These charts were constructed using all of the data obtained in this study and do not represent any subdivision into any of the previously described categories. These charts summarize the results of calculating the individual differences between each DMSP data point and the corresponding data point determined by each of the models. If a difference is negative, it indicates the model's boundary is more poleward (i.e., at a higher MLAT) than the DMSP boundary. A perfect model would have a mean difference of 0, and the standard deviation of the distribution plot of the difference statistics would also be equal to 0. Therefore, small values in both statistics are indicative of accurate model performance.

The plots in Figure 32 depict the distribution of all of the differences rounded to the nearest integer between -10 and 10. If the difference between the DMSP boundary and a model's boundary exceeded  $\pm 10$ , it was counted in the 10 or -10 bins respectively. To facilitate comparison, the mean value of the differences and the standard deviation of the differences were calculated.

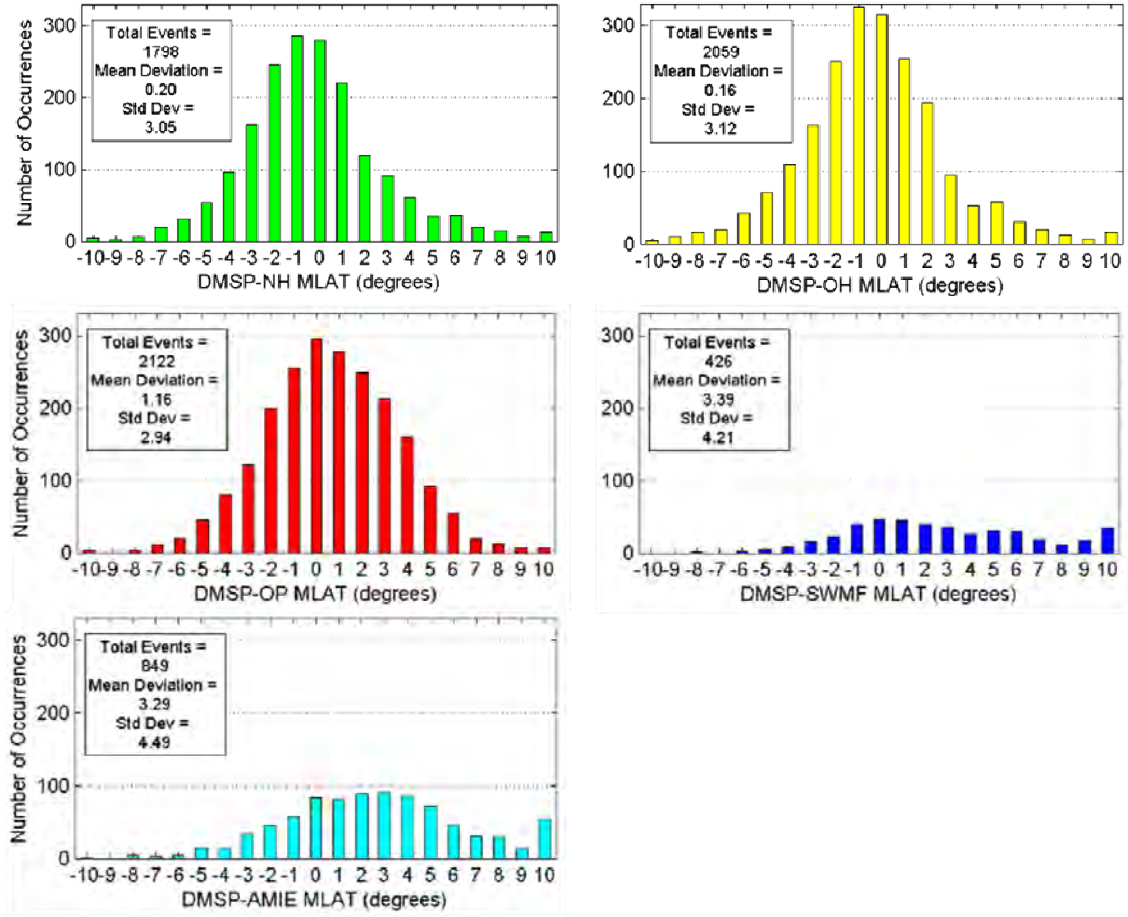


**Figure 32. MLAT deviations (DMSP-model) binned in integral steps using  $0.4 \text{ erg/cm}^2/\text{s}$  threshold. Entire data set has been included. NH (green), OH (yellow), OP (red), SWMF (blue), AMIE (cyan).**

The NH model's average deviation was  $0.20^\circ$  MLAT, and the OH model's was  $0.16^\circ$ . The OP model's average displacement was  $1.16^\circ$ , indicating it calculated a more equatorward boundary on average. This result is consistent with the qualitative trends observed in Figure 31. The standard deviation of the NH, OH, and OP models is 3.05, 3.12, and  $2.94^\circ$  respectively. As a reminder, these values represent standard deviations of the deviation data. No other similar study published the standard deviations in this way, so it is impossible to compare these results to others. However, an error of  $\pm 3^\circ$  MLAT equates to more than 350 km of transit for a DMSP satellite orbit, so the amount of uncertainty, as revealed by these statistics is considerable.

The similarity in standard deviations for NH, OH, and OP models is interesting, though, because the OH and NH models are highly discretized (binned by integral K<sub>p</sub> value), whereas the OP model ingests many dynamic parameters tied to small changes in the geomagnetic conditions. Said differently, the considerably more computationally complex OP model does not achieve noticeably lower deviations from the DMSP data than does its more simply designed peers.

The average performance of SWMF and AMIE are poor by comparison. Not only did both models locate the boundary at significantly lower MLATs, but both also have high standard deviations. Because these calculations are based upon the entire data set, there is no consideration given to the possibility of a model exhibiting a high degree of accuracy in a particular subcategory. If the data is broken down into K<sub>p</sub> groups, as was done with the RE calculation, the performance statistics change.

For example, when only high-K<sub>p</sub> conditions (i.e., K<sub>p</sub> > 6-) are considered, SWMF and AMIE experience marked improvement. All of the models' performance results under these conditions are shown in Figure 33. Under these circumstances, the mean deviations of NH, OH, and OP are now negative, meaning these model's boundary locations are more poleward on average. The NH model's mean deviation shifted 2.96°, and the OH and OP model shifted 1.14° and 1.94° respectively. These shifts represent a significant change in each model's performance.

The SWMF model's mean deviation experiences a 3.03° change, going from 3.39° to -0.36°. This is the likely result of the model's effective indifference to K<sub>p</sub> conditions. Put a different way, the SWMF model appears to be preconditioned to model high-K<sub>p</sub> events only, which is why its scores are poorer during quieter conditions. The

AMIE model appears to improve, but the standard deviation of its data warrants caution in making any conclusions. Its deviations are more spread out than the other models, which definitely limits any confidence in its reliability.

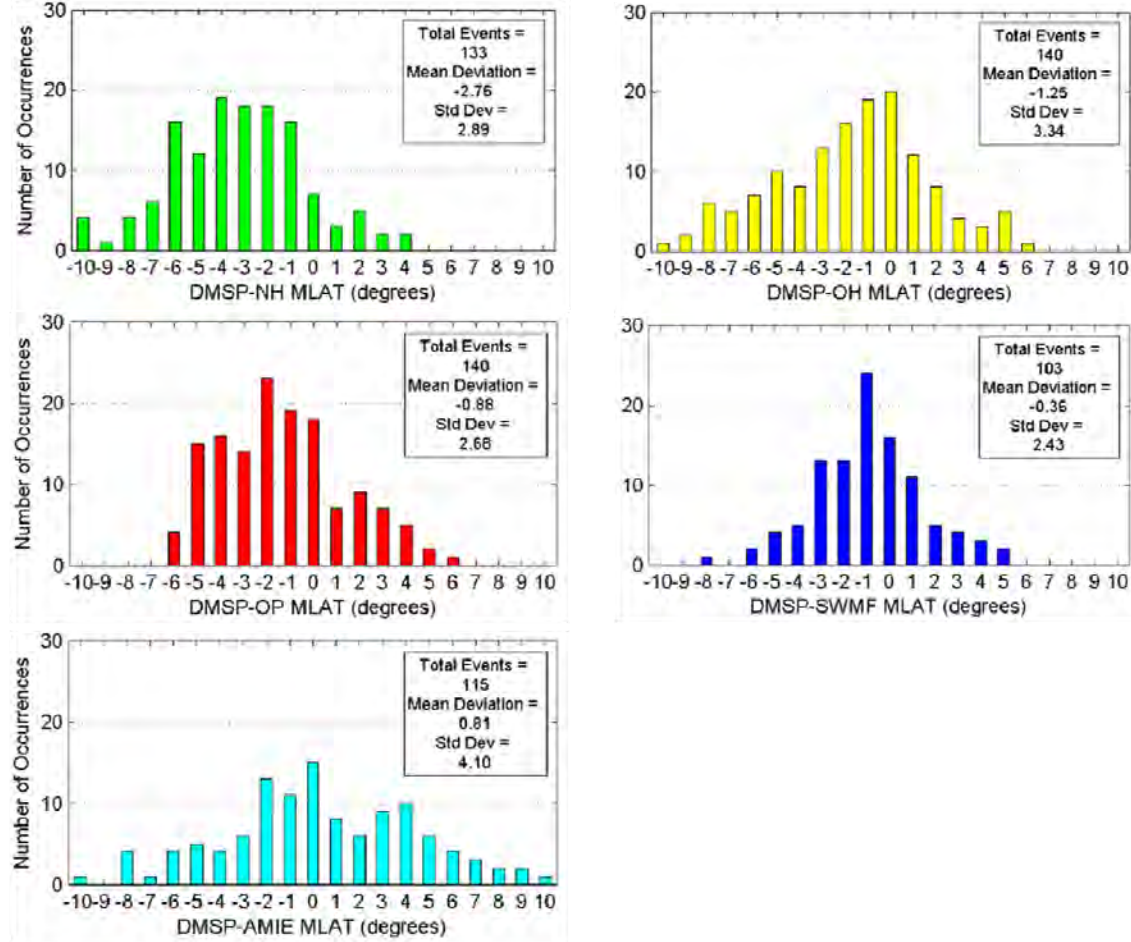


Figure 33. Same as Figure 32 but for  $K_p > 6$  only.

Categorizing the models based upon geomagnetic activity levels is one way the models can be measured. However, based upon the earlier discussion of the variability in the aurora based upon MLT sector, this study also sought to examine any changes to the models' accuracies with regard to time of day and time of year. As the data is grouped into smaller and more specific representations, some models exhibit particular strengths.

Table 14 lists the models with the lowest average deviation in each subcategory. Spring and fall seasonal statistics were excluded because not enough data during these seasons was introduced into this study. The same circumstance was true for the 10-15 MLT statistics during high Kp conditions. These unfortunate gaps represent an avenue for continued research.

**Table 14. Lowest average deviations during dawn, day, and dusk MLT sectors and winter and summer seasons for high, moderate, and low Kp conditions. Table entries represent deviation in degrees of MLAT. Direction of deviation (equatorward or poleward) was not factored into ranking.**

| MLT           | High Kp |       | Moderate Kp |       | Low Kp |       |
|---------------|---------|-------|-------------|-------|--------|-------|
| <b>04-09</b>  | SWMF    | -0.33 | NH          | 0.18  | OH     | 0.38  |
| <b>10-15</b>  | --      | --    | NH          | 0.40  | NH     | -0.40 |
| <b>16-21</b>  | SWMF    | -0.67 | OP          | -0.87 | OH     | -0.32 |
| Season        | High Kp |       | Moderate Kp |       | Low Kp |       |
| <b>Winter</b> | SWMF    | 0.17  | NH          | 0.67  | OH     | 0.59  |
| <b>Summer</b> | OH      | -0.07 | NH          | 0.13  | NH     | 0.31  |

During storming events, the SWMF model's boundary location is the closest on average regardless of the MLT sector, and it also models well during winter. During moderate-Kp events, the NH model performs best from 04-15 MLT, and the OP model does the best from 16-21 MLT. The NH model remains the top performer during winter and summer. During quiet conditions, the equatorward boundary is most closely represented, on average, by the OH model from 04-09, from 16-21 MLT, and during summer. The NH model has the lowest deviation from 10-15 MLT and during summer.

Although none of the models is clearly dominant in all categories, based upon these results, the NH, OH, OP, and SMWF models have earned credibility in specific niches. Each of these models demonstrates comparatively good performance in at least one Kp and/or MLT regime. The SWMF model is ranked highest in 2 of 8 MLT

categories and 1 seasonal category. The OH model earns 2 MLT categories and 2 seasonal categories. The NH model has the highest number of categories—3 MLT and 3 seasonal. Somewhat surprisingly, the OP model only has the lowest deviation in one of the MLT categories.

#### **4.3.3 Prediction Efficiency (PE)**

The mean deviation is an important consideration, but it does not tell the full story. Comparative studies of this sort are well-suited for prediction efficiency (PE) calculations. The PE is useful because it measures the percentage of variance in the observed data (here, DMSP data) that is explained by the model. Thus, a perfect PE score is 1, indicating 100% of the model's variance has been captured by the model. Contrarily, any score less than 0 indicates the model's variance exceeds the variance in the DMSP data. In this unfavorable case, using the mean of the observed data serves as a more accurate predictor, on average, than using the model.

Table 15 lists the PE scores when the data is divided into Kp groups and then is further subdivided into MLT sectors. In order for a score to be calculated, more than 20 data points had to exist within the category. The top line of the table lists the PE scores for the entire data set. In this aggregate condition, the OP model receives the highest PE score. It is followed by the OH model and then the NH model. Neither the SWMF nor AMIE model has a positive PE when all of the data is considered.

**Table 15. Prediction efficiency scores. Negative PEs are indicated by (--). Green box represents best PE in that category.**

| MLT          | Kp   | NH                | OH   | OP   | SWMF | AMIE |
|--------------|------|-------------------|------|------|------|------|
| <b>04-21</b> | All  | 0.45              | 0.51 | 0.55 | --   | --   |
| <b>04-21</b> | High | --                | --   | 0.13 | 0.29 | --   |
|              | Mod  | 0.32              | 0.31 | 0.30 | --   | --   |
|              | Low  | 0.22              | 0.34 | 0.37 | --   | --   |
| <b>04-09</b> | High | --                | --   | --   | 0.32 | --   |
|              | Mod  | 0.19              | 0.05 | 0.30 | --   | --   |
|              | Low  | 0.19              | 0.06 | 0.10 | --   | --   |
| <b>10-15</b> | High | Insufficient Data |      |      |      |      |
|              | Mod  | 0.06              | 0.21 | 0.12 | --   | --   |
|              | Low  | --                | 0.40 | 0.38 | --   | --   |
| <b>16-21</b> | High | --                | --   | 0.15 | 0.25 | --   |
|              | Mod  | 0.39              | 0.35 | 0.19 | --   | --   |
|              | Low  | 0.07              | 0.36 | 0.37 | --   | --   |

The OP model receives a positive PE in all of the categories except for high-Kp events occurring between 04-09 MLT, which indicates strong performance. However, its scores during the other high-Kp categories are relatively low. The OH and NH models fare even worse during periods of significant geomagnetic storming; both have negative scores in each of the MLT categories during high-Kp conditions. The SWMF model has the highest PE scores in all MLT sectors during high-Kp events. This fact, combined with its low mean deviation, indicate the SWMF model is the most accurate during high-Kp events.

There is no decisive winner when considering the PEs in Table 15 during other activity levels and times of day, and any broad conclusions would be rife with caveats. For example, when the Kp index is low, both OP and OH fare well, but not in the dawn sector, where the NH model has the highest PE. However, the top-ranked NH model only accounts for 19% of the variance of the DMSP data in this subcategory, and this

underscores poor performance for all of the models. A similar situation occurs during moderate-Kp events between 10-15 MLT. In this case, the OH model only accounts for 21% of the DMSP variance, but this score is almost twice the OP model's score of 12%.

The PEs calculated using data occurring during winter and summer are listed in Table 16. Generally speaking, the PE scores are slightly higher than what was found in the previous table. Except for case of high Kp during winter, the OP model performs well in all categories and could justifiably be declared the best performing model in consideration of these categories. Combined with the previous results, the OP model has begun to establish itself as a front-runner.

But, other models also perform well under certain circumstances. The OH model does comparatively well during the summer months and also during the moderate-Kp events during the winter. It also does quite well in the summer months when the Kp index is high. The NH model does not have any of the highest scores, but it does not necessarily languish either. It performs poorly during high and low-Kp events in the winter and high-Kp events in the summer. The SWMF model again performs well in a high-Kp category, as it has the only positive PE score during the winter months.

**Table 16. Same as Table 15 but data is grouped by season.**

| Season | Kp   | NH   | OH   | OP   | SWMF | AMIE |
|--------|------|------|------|------|------|------|
| Winter | High | --   | --   | --   | 0.30 | --   |
|        | Mod  | 0.38 | 0.46 | 0.45 | --   | --   |
|        | Low  | --   | 0.03 | 0.29 | --   | --   |
| Summer | High | --   | 0.45 | 0.28 | 0.08 | --   |
|        | Mod  | 0.30 | 0.28 | 0.49 | --   | --   |
|        | Low  | 0.28 | 0.34 | 0.46 | --   | --   |

#### **4.3.4 Skill Score**

The last performance measure investigated in this study is the skill score (SS).

Development of meaningful skill scores requires the selection of one model as the reference. For the purposes of this study, the OH model will be used in this capacity, and it will be compared to the NH and OP models. The SWMF model's performance in all other categories except for high-K<sub>p</sub> and the AMIE model's overall performance do not warrant performing a skill score analysis on these models.

A perfect SS is 1, which indicates the test model and all observations are in perfect agreement. A positive SS means the test model provides a better forecast than the reference model, but the SS does not necessarily imply any degree of accuracy. That is, if the reference, itself, was inaccurate, the SS only indicates whether or not the test model performed better. However, there is a distinct possibility the test model's predictive capacity is also quite poor.

The data in Table 17 summarizes the SS results. A green box designates a positive score. Analysis of the skill scores shows that the NH model is an improvement over the OH model under the majority of low- and moderate-K<sub>p</sub> events. However, it must be noted that all of the NH scores are only slightly positive and are less than 0.15. This indicates a very modest improvement over the OH model. By contrast, the OP model has fewer positive scores, but some of its scores are much greater than the NH model's. The OP model provides a particular advantage over the OH model during high K<sub>p</sub> events.

These SS results are intended to complement the PE analysis, but nuances do exist. In the case of the low-K<sub>p</sub> events occurring in the 16-21 MLT sector, the results

appear to be in stark contrast to those found using the PE. The number of NH and OP data points used in computing the skill score was not necessarily the same, due to the potential for data losses described in an earlier section. In this case highlighted here, the OP skill score was determined using 235 points, while the NH skill score only used 124 points. Refer to Figure 29 for the specific loss statistics associated with the 16-21 MLT sector.

**Table 17. Skill scores. Green boxes indicate the model performed better than the OH reference model.**

| MLT          | Kp   | n                 | NH    | n    | OP    |
|--------------|------|-------------------|-------|------|-------|
| <b>04-21</b> | All  | 1763              | 0.07  | 2018 | 0.01  |
| <b>04-21</b> | High | 133               | -0.37 | 140  | 0.37  |
|              | Mod  | 1198              | 0.14  | 1299 | -0.02 |
|              | Low  | 432               | 0.05  | 579  | -0.05 |
| <b>04-09</b> | High | 58                | -0.53 | 58   | 0.30  |
|              | Mod  | 486               | 0.15  | 486  | 0.27  |
|              | Low  | 231               | 0.13  | 231  | 0.05  |
| <b>10-15</b> | High | Insufficient Data |       |      |       |
|              | Mod  | 146               | 0.14  | 198  | -0.06 |
|              | Low  | 77                | -0.40 | 113  | -0.34 |
| <b>16-21</b> | High | 63                | -0.60 | 67   | 0.18  |
|              | Mod  | 566               | 0.13  | 615  | -0.24 |
|              | Low  | 124               | 0.09  | 235  | -0.07 |

Again, like with the PE, the SS can be also determined with a seasonal dependence. Table 18 summarizes those results. The results are similar to the previous findings. Again, the OP model demonstrates a greater improvement over the reference than does the NH model. Neither model performs better than OH during high-Kp summer events.

**Table 18. Same as Table 17 but with data grouped by season.**

| Season | Kp          | n   | NH    | n   | OP    |
|--------|-------------|-----|-------|-----|-------|
| Winter | <b>High</b> | 49  | -0.39 | 55  | 0.40  |
|        | <b>Mod</b>  | 275 | 0.14  | 300 | 0.04  |
|        | <b>Low</b>  | 68  | 0.01  | 95  | -0.05 |
| Summer | <b>High</b> | 44  | -1.18 | 44  | -0.03 |
|        | <b>Mod</b>  | 260 | 0.07  | 277 | 0.31  |
|        | <b>Low</b>  | 211 | 0.02  | 288 | 0.20  |

## 4.4 Comparative Statistics Using Different Thresholds

As was mentioned in the first section of this chapter, the same experimental procedures were performed when representing the boundary with higher energy flux thresholds. The original intention of this was to vet the results found using the 0.4 erg/cm<sup>2</sup>/ threshold with results obtained using 0.6 and 1.0 erg/cm<sup>2</sup>/s thresholds. It was discovered the model's often did not compute any flux values at or above 1.0 erg/cm<sup>2</sup>/s, reducing the available data set by nearly 50%.

In some cases, especially during low-Kp events, the DMSP satellite also did not record such a high energy flux value. However, the more prolific problem with the DMSP data pertained to the physical processes occurring in the magnetosphere. In Chapter II, it was shown the energy dependent dominance of the gradient drift results in a steep energy gradient that is often observed at the equatorward boundary of the auroral oval. However, particularly during quiet activity, particle energies in the boundary region of the plasma sheet are reduced, and this causes a shallower onset of energies. Large energy fluxes, however, may still exist well inside of the auroral oval due to the diverse population of particle energies found in central plasma sheet.

Both of these circumstances are depicted in Figure 34, which depicts two satellite passes during low K<sub>p</sub> conditions. In the panel on the left, the satellite did not encounter an energy flux value above the 1.0 erg/cm<sup>2</sup>/s threshold, where it would have for a lower fixed value. In the plot on the right, the threshold is crossed well inside of the auroral oval, which is clearly not indicative of the equatorward boundary. As a result, it was determined that this flux threshold could not be reliably and consistently associated with the equatorward boundary, and the data was removed from the study.

However, the data obtained using a 0.6 erg/cm<sup>2</sup>/s threshold was set at an appropriate level and did not encounter the same issues with data losses and unrepresentative threshold crossings. Thus, the data obtained with this threshold was used to correlate to the results obtained using 0.4 erg/cm<sup>2</sup>/s. The distribution plots of the differences are shown in Figure 35. Again, this data was calculated using the entire data set and was not divided into any subcategories.

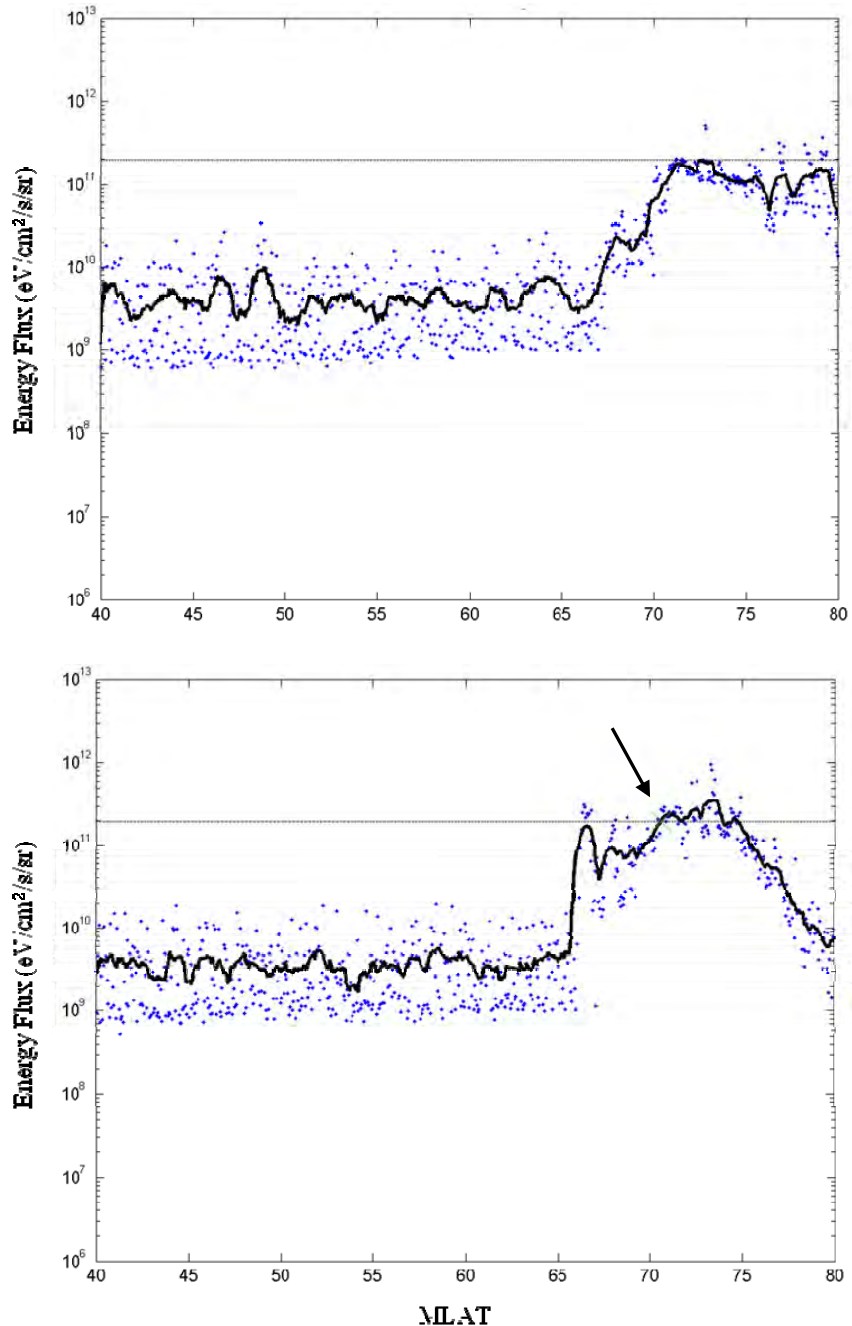


**Figure 34.** Examples of data loss using 1.0 erg/cm<sup>2</sup>/s threshold. Top plot demonstrates situation where no boundary occurred due to low energy throughout the auroral zone. Bottom plot demonstrates a misplaced boundary (black arrow) located well inside auroral oval based upon central plasma sheet particle energies.

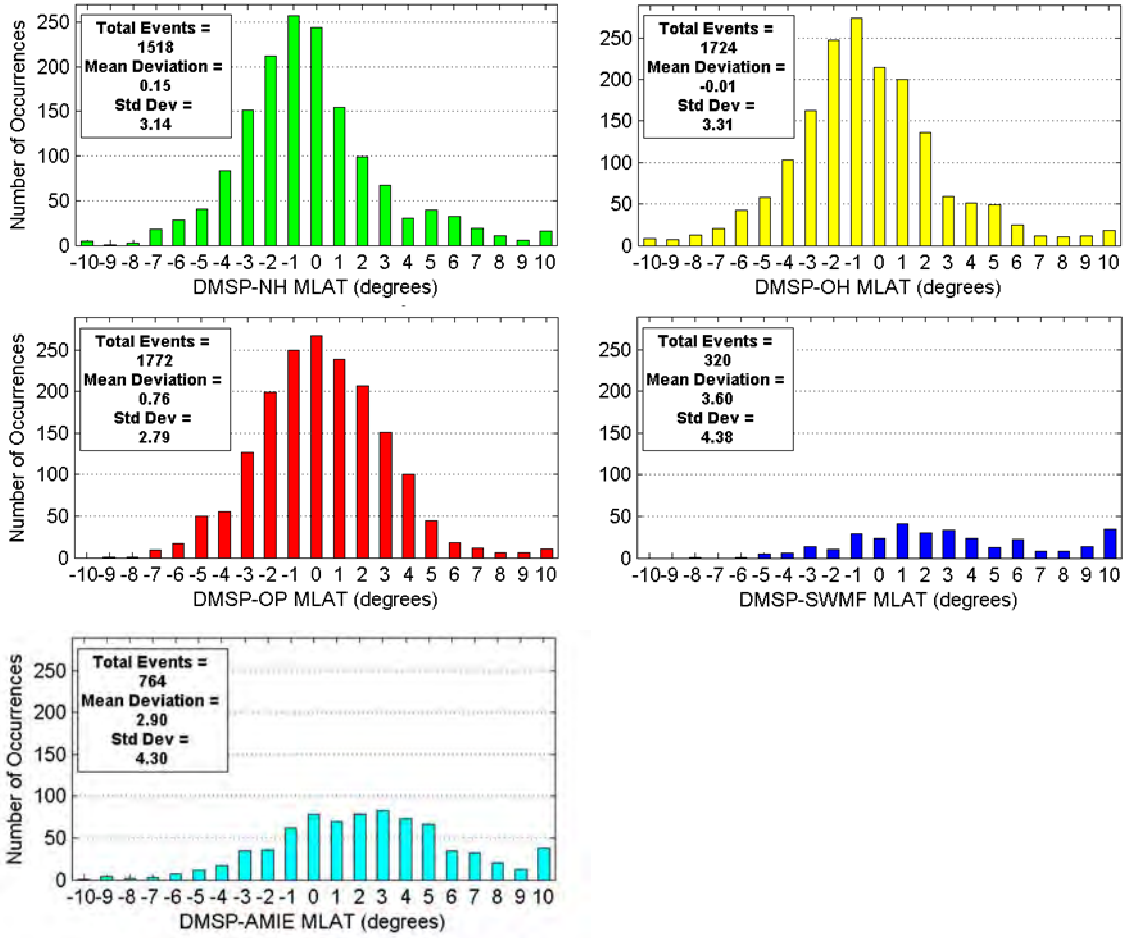


**Figure 35. MLAT deviations (DMSP-model) binned in integral steps using 0.6 erg/cm<sup>2</sup>/s threshold. Entire data set has been included. NH (green), OH (yellow), OP (red), SWMF (blue), AMIE (cyan).**

These charts show similar results to what was calculated using the lower threshold. The OH and NH models have the lowest average deviations. The OP model exhibits an improvement in its mean difference and has a standard deviation that is very low compared to its peers. Neither the SWMF nor the AMIE models exhibit an enhancement in accuracy. Table 19 provides a comparison of each model's difference statistics using both thresholds.

**Table 19.** Comparison of mean deviation and standard deviation using different energy flux thresholds.

| Thresh |          | NH   | OH    | OP   | SWMF | AMIE |
|--------|----------|------|-------|------|------|------|
| 0.4    | N        | 1798 | 2059  | 2122 | 426  | 849  |
|        | $\mu$    | 0.20 | 0.16  | 1.16 | 3.39 | 3.29 |
|        | $\sigma$ | 3.05 | 3.12  | 2.94 | 4.21 | 4.49 |
| 0.6    | N        | 1518 | 1724  | 1772 | 320  | 764  |
|        | $\mu$    | 0.15 | -0.01 | 0.76 | 3.60 | 2.90 |
|        | $\sigma$ | 3.14 | 3.31  | 2.79 | 4.38 | 4.30 |

The data in Table 20 summarizes the prediction efficiency scores when using a flux threshold of 0.6 erg/cm<sup>2</sup>/s. As was found with the lower threshold, the SWMF model has the highest PE during high-Kp conditions from 04-15 MLT, but at the higher threshold, the OP model now has the highest score in evening sector. The OP model achieves higher scores in the majority of the other categories.

**Table 20.** Prediction efficiency score comparison using 0.6 erg/cm<sup>2</sup>/s threshold. Negative PEs are indicated by (--). Green box represents highest PE in that category.

| MLT   | Kp   | NH                | OH   | OP   | SWMF | AMIE |
|-------|------|-------------------|------|------|------|------|
| 04-21 | All  | 0.44              | 0.41 | 0.58 | --   | --   |
| 04-21 | High | --                | --   | 0.16 | 0.24 | --   |
|       | Mod  | 0.31              | 0.29 | 0.39 | --   | --   |
|       | Low  | 0.14              | 0.11 | 0.47 | --   | --   |
| 04-09 | High | --                | --   | --   | 0.55 | --   |
|       | Mod  | 0.16              | 0.07 | 0.31 | --   | --   |
|       | Low  | 0.11              | --   | 0.20 | --   | --   |
| 10-15 | High | Insufficient Data |      |      |      |      |
|       | Mod  | --                | 0.12 | 0.40 | --   | 0.21 |
|       | Low  | --                | 0.17 | 0.58 | --   | --   |
| 16-21 | High | --                | --   | 0.29 | 0.16 | --   |
|       | Mod  | 0.37              | 0.40 | 0.32 | --   | --   |
|       | Low  | --                | 0.13 | 0.40 | --   | --   |

Comparing the PE results for each threshold reveals that 10 of 10 OP model scores were higher using the higher energy flux threshold, while 5 of 5 NH scores and 5 of 7 OH scores were lower. The reason for the surge in OP performance is not inherently obvious but can be partially explained by investigating differences between the data sets obtained using the different thresholds.

Referring back to Table 9, the DMSP data obtained using the 0.6 erg/cm<sup>2</sup>/s threshold has a larger variance than the data obtained using the lower threshold in 8 of the 9 Kp categories. Referring to Equation (7), if the differences between the model and observed data remain the same, a larger variance in the DMSP data should result in higher PE scores for all of the models. Thus, in order for the NH and OH model's scores to have decreased, the average difference between each of them and the DMSP data must have increased. This is the term in the numerator of Equation (7).

In Figure 36, the corresponding threshold crossing points for the low (blue) and high (red) flux thresholds are overlaid on the same plot for the NH, OH, and OP models. The boundaries in these plots correspond to a Kp index of 3. Panel (a) and panel (b) show the NH and OH model boundaries are virtually identical. Although the higher flux boundary is very slightly displaced toward the pole, which is consistent with theory, there is very little displacement. Panel (c) shows the OP model's output, and its higher energy boundary is also more poleward as well. However, its displacement is slightly larger.

Again, referring to the statistics in Table 9, the DMSP crossing points are located, on average, more poleward at the higher flux threshold. This more significant displacement of the OP model thus reduces the term in the numerator of Equation (7) more so than either the NH or OH models. This, results in higher PE scores for the OP

model. The NH and OH models, whose outputs are virtually indistinguishable, are better suited modeling boundaries associated with lower energy fluxes.

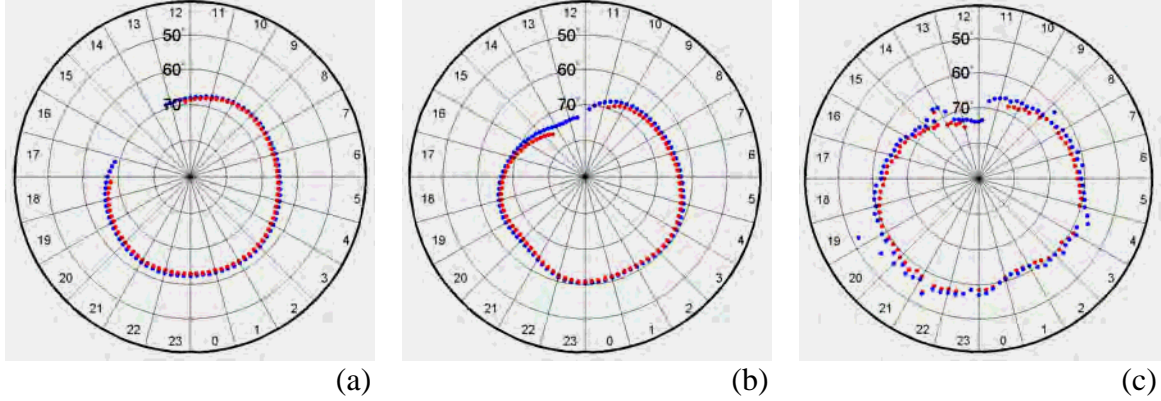


**Figure 36. Boundary plots at 0.4 (red) and 0.6 (blue)  $\text{erg}/\text{cm}^2/\text{s}$  thresholds for (a) NH, (b) OH, and (c) OP. Plots represent conditions with Kp 3.**

A list of the model with the top prediction efficiency score in each subcategory for both flux thresholds is provided in Table 21. Some general conclusions can be gleaned from the low-flux results. The SWMF model has clearly carved out a niche modeling the oval's equatorward boundary during most high-Kp events. The OP model does well at modeling many of the low-Kp conditions. Moderate-Kp events, those with Kp index values between 3 and 6, are relatively split between the NH, OH, and OP models. If the data is parsed into any subcategorizes at all, then the OP model has the highest PE scores using both thresholds.

**Table 21.** Top prediction efficiency scores in each subcategory using 0.4 and 0.6 erg/cm<sup>2</sup>/s thresholds.

|             |      | 0.4  |      | 0.6  |      |
|-------------|------|------|------|------|------|
| SEASONS     | High | SWMF | 0.30 | --   | --   |
|             |      | OH   | 0.46 | OP   | 0.51 |
|             |      | OP   | 0.29 | OP   | 0.16 |
|             | High | SWMF | 0.22 | SWMF | 0.21 |
|             |      | NH   | 0.14 | OP   | 0.16 |
|             |      | OP   | 0.32 | OP   | 0.15 |
|             | High | OH   | 0.45 | OP   | 0.32 |
|             |      | OP   | 0.49 | NH   | 0.33 |
|             |      | OP   | 0.46 | OP   | 0.60 |
|             | Mod  | --   | --   | --   | --   |
|             |      | NH   | 0.38 | OP   | 0.52 |
|             |      | OH   | 0.44 | OH   | 0.45 |
| MLT SECTORS | High | SWMF | 0.32 | SWMF | 0.55 |
|             |      | OP   | 0.30 | OP   | 0.31 |
|             |      | NH   | 0.19 | OP   | 0.20 |
|             | Mod  | --   | --   | --   | --   |
|             |      | OH   | 0.21 | OP   | 0.40 |
|             |      | OH   | 0.40 | OP   | 0.58 |
|             | Low  | SWMF | 0.25 | OP   | 0.29 |
|             |      | NH   | 0.39 | OH   | 0.40 |
|             |      | OP   | 0.37 | OP   | 0.40 |
| ALL         |      | OP   | 0.55 | OP   | 0.58 |

An attempt to corroborate these broad conclusions using a higher energy flux results highly favors to the OP model, which earned the top score in 13 of 18 categories in which data was available. Table 22 lists the models that had the highest PE score using both the low- and high-energy flux data. This circumstance occurred 8 times out of 18 opportunities. The OP model had five category corroborations, which was the most of any model. Thus, although the results do not permit a decisive determination, this comparative statistical study favors the OP model as the model of choice.

**Table 22. Corroborated categories. In these 8 categories, the same model had the highest PE score using both energy flux thresholds.**

| Season    | Kp   | Model |
|-----------|------|-------|
| Winter    | Low  | OP    |
| Spring    | High | SWMF  |
| Spring    | Low  | OP    |
| Summer    | Low  | OP    |
| Fall      | Low  | OH    |
| 04-09 MLT | High | SWMF  |
| 04-09 MLT | Mod  | OP    |
| 16-21 MLT | Low  | OP    |

## 4.5 Small-scale Experiment Using Predictable Precipitation Patterns

Consideration of the previous statistical measures did not confirm the existence of a superior model. These results underpin the difficulties involved in modeling such a highly dynamic phenomenon. Thus, the following extremely small-scale experiment was devised to determine if providing the models with a small set of well-defined auroral events would affect their statistical scores.

This study used the data from 48 satellite passes. The data was selected such that 3 events were selected from 16 days. Each of the 48 passes was chosen by making a qualitative inspection of the DMSP data plots (see Figure 16). An event was selected if it possessed a steep gradient at the equatorward boundary, so as to reduce the ambiguity in the location of the boundary. Furthermore, only data was chosen that occurred between 17-21 MLT to avoid the inherent difficulties in modeling the dayside auroral precipitation. Table 23 shows how the 48 individual events were distributed with regard to Kp index.

**Table 23. Total number of events during specific Kp index value for small-scale study.**

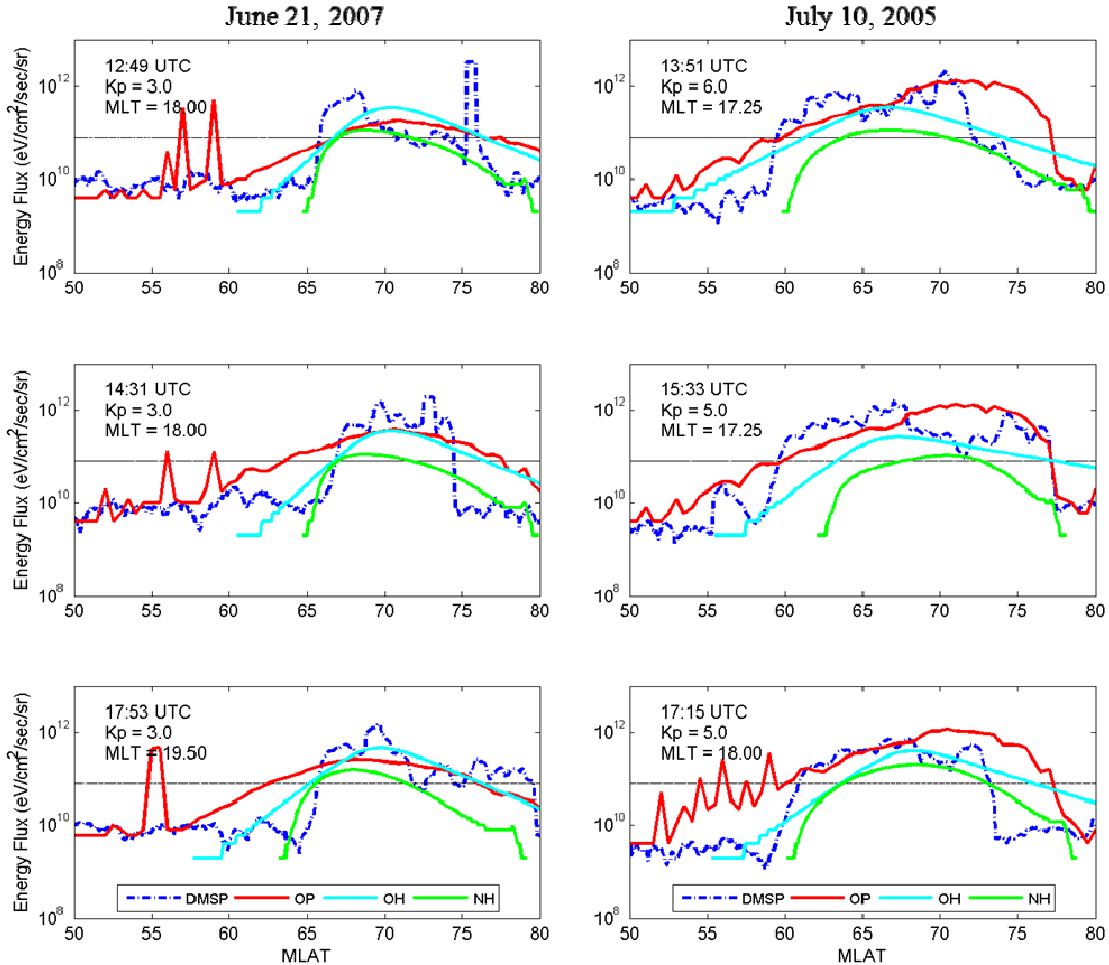
| Kp     | 3  | 4  | 5  | 6-8 |
|--------|----|----|----|-----|
| Number | 13 | 13 | 14 | 8   |

Figure 37 depicts the data obtained from 2 of the 16 days. In the left column, there are three low-Kp events from the same day ordered chronologically from top to bottom. The right column shows three more chronological events from a different day and during stormier conditions. In each plot, the dashed dark blue line represents the 15-second moving average of the DMSP energy flux data. The NH, OH, and OP models results are represented by the solid green, cyan, and red lines respectively.

Using 0.4 erg/cm<sup>2</sup>/s as the threshold, the DMSP MLATs from the three measurements taken during the low-Kp event occurred within a 1.1° span. The MLAT coordinates during the high-Kp event occurred within 1.5°. The three passes used from each day cover a period of 4-5 hours. Such a well-defined boundary location over a considerable amount of time represents relatively static auroral conditions, reducing the variance that pervades the DMSP data in larger samples. This stable boundary location existed in the other 14 days used in this study as well and ultimately provides a template against which the models can be scrutinized.

The sharp spikes in the red line in the low latitudes demonstrate the noisy nature of the OP model that was eliminated by imposing the stricter criterion outlined in Chapter III. The places where no cyan or green line exists represent the latitudes at which no energy flux was calculated by either the OH or NH model. The plots on the left show pictorially that the OH and NH models depict the equatorward boundary consistently well. The intersection of the dark blue, yellow, and green lines with the

black threshold line occurs within a close proximity. Furthermore, the shape of the NH model's line also depicts the steep gradient that closely approximates what is observed in the DMSP data near the boundary. With regard to the low-K<sub>p</sub> conditions, the OP model tends to locate the boundary too far equatorward, with deviations approaching 5° MLAT. And both the OH and OP models depict a more gradual energy flux onset than is shown by the DMSP data, which is inconsistent with the theoretical understanding of the nightside plasma sheet.



**Figure 37.** Chronological data plots of DMSP and model data for low-K<sub>p</sub> (left column) and high-K<sub>p</sub> (right column) events on different days. Horizontal black line represents 0.4 erg/cm<sup>2</sup>/s threshold.

The gradual onset, however, works in the OP model's favor as is shown in the high-K<sub>p</sub> conditions depicted in the right column of Figure 37. Here, the DMSP and OP lines cross the threshold more closely than was seen in the low-K<sub>p</sub> event. However, it is noted the OP model's gradual flux onset (and to a lesser extent the OH model's as well) makes its boundary dependent upon the selected threshold.

Having considered two individual cases, the same statistical analysis can be applied to the entire 48-event dataset. The average deviations for each model are shown in Figure 38. These results seen here validate the intention of the small-scale study. The nightside auroral boundaries chosen for this micro-study have little spatial ambiguity because the energy flux onset occurs so rapidly, and the models have fewer (if any) large deviations.

Although this small study has merely introduced the concept, the idea of consistent and static auroral precipitation patterns is an obvious condition where empirically based models like OH and NH will excel because these types of models have been assembled through statistical and regression analyses on a much larger scale. Generally speaking, the less ambiguous and more consistent auroral precipitation regions complement statistically based models like the OH and NH models.

The scope of this micro study is far too small to make any comprehensive categorizations about accuracy; however, it has been included to underscore the fact that there are aspects of the auroral oval that do not exhibit wild variations and that are well-suited to modeling by purely statistical means. In the absence of this consistency, though, the results obtained in the previous section that, with refinement, the more

dynamic, complex, and comprehensive models like OP do represent progress in this important regime of space weather modeling.

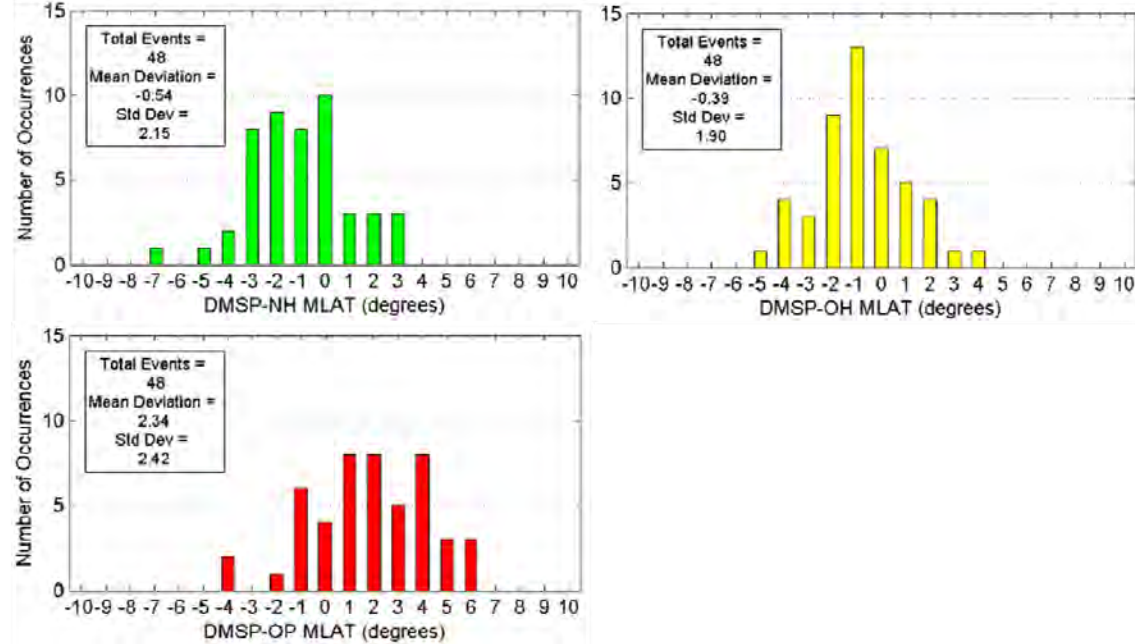


**Figure 38. Deviation plots for NH, OH, and OP models.**

Table 24 summarizes all of the statistics for this small-scale study. The ratio estimations of the NH and OH models show a nearly 1:1 correspondence in boundary migration. It is apparent that when considering a micro-population with a well-defined auroral boundary, the OH model is the most successful model. It has the highest PE score, and the skill scores of the NH and OP models are negative, which also confirms the OH model's performance is superior. Qualitatively speaking, however, the closer resemblance between the DMSP satellite's energy profile and the NH model's energy flux output is a favorable characteristic of this model.

**Table 24. Prediction efficiency, ratio estimates, and skill scores for small-scale investigation. The OH has no SS entry because it served as the reference model.**

|    | NH    | OH   | OP    |
|----|-------|------|-------|
| PE | 0.30  | 0.47 | -0.63 |
| RE | 0.99  | 0.99 | 1.04  |
| SS | -0.15 | --   | -0.75 |

There is another avenue of investigation that this small-scale study supports. Because of the relative stability of the auroral oval over extended periods of time, these plots can also be used to examine some of the characteristics of the evolution of each of the models on a relatively short time scale.

In Figure 39, three chronological plots are shown, and each contains the energy flux profile of the DMSP data and the NH, OH, and OP models in a specific MLT sector. For this example, the time period involves high-K<sub>p</sub> conditions. The vertical lines connecting the plots map depict the migration of the threshold crossing locations. This particular example underscores some important characteristics of each model's behavior and highlights some positive and negative qualities that are tough to discern from a statistical study alone.

In the top panel of the Figure 39, the DMSP threshold crossing is reasonably well represented by all three models. The NH model is displaced poleward, but as before, its energy onset (i.e., gradient) most closely mimics the DMSP data. The data in the second panel was obtained approximately 1 hour and 40 minutes later and was accompanied by a decrease in K<sub>p</sub> from 7.0 to 6.0. Counter intuitively, the DMSP threshold crossing actually migrates slightly more toward the equator. There is no change in the NH or OH model outputs because both they are capped at K<sub>p</sub> 6. The OP model, however, also follows the DMSP boundary, despite the fact that the decrease in K<sub>p</sub> statistically warrants

poleward migration. This serves as a testament to the benefit of a highly adaptable model like OP.

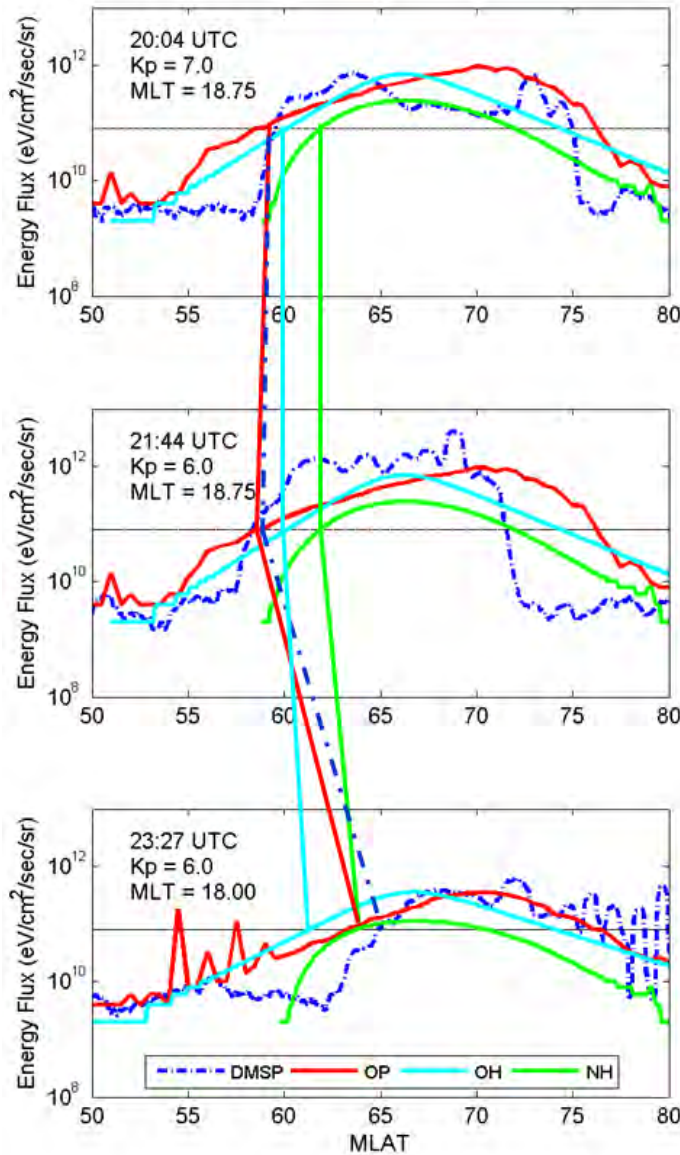


**Figure 39.** Three chronological plots of the energy flux profiles of the DMSP data and the NH, OH, and OP models. The vertical lines drawn between the panels show the migration of the threshold crossings.

In the third panel, again containing data obtained approximately 1 hour and 40 minutes later, the poleward migration of the threshold crossing coordinates of the NH and

OH models is solely due to the change in MLT sector. The Kp index remains the same because the data falls within the three hour window that was applicable to the previous satellite pass. However, it is clear that the auroral oval is relaxing back to a less stormy state. Again, if the noise is ignored in the region between 50 and 60° MLAT, the OP model successfully follows the DMSP data migration.

It is dangerous to make definitive conclusions based upon one example, but this does show the potential of using and developing a highly adaptable model construct that is not immune to small changes in the geomagnetic conditions that are occurring at a far faster rate than the Kp index is updated. Somewhat cautiously, therefore, it is possible to suppose that the future of auroral forecasting will continue to improve upon the same “nowcasting” capabilities already present, to some degree, in the OP model. That being said, the climatological utility of empirically derived models, like OH and NH, holds an important place in the assessment of space weather conditions.

## V. Conclusion

In this chapter, the development of the experiment and its results will be briefly summarized. Some additional comments will be made regarding avenues of future research.

### 5.1 Summary of Results

The ability to accurately model the auroral oval is important to national security objectives in the space domain. The auroral activity serves as a remarkable proxy for the space weather environment, and the precipitation patterns associated with it have a direct impact on space-based operations, especially including communication and navigation capabilities.

This study obtained data from more than 6,000 DMSP satellites passes between 2000-2008. This data was carefully quality checked and vetted against previous studies of a similar nature. It was determined that, despite a high degree of variance, the characteristics and location of the equatorward boundary could be effectively determined using the DMSP data.

The five models utilized in this study brought to bear several different approaches to modeling, and the characteristic behavior of each of the models under a variety of conditions was investigated in detail. This exposed the nature of the data loss problem that was encountered when the energy flux threshold was set too high. It also revealed a systematic noise issue with the low-latitude output of the OP model, and it underscored the limitations of models like SWMF and AMIE, whose resolutions were significantly coarser than the other models.

Each model's output was compared to DMSP data, and several basic statistics were obtained. Calculations of each model's mean deviations and the variance of these deviations led to the validation of the NH, OH, OP, and SWMF as viable models under certain conditions. Then, the prediction efficiency of each model was calculated using the 0.4 erg/cm<sup>2</sup>/s threshold dataset because it was determined to have the highest validity.

Calculating the prediction efficiency scores led to the conclusion that the OP model was the most accurate, but each model had comparative success when certain criteria were imposed. The OH model received high scores for data obtained between 10-15 MLT. The OP model's PE scores were high during low-K<sub>p</sub> conditions. The SWMF model was extremely effective during high-K<sub>p</sub> conditions, regardless of season or MLT sector. Here, it was also ascertained that the AMIE model underperformed in all categories.

The results found using a 0.4 erg/cm<sup>2</sup>/s threshold were corroborated using a dataset obtained with a 0.6 erg/cm<sup>2</sup>/s threshold. The PE scores at this threshold showed a substantial uptick in the performance of the OP model, which was ultimately attributed to a lack of adaptation of the NH and OH models to the new threshold. Of the 18 categories in which data was available, the same model had the highest PE score 8 times, and the OP model was responsible for 5 of those 8 occurrences. From these results, the OP model was determined to be the most uniformly accurate model.

Skill scores were also used to measure the performance of the NH and OP models using the OH model as the reference. At the low energy threshold, both models generally performed better than OH. Ultimately, the skill score analysis did not contribute much to the distinction between the model's performances.

Finally, a small-scale study was conducted utilizing 48 hand-selected examples of nightside aurora with well-defined equatorward boundaries. These cases were selected in order to study and categorize the models' performance during relatively static auroral precipitation conditions. The results of this micro study led to the conclusion that the OH model was the most accurate at modeling conditions with an unambiguous boundary, which is consistent with its statistically based development. However, it was also shown that the adaptable design of the OP model was a modeling capability that distinctly exceeded both of the highly discretized Hardy models.

Based upon these factors, the OVATION Prime model has manifested itself as the most suitable candidate for operational employment. Foremost, it exhibited the highest degree of accuracy when using a fixed energy flux threshold to depict the geographic extent of the auroral oval, and this accuracy was corroborated at multiple thresholds. Its equatorward bias detracts from its accuracy, but this behavior is operationally more conservative than is underestimating the oval's extent. The OP model also offers a highly adaptable approach to modeling, which presents an important capability, especially during high-K<sub>p</sub> conditions.

## 5.2 Future Research

The scope of this research was truly broad, and opportunities for future research exist along many different avenues. At the outset, it would certainly be warranted to recreate the statistics obtained in this study with a larger data set by utilizing more of the available DMSP data. There exists, however, an inherent challenge in utilizing DMSP data, and it is important some sort of quality standard is enforced. This is the most time

consuming element of a study of this sort, but an enhanced computer algorithm to streamline the process is within the realm of possibility.

An additional avenue of complementary research pertains to the criterion/criteria by which the equatorward boundary is defined. This study took a somewhat simplistic approach by looking at a fixed energy flux threshold. Exploring other means of identifying the boundary would certainly be a fair and useful way to corroborate the results found in this study.

Finally, the use of a different source of data rather than single pass particle counts from the DMSP satellites may yield fruitful results. There are a multitude of additional sources that can be used to directly measure or infer the equatorward boundary of the auroral oval. Synoptic measurements, such as those obtained with all-sky cameras or the Polar satellites UVI instrument, could prove to be excellent tools for capturing this highly dynamic phenomenon.

## Bibliography

- Akasofu, S-I. (1991). Auroral Phenomena. *Auroral physics*. Eds. Ching –I. Meng, Michael J. Rycroft, and Louis A. Frank. Cambridge: Cambridge University Press.
- Gussenhoven, M.S., et al. (1981). DMSP F2 electron observations of equatorward auroral boundaries and their relationship to magnetospheric electric fields. *Journal of geophysical research*, 86(A2), 768-778.
- Gussenhoven, M.S. & Hardy, D.A. (1983). Systematics of the Equatorward Diffuse Auroral Boundary. *Journal of geophysical research*, 88(A7), 5692-5708.
- Hardy, D.A., et al. (1985). A statistical model of auroral electron precipitation. *Journal of geophysical research*, 90(A5), 4229-4248.
- Hardy, D.A., et al. (2008). Probability distributions of electron precipitation at high magnetic latitudes. *Journal of geophysical research*, 110(A60305), 1-19.
- Hargreaves, J.K. (1995). *The solar-terrestrial environment*. Cambridge, England: Cambridge University Press.
- Menvielle, M. & Berthelier, A. “The K-Derived Planetary Indices: Description and Availability,” *Review of Geophysics*, 29, 3: 415-432 (August 1991).
- Newell, P.T., et al. (1996). Morphology of nightside precipitation. *Journal of geophysical research*, 101(A5). 10737-10748.
- Newell, P.T., et al. (2002). OVATION: Oval variation, assessment, tracking, intensity, and online nowcasting. *Annales Geophysicae*, 20, 1039-1047.
- Newell, P.T., et al. (2009). Diffuse, monoenergetic, and broadband aurora: The global precipitation budget. *Journal of geophysical research*, 114(A09207). 1-20.
- Newell, P.T., et al. (2010a). Predictive ability of four auroral precipitation models as evaluated using Polar UVI global images. *Space Weather*, 8, 1-9.
- Newell, P.T., et al. (2010b). Seasonal variations in diffuse, monoenergetic, and broadband aurora. *Journal of geophysical research*, 115(A03216). 1-19.
- Ohtani, S., et al. (2004). Temporal structure of the fast convective flow in the plasma sheet: Comparison between observations and two-fluid simulations. *Journal of geophysical research*, 109(A03210). 1-16.
- Paschmann, G., Haaland, S., & Treumann, R. (Eds.). (2003). *Auroral plasma physics*. Norwell, MA: Kluwer Academic.

- Prölss, G.W. (2004). *Physics of the earth's space environment*. Bonn, Germany: Springer.
- Redmon, R.J., et al. (2010). Vertical thermal O<sup>+</sup> flows at 850 km in dynamic auroral boundary coordinates. *Journal of geophysical research*, 115(A00J08). 1-10.
- Richmond, A.D., et al. (1998). The AMIE procedure: Prospects for space weather specification and prediction. *Advanced Space Research*, 22, 103-112.
- Schunk, R. & Nagy, A. (2009). *Ionospheres: physics, plasma physics, and chemistry*. New York, NY: Cambridge University Press.
- Siscoe, G. (1991). What determines the size of the auroral oval? *Auroral physics*. Eds. Ching –I. Meng, Michael J. Rycroft, and Louis A. Frank. Cambridge: Cambridge University Press.
- Sotirelis, T. & Newell, P.T. (2000). Boundary-oriented electron precipitation model. *Journal of geophysical research*, 105(A8). 18655-18637.
- Tascione, T. F. (1988). *Introduction to the space environment*. Malabar, FL: Orbit Book Co.
- Tóth, G., et al. (2005). Space Weather Modeling Framework: A new tool for the space science community. *Journal of geophysical research*, 110(A12226). 1-21.
- Whalen, J.A. (2001). The aurora. *Handbook of geophysics and space environment*. Hanscomb AFB, MA: Air Force Geophysics Laboratory.
- Wing, S., et al. (2005). Kp forecast models. *Journal of geophysical research*, 110(A04203). 1-14.
- Zheng, Yihua. NASA-Goddard Space Flight Center. Personal communication. (November, 2011).

| REPORT DOCUMENTATION PAGE  |                                   |   |   | Form Approved<br>OMB No. 074-0188  |
|--|-----------------------------------|---|---|--|
| <p>The public reporting burden for this collection of information is estimated to average 1 hour per response, including the time for reviewing instructions, searching existing data sources, gathering and maintaining the data needed, and completing and reviewing the collection of information. Send comments regarding this burden estimate or any other aspect of the collection of information, including suggestions for reducing this burden to Department of Defense, Washington Headquarters Services, Directorate for Information Operations and Reports (0704-0188), 1215 Jefferson Davis Highway, Suite 1204, Arlington, VA 22202-4302. Respondents should be aware that notwithstanding any other provision of law, no person shall be subject to an penalty for failing to comply with a collection of information if it does not display a currently valid OMB control number.</p> <p><b>PLEASE DO NOT RETURN YOUR FORM TO THE ABOVE ADDRESS.</b></p>   |                                   |   |   |  |
| 1. REPORT DATE (DD-MM-YYYY)<br>22-03-2011  | 2. REPORT TYPE<br>Master's Thesis | 3. DATES COVERED (From – To)<br>Sep 2009 – Mar 2011                           |   |  |
| 4. TITLE AND SUBTITLE<br><br>Comparative Statistical Analysis of Auroral Models  |                                   | 5a. CONTRACT NUMBER<br><br>5b. GRANT NUMBER<br><br>5c. PROGRAM ELEMENT NUMBER |   |  |
| 6. AUTHOR(S)<br><br>Lane, Cory T., Major, USAF   |                                   | 5d. PROJECT NUMBER<br><br>5e. TASK NUMBER<br><br>5f. WORK UNIT NUMBER         |   |  |
| 7. PERFORMING ORGANIZATION NAMES(S) AND ADDRESS(S)<br><br>Air Force Institute of Technology<br>Graduate School of Engineering and Management (AFIT/EN)<br>2950 Hobson Way<br>WPAFB OH 45433-7765   |                                   |   | 8. PERFORMING ORGANIZATION REPORT NUMBER<br><br>AFIT/APPLPHY/ENP/12-M07 |  |
| 9. SPONSORING/MONITORING AGENCY NAME(S) AND ADDRESS(ES)<br><br>Dr. Yihua Zheng (yihua.zheng@nasa.gov)<br>NASA Goddard Space Flight Center Space Weather Laboratory<br>8800 Greenbelt Rd.<br>Greenbelt, MD 20771  |                                   |   | 10. SPONSOR/MONITOR'S ACRONYM(S)<br>NASA-CCMC                           |  |
|  |                                   |   | 11. SPONSOR/MONITOR'S REPORT NUMBER(S)                                  |  |
| 12. DISTRIBUTION/AVAILABILITY STATEMENT<br><br>APPROVED FOR PUBLIC RELEASE; DISTRIBUTION UNLIMITED   |                                   |   |   |  |
| 13. SUPPLEMENTARY NOTES  |                                   |   |   |  |
| <b>14. ABSTRACT</b><br><p>The location of the equatorward boundary of the auroral oval provides an appropriate means to measure the accuracy of auroral models. In this study, the equatorward boundary is represented by the location at which the energy flux data measured by DMSP satellites exceeds 0.4 erg/cm<sup>2</sup>/s. The MLAT coordinates obtained from more than 4,000 orbits through the polar region of the Northern Hemisphere comprise the data set used to compare to the outputs of five auroral models. These models are: the original Hardy auroral model of 1985 (OH), the OVATION Prime model (OP), the 2008 adaptation to the Hardy model (NH), the Space Weather Modeling Framework Ring-Current model (SWMF), and the Assimilated Mapping of Ionospheric Electrodynamics model (AMIE).</p> <p>In each of the 19 individual Kp-MLT-season categories considered in this study, the model with the highest PE score was determined. The SWMF model received the highest PE score in 4 categories, the NH model in 4 categories, the OH model in 5 categories, and the OP model in 6 categories. The results also showed the SWMF model clearly outperforms the other models during events where the Kp index was greater than 6, but there were no other unequivocal occurrences of a model's specific success in a particular subcategory.</p> <p>The model that has the highest prediction efficiency score without subdividing the data into categories is the OP model (0.55). The OH model (0.51) has the second best score, and it is followed by the NH model (0.45). These results were corroborated using an energy flux threshold of 0.6 erg/cm<sup>2</sup>/s. Based upon the specific criteria of this study, the OP model has been determined to most accurately represent the equatorward boundary of the auroral oval.</p> |                                   |   |   |  |
| 15. SUBJECT TERMS  |                                   |   |   |  |
| 16. SECURITY CLASSIFICATION OF:  |                                   | 17. LIMITATION OF ABSTRACT  | 18. NUMBER OF PAGES   | 19a. NAME OF RESPONSIBLE PERSON<br>Lt Col Ariel O. Acebal (AFIT/ENP)                     |
| a. REPORT<br>U   | b. ABSTRACT<br>U                  | c. THIS PAGE<br>U   | UU<br>119   | 19b. TELEPHONE NUMBER (Include area code)<br>937-255-3636 x4518<br>ariel.acebal@afit.edu |